

Beam Energy and Collision System Dependence of Anisotropic Flow and Its Fluctuations

A Dissertation presented

by

Niseem Magdy Abdelwahab Abdelrahman

to

The Graduate School

in Partial Fulfillment of the

Requirements

for the Degree of

Doctor of Philosophy

in

Chemistry

(Concentration - optional)

Stony Brook University

December 2018

Stony Brook University

The Graduate School

Niseem Magdy Abdelwahab Abdelrahman

We, the dissertation committee for the above candidate for the

Doctor of Philosophy degree, hereby recommend

acceptance of this dissertation

Roy A. Lacey
Professor, Department of Chemistry

Peter Khalifah
Professor, Department of Chemistry

Jiangyong Jia
Professor, Department of Chemistry

Zhangbu Xu
BNL STAR Group Leader, Brookhaven National Laboratory

This dissertation is accepted by the Graduate School

Dean of the Graduate School

Abstract of the Dissertation

Beam Energy and Collision System Dependence of Anisotropic Flow and Its Fluctuations

by

Niseem Magdy Abdelwahab Abdelrahman

Doctor of Philosophy

in

Chemistry

(Concentration - optional)

Stony Brook University

2017

New measurements of the flow harmonics ($v_{n \leq 5}$) and the elliptic flow fluctuations are presented as a function of harmonic number (n), transverse momentum (p_T), pseudorapidity (η) and collision centrality, for Au+Au collisions spanning a broad range of beam energies ($\sqrt{s_{NN}} = 7.7 - 200$ GeV), as well as for U+U ($\sqrt{s_{NN}} = 193$ GeV) and Cu+Au, Cu+Cu and d+Au collisions at $\sqrt{s_{NN}} = 200$ GeV. The measurements, performed with the STAR detector at the Relativistic Heavy Ion Collider (RHIC), show characteristic dependencies on centrality, $\sqrt{s_{NN}}$, η , p_T and collision system, consistent with the development of hydrodynamic-like flow in Quark-Gluon Plasma (QGP) created in these collisions. The rapidity-even dipolar flow (v_1^{even}) measurements underscore the importance of momentum conservation and the role of geometric fluctuations generated in the initial stages of the collisions. The $v_{n=2-5}$ measurements accentuate the influence of the specific shear viscosity ($\frac{\eta}{s}$), initial-state eccentricity (ϵ_n) and dimensionless size (RT), on the magnitude of v_n and its viscous attenuation in the QGP. The measurements for elliptic flow fluctuations in Au+Au collisions for $\sqrt{s_{NN}} = 7.7 - 200$ GeV (Beam Energy Scan (BES) energies), as well as for different collision systems

at $\sqrt{s_{\text{NN}}} \sim 200$ GeV, give new insight into the origin of flow fluctuations as well as their influence on the magnitude of v_n . They indicate sizeable fluctuations in central collisions, a modest dependence on event-shape and system size, and a rather weak dependence on p_T , beam energy and particle species. The detailed $v_{n \leq 5}$ and fluctuations measurements presented, give new insight into the patterns of viscous attenuation and $\frac{\eta}{s}$ for the matter created in the systems studied. The unique set of measurements spanning the BES energies are essential to ongoing theoretical efforts to extract both the μ_B and T dependence of the specific shear viscosity $\frac{\eta}{s}$, of the quark-gluon plasma.

Contents

1	Introduction	1
1.1	The Quantum Chromodynamics	1
1.1.1	The QCD Phase Diagram	2
1.2	The Quark Gluon Plasma	4
1.2.1	Space-time evolution of heavy ion collisions	5
1.2.2	Heavy-Ion collision experiments	5
1.2.3	The RHIC Beam Energy Scan Program	6
1.2.4	Essential concepts and definitions for heavy ion collisions	7
1.3	Anisotropic Flow	10
1.4	Scope and Organization of this thesis	11
2	Experimental Setups and Data Sets	13
2.1	Relativistic Heavy Ion Collider	13
2.2	STAR Detector	16
2.2.1	Time Projection Chamber (TPC)	17
2.2.2	Time Of Flight (TOF)	19
2.3	Centrality Definition in Heavy-Ion Collisions	20
2.4	Data Sets	22
3	Flow Analysis Methodology	24
3.1	Anisotropic Flow	24
3.2	Two-Particle Azimuthal Correlations (Event-Mixing Technique)	28
3.2.1	Suppression of short range non-flow effects	29
3.2.2	Suppression of long-range non-flow (Global Momentum Conservation)	33
3.3	Multi-Particle Correlation Technique	37
3.3.1	Correcting for detector acceptance	37

3.3.2	Standard cumulant method	38
3.3.3	The two-subevents cumulant method	42
3.3.4	The three sub-events cumulant method	44
3.3.5	Flow fluctuations effects	46
4	Beam Energy and Collision System Dependence of Flow Harmonics	48
4.1	Beam Energy Dependence of v_n	48
4.1.1	Flow harmonics measurements for $v_{n>1}$	49
4.1.2	The rapidity-even dipolar flow v_1^{even}	54
4.2	Collision System Dependence of v_n	61
4.2.1	An acoustic model for the viscous attenuation of flow .	67
4.2.2	The odd flow harmonics v_1^{even} and v_3	68
4.2.3	The even flow harmonic v_2	72
4.2.4	Data scaling features	73
5	Beam Energy and Collision System Dependence of Flow Fluctuations	77
5.1	Beam Energy Dependence of Flow Fluctuations	79
5.2	Collision System Dependence of Flow Fluctuations	86
6	Conclusion	92

List of Figures

Fig. 1.1:	Conjectured phase diagram for QCD matter in the μ_B and T plain.	3
Fig. 1.2:	The time evolution of heavy ion collision.	4
Fig. 1.3:	Schematic illustration of the phase diagram of QCD matter with conjectured trajectories for several collision energies at RHIC. The yellow lines indicate the conjectured trajectories for Au+Au collisions for the beam energies indicated.	7
Fig. 1.4:	Schematic illustration of a heavy ion collision seen from the CM frame. Panel (a) illustrates the definition of the impact parameter and pannel (b) shows the participant and spectators (see text).	8
Fig. 1.5:	Example of a standard non-central heavy-ion collision in which the eccentric shape of initial collision geometry is transposed into the elliptic flow anisotropy in the final state momentum space.	11
Fig. 2.1:	The RHIC accelerator complex at Brookhaven National Laboratory.	14
Fig. 2.2:	A perspective view of the STAR detector system with a cutaway for viewing the inner sub-systems.	16
Fig. 2.3:	The diagram of STAR Time Projection Chamber at RHIC.	17
Fig. 2.4:	The energy loss distribution for primary and secondary particles in the STAR TPC.	18
Fig. 2.5:	m^2 computed using the time of flight measurements from the TOF detector.	20
Fig. 2.6:	Illustration of the use of charged track multiplicity selections for centrality definition	21

Fig. 3.1:	A representation of the formation of almond-shaped interaction volume created in mid-central collision of two nuclei. The spatial anisotropy of the interaction volume with respect to reaction-plane (x-z plane), leads to a momentum anisotropy of the produced particles.	26
Fig. 3.2:	Like-sign two-particle correlation function for 0 – 5%, 40 – 50% and 70 – 80% central Au+Au collisions at $\sqrt{s_{NN}} = 200$ GeV for different $\Delta\eta$ cuts.	30
Fig. 3.3:	Unlike-sign two-particle correlation functions for 0 – 5%, 40 – 50% and 70 – 80% central Au+Au collisions at $\sqrt{s_{NN}} = 200$ GeV, for different $ \Delta\eta $ cuts.	31
Fig. 3.4:	Comparison of LS- and US- v_2 values for Au+Au collisions at $\sqrt{s_{NN}} = 200$ GeV. Results are shown for $ \Delta\eta > 0.3, 0.7$ and 0.9 respectively.	32
Fig. 3.5:	Comparison of LS- and US- v_3 for Au+Au collisions at $\sqrt{s_{NN}} = 200$ GeV for $ \Delta\eta > 0.3, 0.7$ and 0.9 respectively.	33
Fig. 3.6:	Comparison of LS- and US- v_4 for Au+Au collisions at $\sqrt{s_{NN}} = 200$ GeV and $ \Delta\eta > 0.3, 0.7$ and 0.9 respectively.	34
Fig. 3.7:	v_{11} vs. p_T^b for several selections of p_T^a for 0-5% central Au+Au collisions at $\sqrt{s_{NN}} = 200$ GeV. The curve shows the result of the simultaneous fit with Eq. (3.24). The fit resulted in the value $\chi^2 = 1.1$ per degree of freedom.	35
Fig. 3.8:	The extracted values of v_1^{even} vs. p_T for Au+Au collisions at $\sqrt{s_{NN}} = 200$ GeV. (b) A representative set of the associated values of K vs. $\langle Mult \rangle^{-1}$ from the same fits. The lines in panel (a) represent the result from a hydrodynamic calculations. In panel (b) the associated momentum conservation coefficient, K vs. $\langle N_{ch} \rangle^{-1}$ is presented	36
Fig. 3.9:	The ϕ - η map for Au+Au $\sqrt{s_{NN}} = 200$ GeV before weighting for low (a) and high (b) p_T .	37
Fig. 3.10:	The ϕ distribution for different collision systems before and after the acceptance correction.	38

Fig. 4.1:	The left panel shows the p_T integrated v_2 and v_3 coefficients vs. $\sqrt{s_{NN}}$. The lines represent the results obtained using $\sqrt{s_{NN}}$ dependent η/s . The right panel shows the effective values of η/s used to describe the experimental data at different collision energies. The green-band represents the estimated uncertainty.	49
Fig. 4.2:	The $v_{n \geq 2}$ as a function of $ \eta $ for charged particles with $0.2 < p_T < 4$ GeV/c in 0-40% central Au+Au collisions at $\sqrt{s_{NN}} = 7.7-200$ GeV. The shaded bands represent the systematic uncertainty.	50
Fig. 4.3:	The $v_{n \geq 2}$ as a function of p_T for charged particles in 0-40% central Au+Au collisions at $\sqrt{s_{NN}} = 7.7-200$ GeV. The shaded bands represent the systematic uncertainty.	51
Fig. 4.4:	The integrated $v_n(\text{Centrality}\%)$ as a function of Au+Au collision centrality for charged particles with $0.2 < p_T < 4$ GeV/c. The shaded bands represent the systematic uncertainty.	52
Fig. 4.5:	The integrated $v_n(\sqrt{s_{NN}})$ for charged particles with $0.2 < p_T < 4$ GeV/c for 0-40% central Au+Au collisions. The shaded bands represent the systematic uncertainty.	53
Fig. 4.6:	(a) The extracted values of v_1^{even} vs. p_T for Au+Au collisions at $\sqrt{s_{NN}} = 200$ GeV. (b) A representative set of the associated values of K vs. $\langle N_{ch} \rangle^{-1}$ from the same fits. The shaded bands represent the systematic uncertainty.	54
Fig. 4.7:	Extracted values of v_1^{even} vs. p_T for 0-10% central Au+Au collisions for several values of $\sqrt{s_{NN}}$ as indicated.	56
Fig. 4.8:	Extracted values of $\langle p_T v_1^{even}(p_T) \rangle$ vs. $\sqrt{s_{NN}}$ for 0-10% central Au+Au collisions.	57
Fig. 4.9:	Centrality dependence of v_1^{even} for $0.4 < p_T < 0.7$ GeV/c for Au+Au collisions at $\sqrt{s_{NN}} = 200, 39,$ and 19.6 GeV. The shaded bands represent the systematic uncertainties.	58

Fig. 4.10:	The extracted K vs. $\langle N_{\text{ch}} \rangle^{-1}$ for the v_1^{even} values shown in Fig. 4.9. The indicated lines show linear fits to the data; the shaded bands represent the systematic uncertainties.	59
Fig. 4.11:	Comparison of the $\sqrt{s_{\text{NN}}}$ dependence of v_1^{even} and v_3 for $0.4 < p_T < 0.7$ GeV/c in 0-10% central Au+Au collisions. The v_1^{even} results are reflected about zero (and shifted horizontally) to facilitate a comparison of the magnitudes. The shaded bands indicate the systematic uncertainties.	60
Fig. 4.12:	Two-particle correlation functions for p_T -integrated track pairs with $0.7 < \Delta\eta < 2.0$. Results are shown for U+U (a) collisions ($\sqrt{s_{\text{NN}}} = 193$ GeV) and Au+Au (b), Cu+Au (c), and Cu+Cu (d) collisions ($\sqrt{s_{\text{NN}}} = 200$ GeV) for $\langle N_{\text{ch}} \rangle = 140$. The solid curves, show the result of a Fourier fit to the data.	63
Fig. 4.13:	Two-particle correlation functions for p_T -integrated track pairs with $0.7 < \Delta\eta < 2.0$. Results are shown for U+U (a) collisions ($\sqrt{s_{\text{NN}}} = 193$ GeV) and Au+Au (b), Cu+Au (c), and Cu+Cu (d) collisions ($\sqrt{s_{\text{NN}}} = 200$ GeV) for $\langle N_{\text{ch}} \rangle = 70$. The solid curves, show the result of a Fourier fit to the data.	64
Fig. 4.14:	Two-particle correlation functions for p_T -integrated track pairs with $0.7 < \Delta\eta < 2.0$. Results are shown for U+U (a) collisions ($\sqrt{s_{\text{NN}}} = 193$ GeV) and Au+Au (b), Cu+Au (c), Cu+Cu (d), and d+Au (e) collisions ($\sqrt{s_{\text{NN}}} = 200$ GeV) for $\langle N_{\text{ch}} \rangle = 21 \pm 3$. The solid curves, show the result of a Fourier fit to the data.	65
Fig. 4.15:	The second-order four-particle for p_T -integrated cumulants, $c_2\{4\}$, vs. $\langle N_{\text{ch}} \rangle$, obtained for U+U (a) collisions ($\sqrt{s_{\text{NN}}} = 193$ GeV) and Au+Au (b), Cu+Au (c), Cu+Cu (d), and d+Au (e) collisions at $\sqrt{s_{\text{NN}}} = 200$ GeV.	66
Fig. 4.16:	The extracted v_1^{even} vs. p_T for several $\langle N_{\text{ch}} \rangle$ selections. Results are compared for U+U, Au+Au, Cu+Au and Cu+Cu for $\langle N_{\text{ch}} \rangle = 140$, and $\langle N_{\text{ch}} \rangle = 70$ and for U+U, Au+Au, Cu+Au, Cu+Cu and d+Au for $\langle N_{\text{ch}} \rangle = 21 \pm 3$	69

Fig. 4.17:	The extracted v_3 vs. p_T for several $\langle N_{ch} \rangle$ selections. Results are compared for U+U, Au+Au, Cu+Au and Cu+Cu for $\langle N_{ch} \rangle = 140$, and $\langle N_{ch} \rangle = 70$ and for U+U, Au+Au, Cu+Au, Cu+Cu and d+Au for $\langle N_{ch} \rangle = 21 \pm 3$	70
Fig. 4.18:	Comparison of the $\langle N_{ch} \rangle$ dependence of v_1^{even} for all collision systems for the p_T selections $0.2 < p_T(\text{GeV}/c) < 4$. The $\langle N_{ch} \rangle$ values for d+Au correspond to $\sim 0\text{-}20\%$ central collisions.	70
Fig. 4.19:	Comparison of the $\langle N_{ch} \rangle^{-1}$ dependence of the extracted values of K for all collision systems. The dashed line represent the straight line fit.	71
Fig. 4.20:	Comparison of the $\langle N_{ch} \rangle$ dependence of v_3 for all collision systems for the p_T selections $0.2 < p_T(\text{GeV}/c) < 4$. The $\langle N_{ch} \rangle$ values for d+Au correspond to $\sim 0\text{-}20\%$ central collisions.	71
Fig. 4.21:	The extracted v_2 vs. p_T for several $\langle N_{ch} \rangle$ selections. Results are compared for U+U, Au+Au, Cu+Au and Cu+Cu for $\langle N_{ch} \rangle = 140$, and $\langle N_{ch} \rangle = 70$ and for U+U, Au+Au, Cu+Au, Cu+Cu and d+Au for $\langle N_{ch} \rangle = 21 \pm 3$	72
Fig. 4.22:	Comparison of the $\langle N_{ch} \rangle$ dependence of v_2 for all collision systems for the p_T selections $0.2 < p_T(\text{GeV}/c) < 4$. The $\langle N_{ch} \rangle$ values for d+Au correspond to $\sim 0\text{-}20\%$ central collisions.	73
Fig. 4.23:	The scaled v_2/ϵ_2 vs. p_T for several $\langle N_{ch} \rangle$ selections. Results are compared for U+U, Au+Au, Cu+Au and Cu+Cu for $\langle N_{ch} \rangle = 140$, and $\langle N_{ch} \rangle = 70$ and for U+U, Au+Au, Cu+Au, Cu+Cu and d+Au for $\langle N_{ch} \rangle = 21 \pm 3$	74
Fig. 4.24:	The scaled v_2/ϵ_2 vs. $\langle N_{ch} \rangle^{-1/3}$ for all collision systems for the p_T selections $0.2 < p_T(\text{GeV}/c) < 4$. The dashed lines represent exponential fits to the data.	75
Fig. 4.25:	The scaled v_2/ϵ_2 vs. $\langle N_{ch} \rangle^{-1/3}$ for all collision systems for the p_T selections $0.2 < p_T(\text{GeV}/c) < 4$. The dashed line represents an exponential fit to the data.	76

Fig. 5.1:	The integrated Two-, four- and six-particle elliptic flow, $v_2\{k\}$, $k = 2, 4$ and 6 (panel a) and their ratios (panels b and c) vs. centrality, for Au+Au collisions at $\sqrt{s_{NN}} = 200$ GeV.	78
Fig. 5.2:	The integrated Two-, four- and six-particle elliptic flow $v_2\{k\}$, $k = 2, 4$ and 6 (panels (a) and (b)), and their ratios (panel (c)) as a function of centrality for Au+Au collisions at $\sqrt{s_{NN}} = 7.7 - 200$ GeV.	80
Fig. 5.3:	(a) The q_2 distribution for 40 – 50% Au+Au collisions at $\sqrt{s_{NN}} = 200$ GeV, for the sub-event sample with $ \eta < 0.35$. The indicated bands represent different $q_2\%$ selections; (b) illustrative plot of $v_2\{2\}$ as a function of q_2 for the $q_2\%$ selections in (a).	81
Fig. 5.4:	Comparison of (a) $v_2\{2\}$, (b) $v_2\{4\}$ and (c) $v_2\{4\}/v_2\{2\}$ as a function of centrality for several q_2 selections for Au+Au collisions at $\sqrt{s_{NN}} = 200$ GeV.	81
Fig. 5.5:	Comparison of (a) $v_2\{2\}$, (b) $v_2\{4\}$ and (c) $v_2\{4\}/v_2\{2\}$ as a function of centrality for several q_2 selections for Au+Au collisions at $\sqrt{s_{NN}} = 54$ GeV.	82
Fig. 5.6:	Comparison of (a) $v_2\{2\}$, (b) $v_2\{4\}$ and (c) $v_2\{4\}/v_2\{2\}$ as a function of centrality for several q_2 selections for Au+Au collisions at $\sqrt{s_{NN}} = 39$ GeV.	82
Fig. 5.7:	The integrated $v_2\{2\}$, $v_2\{4\}$, and $v_2\{4\}/v_2\{2\}$ of identified hadrons as a function of centrality for Au+Au collisions at $\sqrt{s_{NN}} = 200$ GeV; are shown.	83
Fig. 5.8:	The integrated $v_2\{2\}$, $v_2\{4\}$, and $v_2\{4\}/v_2\{2\}$ of identified hadrons as a function of centrality for Au+Au collisions at $\sqrt{s_{NN}} = 54$ GeV; are shown.	84
Fig. 5.9:	The integrated $v_2\{2\}$, $v_2\{4\}$, and $v_2\{4\}/v_2\{2\}$ of identified hadrons as a function of centrality for Au+Au collisions at $\sqrt{s_{NN}} = 39$ GeV; are shown.	85
Fig. 5.10:	The p_T differential $v_2\{2\}$, $v_2\{4\}$, and $v_2\{4\}/v_2\{2\}$ for Au+Au collisions at different beam energies are shown.	85
Fig. 5.11:	The integrated $v_2\{2\}$, $v_2\{4\}$, $v_2\{6\}$ and their ratios as a function of centrality for U+U collisions at $\sqrt{s_{NN}} = 193$ GeV, Au+Au, Cu+Au, and Cu+Cu collisions at $\sqrt{s_{NN}} = 200$ GeV; are shown.	86

Fig. 5.12:	The integrated $v_2\{2\}$, $v_2\{4\}$, and $v_2\{4\}/v_2\{4\}$ as a function of centrality for several q_2 selections for U+U collisions at $\sqrt{s_{NN}} = 193$ GeV, Au+Au and Cu+Au collisions at $\sqrt{s_{NN}} = 200$ GeV; are shown.	87
Fig. 5.13:	The integrated identified hadrons $v_2\{2\}$, $v_2\{4\}$, and $v_2\{4\}/v_2\{4\}$ as a function of centrality for U+U collisions at $\sqrt{s_{NN}} = 193$ GeV; are shown.	88
Fig. 5.14:	The integrated identified hadrons $v_2\{2\}$, $v_2\{4\}$, and $v_2\{4\}/v_2\{4\}$ as a function of centrality for Cu+Au collisions at $\sqrt{s_{NN}} = 200$ GeV; are shown.	89
Fig. 5.15:	The p_T differential $v_2\{2\}$, $v_2\{4\}$, and $v_2\{4\}/v_2\{4\}$ for different collision systems at $\sqrt{s_{NN}} \sim 200$ GeV are shown.	90

List of Tables

Tab. 1.1:	Mass, length and time in Natural units.	10
Tab. 2.1:	The run year and the vertex cut used for the different collision systems and energies studied in this thesis. . .	22
Tab. 2.2:	Track-cuts used in subsequent analyses'.	23

List of Abbreviations

In this dissertation different abbreviations are used which I list them here:

- QCD: Quantum Chromodynamics
- QED: Quantum Electrodynamics
- QGP: Quark Gluon Plasma
- RHIC: Relativistic Heavy Ion Collider
- STAR: Solenoidal Tracker at RHIC
- LHC: Large Hadron Collider
- CEP: Critical End Point
- BES: Beam Energy Scan
- μ_B : Baryon chemical potential
- T_c : Critical temperature
- $\sqrt{s_{NN}}$: Center-of-mass energy per nucleon-nucleon collision

Acknowledgements

First and foremost, I would like to dedicate my dissertation to my mother, Nawal Khattab, my father, Magdy El-Azaz, my brother, Mohamed El-Azaz, my sister Mai El-Azaz and my best friend Emily Racow, for their constant support and love. I would like to extend very special thanks to my advisor Dr. Roy Lacey for giving me the opportunity to work on this interesting topic for my Ph.D thesis, and for all the advice, guidance, and support he has given me. I would like to express my very special thanks to Dr. Paul Sorensen, Dr. Hoda Abou-Shady and Dr. Alaa-El-Din Bahgat for all the advice, and support they have given me. I am grateful to the members of the Stony Brook Heavyion group with whom I worked over the years, especially, Dr. Jiangyong Jia, Mr. Benjamin Schweid, Mr. Arabinda Behera, and Mr. Mingliang Zhou, for their help and friendship. My warm and sincere thanks to all the STAR conveners of STAR physics working group (PWG) and members of STAR collaboration for giving me valuable comments and suggestions on my work. Finally, I would like to express my sincere thanks to the RHIC Operations Group and RACF at BNL, the NERSC Center at LBNL and Grid Computing Facilities at VECC and NISER for providing resources and support.

(Niseem Abdelrahman)

Vita, Publications and/or Fields of Study

List of publications and papers accomplished:

- STAR Collaboration Papers (As a Primary Authors):
 - (a) Beam Energy Dependence of the Third Harmonic of Azimuthal Correlations in Au+Au Collisions at RHIC, Phys.Rev.Lett. 116 (2016) no.11, 112302
 - (b) Beam energy dependence of rapidity-even dipolar flow in Au+Au collisions, Phys.Lett.B 784 2632 (2018)
- Conference Proceedings (for the STAR Collaboration)
 - (a) Viscous Damping of Anisotropic Flow in 7.7-200 GeV Au+Au Collisions, J.Phys.Conf.Ser. 779 (2017) no.1, 012060
 - (b) Beam energy and system dependence of rapidity-even dipolar flow, EPJ Web Conf. 171 (2018) 16002
 - (c) Beam energy dependence of the anisotropic flow coefficients v_n , PoS CPOD2017 (2018) 005
 - (d) Collision system and beam energy dependence of anisotropic flow fluctuations, arXiv:1807.07638
- Paper Under Review in STAR Collaboration (As a Primary Authors):
 - (a) Charge separation measurements in p(d)+Au and Au+Au collisions; implications for the chiral magnetic effect.
 - (b) Collective anisotropic flow in small and large systems.
 - (c) Beam Energy and Collision System Dependence of Anisotropic Flow Fluctuations.
- Other Papers
 - (a) Influence of finite volume and magnetic field effects on the QCD phase diagram, J.Phys. G 44 (2017) no.2, 025101
 - (b) A New Correlator to Detect and Characterize the Chiral Magnetic Effect, Phys.Rev. C 97 (2018) no.6, 061901
 - (c) Can we detect a Chiral-Magnetically-driven charge separation difference in collisions of the $Ru + Ru$ and $Zr + Zr$ isobars at RHIC?, arXiv:1803.02416

Chapter 1

Introduction

1.1 The Quantum Chromodynamics

Studies of the strong nuclear force constitute a central theme in nuclear science research. The strong force is one of the four fundamental forces in nature. It binds quarks and gluons to form composite particles such as the neutrons and protons which comprise the nucleus of atoms. Here, gluons are the force carriers which mediate the interaction between quarks as stipulated by Quantum Chromodynamics (QCD) – the theory of the strong interaction.

One description of QCD is akin to the theory of Quantum Electrodynamics (QED) which describes the electromagnetic force mediated by photons. However, QCD has a larger number of degrees of freedom which complicates the theory. In QED, there is only one kind of charge (electric charge). By contrast, QCD has three charges (color-charges), commonly identified as red, blue and green, and their corresponding anti-colors. Unlike the photons, QED's electrically neutral mediator, the gluons carry color charge and hence, couple to each other to generatee important nonlinearities in the theory.

QCD theory incorporates six quark flavors, up(u), down(d), strange(s), charm(c), bottom(b) and top(t), with the up quark being the lightest and the top quark being the heaviest. The heavier quarks are unstable and readily decay into lighter quarks. Thus, the two light quarks, u and d, play an important role in QCD-matter formation. In addition to electric charge (e), quarks of any type can carry any of the three colors; the quarks also have fractional electric charges (u, c and t carry $+2/3e$, and d, s, and b carry $-1/3e$).

Composite particles derived from quarks are colorless and are called hadrons. Hadrons comprised of two and three quarks (respectively) are called mesons and baryons; mesons contain quark-anti-quark pairs. Quark confinement, which is essential to QCD, dictates that single quarks are not detectable.

Conceptually QCD is a simple theory [1]. However, it is notoriously difficult to solve [1]. Currently, there are several procedures employed to utilize QCD. One approach is a lattice gauge theory formulated on a grid or lattice of points in space and time (LQCD) . This numerical approach has made it possible to obtain several key predictions for the nature of QCD matter from first principles calculations [2]. Another approach is the common practice of incorporating the essential ideas of the QCD Lagrangian into Monte Carlo models such as PYTHIA[3] and HIJING[4]. The results from these approaches often provide an important basis for model comparisons to experimental measurements. Thus, the interplay between model calculations and experimental measurements play a vital role in ongoing efforts to study and develop a full understanding of QCD.

1.1.1 The QCD Phase Diagram

When subjected to the extremes of temperature (T) and pressure, QCD matter can undergo phase transitions to produce new states of matter. Such states of matter are schematically illustrated in Fig. 1.1 as a function T and baryon chemical potential (μ_B). Each point in the $T - \mu_B$ plane corresponds to a thermodynamic state. The diagram conveys many of the rudiments presented in one of the early phase diagram suggested by N.Cabibbo and G.Parisi in 1975 [5]. It also reflects crucial ideas from Hagedorn who inferred a critical temperature T_c , beyond which hadronic matter would not exist, due to an exponential increase in the mass spectra for hadronic states [6]. The solid line in Fig. 1.1 represents a first order transition line which separate the hadronic and quark-gluon plasma phases. The end point of this line is the Critical End Point (CEP). The dashed line at small μ_B indicates a cross-over transition between the quark-gluon plasma and the hadronic phases. At low temperatures and very high baryon density other exotic flavor-locked phases of QCD matter have been conjectured to exist as well.

In general, the indicated phase transitions, as well as those for other substances, are identified via derivatives of the thermodynamic potential with respect to T and μ . The transition between two different phases is usually

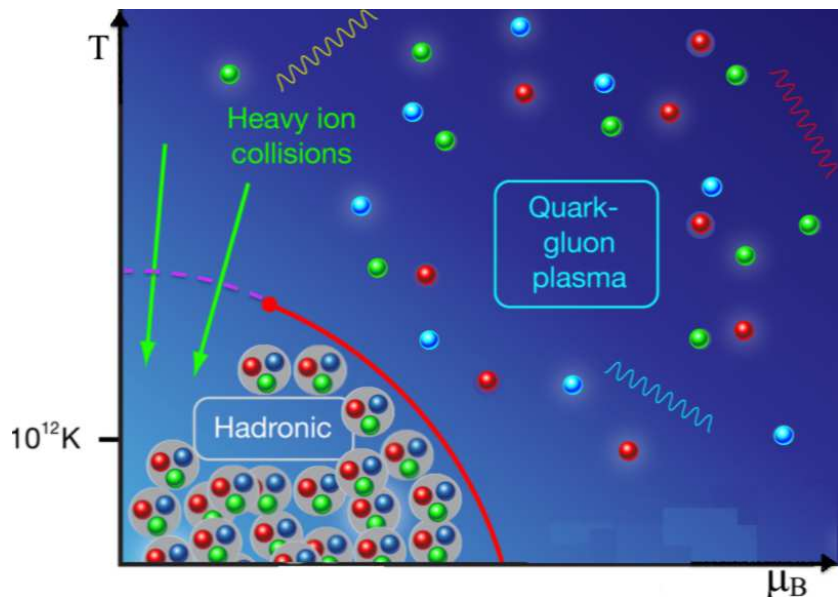


Fig. 1.1: Schematic diagram for of a conjectured phase diagram for QCD matter in the μ_B and T plain. A possible trajectory for a high energy heavy ion collision is indicated for orientation.

characterized by an order parameter that varies from one in the ordered phase to zero in the disordered phase. For example, phase transitions in water (i.e. solid (ice) liquid (water) and gas (vapor)) can be characterized using the density difference as an order parameter.

Phase transitions can be first or second order. A first order transition results in a discontinuous first derivative of the thermodynamic potential. If the thermodynamic potential's second derivative is divergent a second order phase transition occurs. The absence of a discontinuity in the derivatives of thermodynamical potential leads to cross-over phase transition.

In conjunction with the chiral symmetry arguments, first principles theoretical calculations predict a phase diagram similar to the one illustrated in Fig. 1.1. That is, for large μ_B and low temperature, the transition between hadronic matter and the QGP is first order [7–12]. However, for small μ_B values and high temperatures, a smooth crossover phase transition occurs [13, 14] such that it does not cross the singularity where the quark masses (chiral symmetry order parameter) become zero. Both transition domains, crossover, and the first-order are connected by the critical endpoint (CEP),

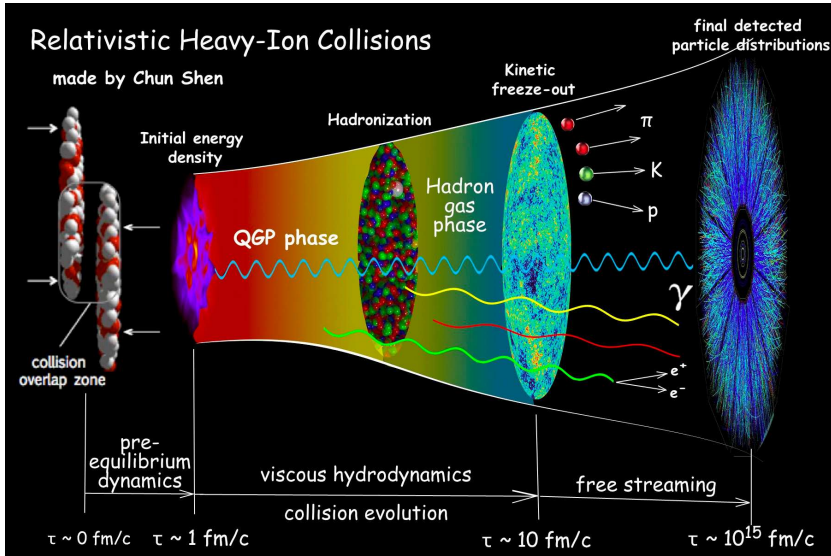


Fig. 1.2: Illustration of the time evolution of heavy ion collision. The figure is taken from Ref. [18].

at which the phase transition is expected to be second order.

1.2 The Quark Gluon Plasma

An important approach to furthering the study of QCD is to experimentally produce and study nuclear matter at extreme temperatures and pressures. Under such conditions, QCD theory predicts that, asymptotic freedom which makes the coupling strength between quarks and gluons weaker, leads to a fluid-like collection of quarks and gluons [15] indicated in Fig. 1.1. The resulting state of matter in which quark and gluon degrees of freedom are mostly freed is called Quark Gluon Plasma (QGP) [16]. That is, quarks and gluons are no longer confined within the dimensions of nucleons. The extraordinary conditions of temperature and pressure required to produce this state of matter, is produced in ion-ion collisions at relativistic energies [17], especially for heavy ions.

1.2.1 Space-time evolution of heavy ion collisions

In energetic heavy ion collisions, the quarks and gluons which reside inside the colliding nucleons, can be de-confined to produce a hot and dense QGP medium as illustrated in Fig.1.2. Before the collision, the two Lorentz contracted nuclei approach each other along the beam direction. Subsequently, they cross each other and the resulting interactions between the nucleons in the interaction region, drives the creation of a high energy density fireball. When this fireball is sufficiently hot, the QGP is created.

The QGP is expected to have a very short lifetime ($\sim 10 \text{ fm}/c$) [19] since it will rapidly expand and cool down, due to a high-pressure gradient between the medium and the external vacuum. As it cools down, the quarks and gluons recombine or hadronize to form a colorless hadronic gas. Further interactions can occur in this gas as it expands; the kinetic freeze-out of these hadrons occur when such interactions cease. The resulting free-streaming hadrons, which can be detected, encode important information about the properties of the QGP and the hadronic gas, as well as their expansion dynamics. Consequently, a major motivation for current heavy ion research is the possibility of obtaining profound insights on the phase structure and the properties of QCD matter at high temperature and non-zero baryon number density. Ongoing heavy ion research programs at RHIC [20] and the LHC [21], as well as future facilities at FAIR [22] and NICA [23] are at the leading edge of the experimental efforts designed to map the thermodynamic and transport properties of QCD matter.

1.2.2 Heavy-Ion collision experiments

Heavy-ion collisions were initially studied at the Lawrence Berkeley National Laboratory with the Bevatron accelerator experiment (BEVALAC) at the beam energy of 6 GeV, in early 1954. The BEVALAC projectile energy was not large enough to study the QGP. At Brookhaven National Laboratory in 1960, the Alternating Gradient Synchrotron (AGS) was the next major experimental facility for studying heavy-ion collisions [24]. The AGS started operating at an energy of 28 GeV and has enabled a wealth of studies. It is still in operation. The highest energy heavy-ion fixed target experiment was the Super Proton Synchrotron (SPS) at CERN [25]. The fixed target high energy collision experiments at the BEVALAC, AGS and SPS were not able to study the behavior of nuclear matter at the very extremes of high

energy-density.

In the summer of 2000 the Relativistic Heavy Ion Collider (RHIC) delivered Au beams with the primary objective of creating and studying the QGP. Subsequently, RHIC has provided excellent opportunities to fulfill this objective. The data collected at different energies by the Solenoidal Tracker at RHIC (STAR) has been used to observe and study many of the initially proposed signatures signaling the formation of the QGP in heavy-ion collisions. Today, the STAR experiment continues to provide valuable measurements designed to extend our understanding of hot and dense QCD matter. The measurements for Au+Au collisions span a broad range of collision energies. Data for other ion species including protons, He, Cu, U have also been obtained with the STAR experiment. In this dissertation several of these data sets were used in analyses' designed to gain further insights on the properties of the QGP.

1.2.3 The RHIC Beam Energy Scan Program

The RHIC Beam Energy Scan (BES) program leverages the the collider's capability of accelerating nuclei at different collision energies spanning the range $\sqrt{s_{NN}} = 7 - 200$ GeV. This is especially important to experimental studies of the QCD phase diagram since T and μ_B are known to vary with $\sqrt{s_{NN}}$ [26]. The variation of $\sqrt{s_{NN}}$ of the colliding nuclei, lead to different reaction trajectories in the phase diagram which could cross the phase boundary at different T and μ_B values as illustrated schematically in Fig.1.4. Such trajectories could also traverse $T - \mu_B$ regions close to the CEP. Therefore, studies involving measurements which span BES energies could give insights on the detailed structure of the phase diagram, as well as the properties of the respective QCD phases.

A major focus of the ongoing BES program is aimed at: (a) detailed studies of the QGP transport properties as a function of T and μ_B ; (b) the detection of signatures which signal the first order phase transition, and (c) the detection of experimental signatures which can aid identification and characterization of the QCD Critical End Point.

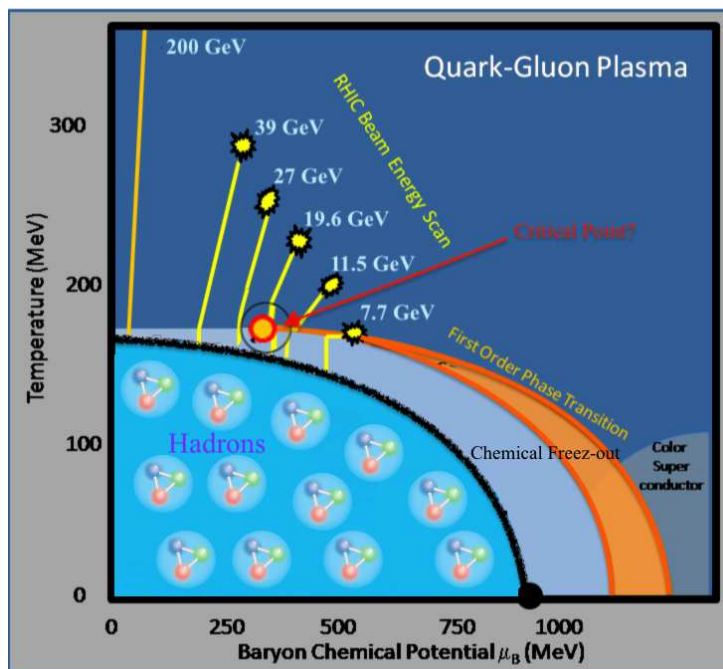


Fig. 1.3: Schematic illustration of the phase diagram of QCD matter with conjectured trajectories for several collision energies at RHIC. The yellow lines indicate the conjectured trajectories for Au+Au collisions for the beam energies indicated.

1.2.4 Essential concepts and definitions for heavy ion collisions

Given the focus of this work, a set of definitions and concepts important for navigating the ins and outs of heavy ion collisions is outlined as follows;

- Collision Geometry

When observed from the center of mass (CM) frame, two nuclei accelerated to highly relativistic speeds will appear as two flat pancakes due to Lorentz contraction along the beam direction. A schematic view of this picture is shown in Fig(1.4). The transverse radius of each nuclei can be estimated as $R = 1.2A^{1/3}$, where A is the atomic mass number. For Au ions, this radius is approximately 7.0 fm ($1 \text{ fm} = 10^{-15} \text{ m}$). Thus, extremely peripheral collisions have an impact parameter (the distance between the centers of the two colliding nuclei) of about 14.0

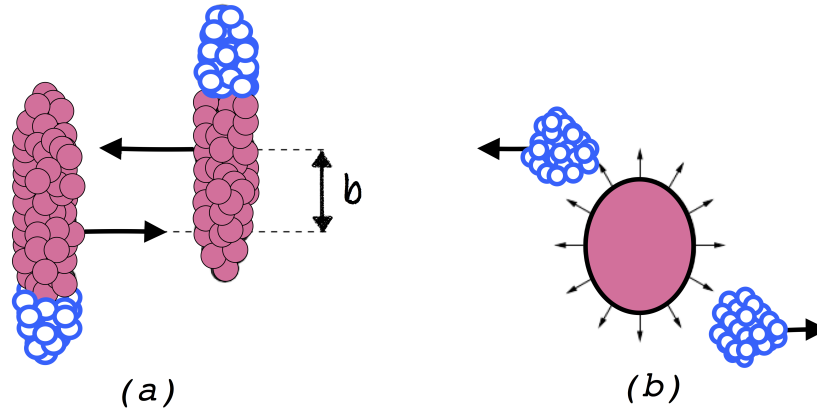


Fig. 1.4: Schematic illustration of a heavy ion collision seen from the CM frame. Panel (a) illustrates the definition of the impact parameter and panel (b) shows the participant and spectators (see text).

fm while central collisions have an impact parameter of 0.0 fm. This impact parameter (b) (c.f. Fig(1.4)) can not be measured directly and is typically estimated via the multiplicity of the produced particles. That is, central collisions ($b = 0$) lead to large multiplicities while peripheral collisions result in much smaller multiplicities. Fig(1.4) gives an illustration of two colliding nuclei, before and after the collision. The nucleons inside the overlap region (participants) leads to the creation of the fireball which expands and ultimately decays into particles. The nucleons outside of the overlap region (spectators) continue to move along their original trajectories and can also decay into particles if they have sufficient excitation energy.

- Kinematics

At RHIC, the coordinate system is such that the z -axis is parallel to the collision axis (beam axis); the x - and y -axes form a plane which is perpendicular to the z -axis and the y -axis is taken to be vertical pointing up. The nominal interaction point is at the $(0, 0, 0)$ -coordinate; the beams are tuned such that collisions take place at this point. However, collisions do not always occur exactly at the interaction point, so its actual location has to be measured. This location is called the primary vertex or just the vertex.

- Collision Energies

The energy in the CM frame can be calculated using the 4-vectors of the beams $E(E, 0, 0, p_z)$ as:

$$E_{CM} = \sqrt{(2E)^2} = 2E \quad (1.1)$$

I.e. twice the beam energy. Usually, the CM energy is denoted as $\sqrt{s_{NN}}$, where the subscript NN makes it clear that it is the CM energy per nucleon pair.

- Transverse momentum

Often the momentum is divided into a transverse component p_T , and a longitudinal component p_z . The transverse momentum has the advantage of being Lorentz invariant. It is defined as:

$$p_T = \sqrt{p_x^2 + p_y^2} \quad (1.2)$$

- Rapidity

The longitudinal momentum component p_z is rarely used by itself. More than often, it is used to define the rapidity, y , of a particle:

$$y = \ln \left[\frac{1}{2} \left(\frac{E + p_z}{E - p_z} \right) \right] \quad (1.3)$$

One of the advantages of the rapidity variable is that it is additively invariant under Lorentz transformations, while p_z is not

- Pseudorapidity

The rapidity (y) of a particle requires knowledge of the particle mass. However, this mass is not necessarily known experimentally, in which case the pseudorapidity variable η , is used:

$$\eta = -\ln \left[\tan\left(\frac{\theta}{2}\right) \right] \quad (1.4)$$

where $\tan(\theta) = \sqrt{x^2 + y^2}/z$. Since this reduces the variables into (x, y, z) coordinates, knowledge about the momentum of a particle is not necessary to calculate its pseudorapidity. For particles with $m \ll p$ the energy $E = \sqrt{m^2 + p^2} \rightarrow p$ and $y \rightarrow \eta$.

<i>Quantity</i>	<i>Conversion</i>	$\hbar = c = 1 \text{ units}$
<i>Mass</i>	$1 \text{ kg} = 5.61 \times 10^{26} \text{ GeV}$	GeV
<i>Length</i>	$1 \text{ m} = 5.07 \times 10^{16} \text{ GeV}^{-1}$	GeV^{-1}
<i>Time</i>	$1 \text{ s} = 5.61 \times 10^{26} \text{ GeV}^{-1}$	GeV^{-1}

Tab. 1.1: Mass, length and time in Natural units.

- Multiplicity

The multiplicity is defined as the number of particles emitted in a given collision event. Usually, multiplicity will refer only to the number of charged particles. The multiplicity is often measured differentially as a function of pseudorapidity, $dN/d\eta$.

- Units and conversion factors

In this thesis, all quantities are measured and expressed in terms of natural units as shown in table 1.1.

Some other conversion factors often used in heavy-ion physics:

(a) $1 \text{ fm} = 10^{-15} \text{ m} = 5.07 \text{ GeV}^{-1}$

(b) $1 \hbar c = 197 \text{ MeV fm}$

1.3 Anisotropic Flow

A major focus of this dissertation is the presentation of new flow measurements, as well as their use to gain insight on both reaction dynamics and the transport properties of the QGP produced in relativistic heavy ion collisions. In such collisions, the interaction zone, where the initial nucleon-nucleon interactions occur, is elliptical for non-central collisions - see Fig. 1.5. If QGP develops in this interaction zone, then the pressure gradients which develop as a result of the initial spatial anisotropy, drives an anisotropic expansion of the fireball which leads to an azimuthal momentum anisotropy of the particles emitted subsequent to hadronization. This anisotropic flow of the emitted particles, not only reflect the Equation of State (EOS) of QCD matter, but also the transport coefficients which influence the magnitude of the flow-driven anisotropy.

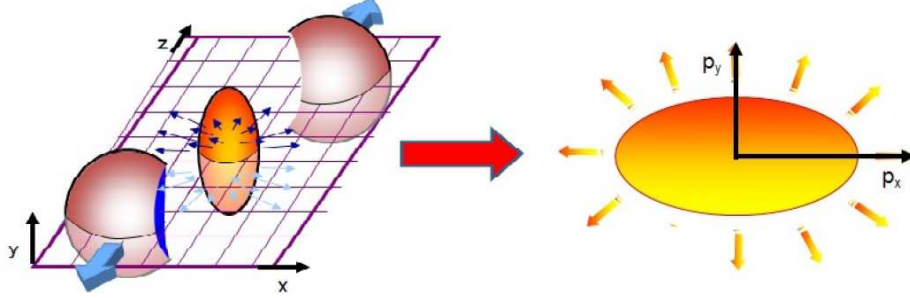


Fig. 1.5: Example of a standard non-central heavy-ion collision in which the eccentric shape of initial collision geometry is transposed into the elliptic flow anisotropy in the final state momentum space. Figure taken from [27].

Experimentally, this anisotropic flow is usually characterized via a Fourier expansion of the azimuthal distribution of the emitted particles:

$$E \frac{d^3 N}{d^3 p} = \frac{1}{2\pi} \frac{d^2 N}{p_T dp_T dy} \left(1 + 2 \sum_{n=1}^{\infty} v_n \cos[n(\phi - \Psi_n)] \right), \quad (1.5)$$

where E is the energy, p is the momentum, p_T is the transverse momentum, ϕ is the azimuthal angle and y is the rapidity of the particle respectively. Ψ_n is the n^{th} -order event plane and v_n is the n^{th} -order flow coefficients; v_1 , v_2 and v_3 are called directed flow, elliptic flow and triangular flow respectively.

In the last decade, the v_2 coefficient which is dominated by asymmetries related to the initial elliptic shape of the collision zone, has received a lot of experimental and theoretical attention [28, 29]. More recently it was realized that higher odd and even anisotropic flow coefficients are also important, and are more sensitive to the transport coefficients. In this dissertation, a comprehensive set of new measurements of both odd and even harmonics will be presented and studied.

1.4 Scope and Organization of this thesis

In this thesis, I will present and discuss new measurements of anisotropic flow and its fluctuations, for Au+Au collisions at all BES energies, as well as d+Au, Cu+Cu and Cu+Au at $\sqrt{s_{NN}} = 200$ GeV, and U+U at $\sqrt{s_{NN}}$

= 193 GeV. The beam energy dependent measurements provide important constraints for the extraction of the specific viscosity η/s (the ratio of shear viscosity to entropy density) as well as its T and μ_B dependence. In turn the measurements for different collision systems provide stringent constraints for initial-state models.

The organization of this thesis is as follows:

Chapter 2 gives a brief outline of the RHIC accelerator facility and the detector setup employed for the measurements. In chapters 3 and 4 the data analysis method is presented with emphasis on the two- and multi-particle correlation techniques [30–34] employed for the anisotropic flow measurements. The detailed results from these analysis techniques, for all collision systems and beam energies are also presented. In chapter 5, detailed measurements of the two-, four- and six-particle elliptic flow harmonic, as well as elliptic flow fluctuations are presented and discussed. Chapter 6 summarizes the main findings of this thesis and gives further in-depth discussions on the results obtained. An outlook for the future studies is also presented.

Chapter 2

Experimental Setups and Data Sets

The measurements presented in this thesis were conducted with d+Au, Cu+Cu and Cu+Au collisions at $\sqrt{s_{NN}} = 200$ GeV, U+U collisions at $\sqrt{s_{NN}} = 193$ GeV and Au+Au collisions at $\sqrt{s_{NN}} = 7.7$ -200 GeV. The beams were provided by the Relativistic Heavy Ion Collider and the data were collected with the STAR detector[35, 36].

2.1 Relativistic Heavy Ion Collider

The Relativistic Heavy Ion Collider (RHIC) [37] is located at Brookhaven National Laboratory in Upton, New York on Long Island. RHIC is a versatile collider capable of accelerating various species of ions over a broad range of energies. The two primary physics programs at RHIC are spin physics[38], using polarized protons, and “heavy ion” physics. For the heavy ion program, data has been collected for p+p, p+Au, d+Au, $^3\text{He}+\text{Au}$, Cu+Cu, Cu+Au, Au+Au and U+U collisions at several beam energies. Data has also been collected for a beam energy scan involving Au+Au collisions. As Fig(2.1) shows, there are six interaction points on RHICs 3.8 km ring where collisions can occur. Measurements have been performed at four of these interaction points by the STAR experiment at 6 clock, the PHENIX experiment at 8 clock, the PHOBOS experiment at 10 clock, and the BRAHMS experiment at 1 clock. The PHOBOS, BRAHMS and PHENIX experiments completed their experimental missions in 2005, 2006 and 2017 respectively. The data reported

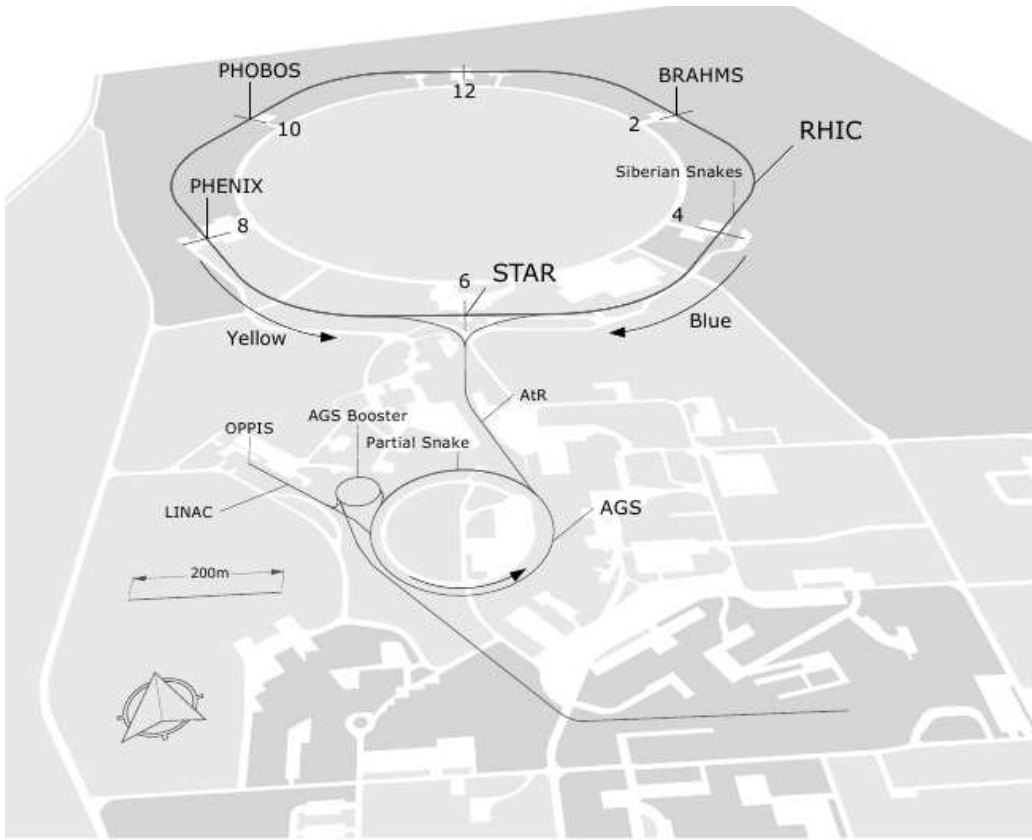


Fig. 2.1: The RHIC accelerator complex at Brookhaven National Laboratory.

in this work were obtained with STAR experiment which still maintains an active experimental program at RHIC.

The BNL accelerator complex consists of an ion source and several accelerators [37] which the Ions go through before they enter the RHIC ring where the ions are further accelerated and made to collide. Several of the major components of the accelerator complex are briefly described below:

- Linear Accelerator
 In 1971 the Brookhaven Linear Accelerator (Linac) was built as an upgrade to the Alternating Gradient Synchrotron (AGS). Presently, the Linac is the main source of the polarized and/or high intensity proton beams injected into RHIC.
- Tandem Van de Graaff

For many years the Tandem Van de Graaff was the largest electrostatic facility. It has the ability to produce a wide range of ion species spanning the full range from hydrogen to uranium.

- Tandem-to-Booster line
The TtB line is a beam transport system. The TtB line is situated in a 700-meter-long tunnel. The TtB delivers heavy ions from the Tandem to the AGS for further acceleration. This line is critical for moving ions from the Tandem to RHIC.
- Electron Beam Ion Source
The EBIS is the ion source for RHIC. It creates ion beams from the lightest to the heaviest elements. These ions are injected into RHIC after acceleration by the Linac, Booster and the AGS.
- Booster Accelerator
The Booster is an important part of AGS with size less than a quarter of AGS operated by Collider-Accelerator Department. The Booster receives heavy ions from EBIS or protons from the Linac. It then pre-accelerates particles and injects them into the AGS ring.
- Alternating Gradient Synchrotron
The AGS is the final and most important part in the injector chain. It receives beam from Booster and accelerates it before releasing it to the two RHIC accelerator ring.
- AGS-to-RHIC Line
The AGS-to-RHIC (ATR) line is the last platform for the beam before entering the RHIC ring. The characterization of the beam extracted from AGS is done in this transfer line. At the end of this line a switching magnet gives direction to the ion bunches either in clockwise or in anti-clockwise direction.
- RHIC Ring
The RHIC ring consists of two independent rings called Blue and Yellow rings which accelerate ions clockwise and counter clockwise in each ring respectively. There are six interaction point in the ring where the these beams can be tuned to collide.

Solenoidal Tracker At RHIC : $-1 < \eta < 1, 0 < \phi < 2\pi$

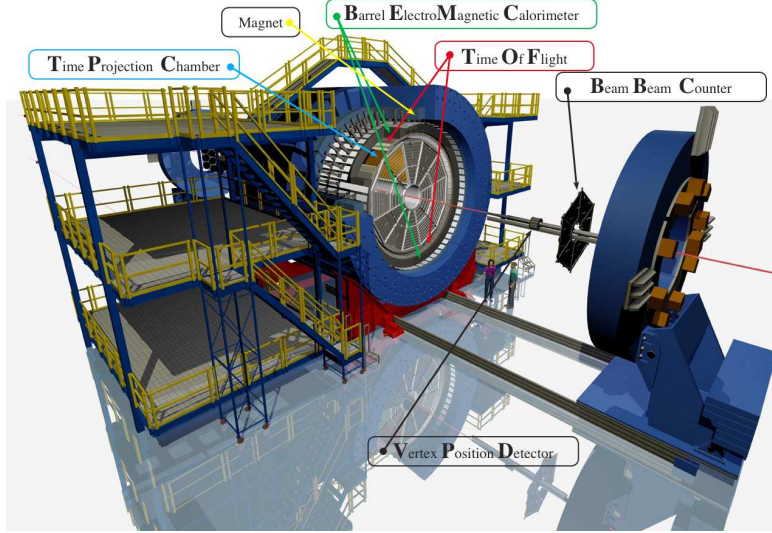


Fig. 2.2: A perspective view of the STAR detector system with a cutaway for viewing the inner sub-systems.

2.2 STAR Detector

The Solenoidal Tracker at RHIC (STAR) detector Fig. 2.2 has various detector subsystems. In the STAR coordinate system, the z -axis is along the beam direction as shown in Fig. 2.2. The applied magnetic field in the z -direction from the STAR magnet bends the trajectories of charged particles enabling momentum measurements. This magnet can be maintained at magnetic fields of $0, \pm 0.25$ or ± 0.5 Tesla. The Time Projection Chamber (TPC) [39], is the main tracking detector and is capable of measuring charged particles within $|\eta| < 1.8$ and full azimuthal coverage in the $x - y$ plane. In 2010, a barrel Time-of-Flight (TOF) detector [40] based on Multi-gap Resistive Plate Chamber (MRPC) technology was fully installed in STAR. The TOF consists of a total of 120 trays spanning a pseudo-rapidity range $|\eta| < 0.9$ with full azimuthal coverage. The TPC, and the TOF are the main sub-systems of the STAR detector used for the measurements presented in this thesis. Both subsystems are briefly discussed in the following.

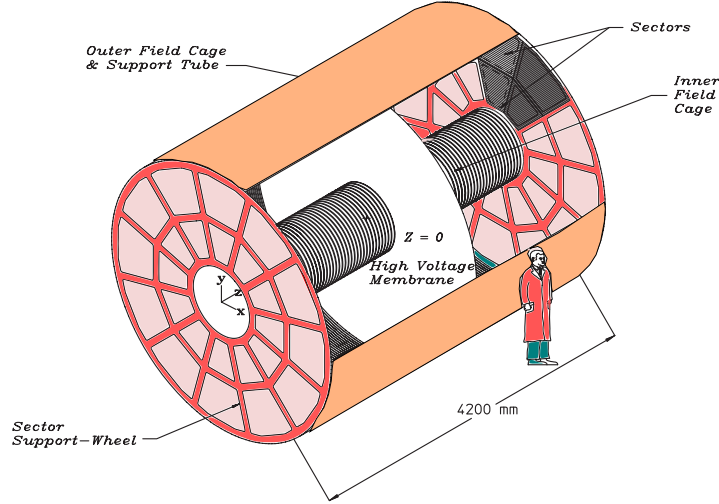


Fig. 2.3: The diagram of STAR Time Projection Chamber at RHIC.

2.2.1 Time Projection Chamber (TPC)

The TPC is the main tracking detector at STAR [39]. The TPC tracks charged particles via the ionization trail that they leave in the volume of the TPC; it measures particle momentum and charge and facilitates particle identification over a limited p_T range. It is 4-meters in diameter and 4.2-meters long, providing coverage of $-1 < \eta < 1$ with high-quality tracking. For a magnetic field of 0.5 Tesla in the z -direction, the TPC can measure particles with momentum larger than $150 \text{ MeV}/c$. Fig.(2.2.1) shows the thin conductive Central Membrane, the concentric field cage cylinders, and two end caps which provide a nearly uniform electric field along the beam (z) direction in the TPC. The TPC is filled with P10 gas (90% Ar + 10% CH₄) which provides a stable electron drift velocity that is insensitive to small variations of temperature and pressure.

When a charged particle crosses the TPC's volume, it ionizes the gas atoms and the ionized electrons drift in the electric field to the anode in the Multi-Wire Proportional Chambers at the end cap readout. The current collected by the wires gives the hit location in the $x-y$ plane and the current amplitude is proportional to the ionization energy loss. The drift time gives

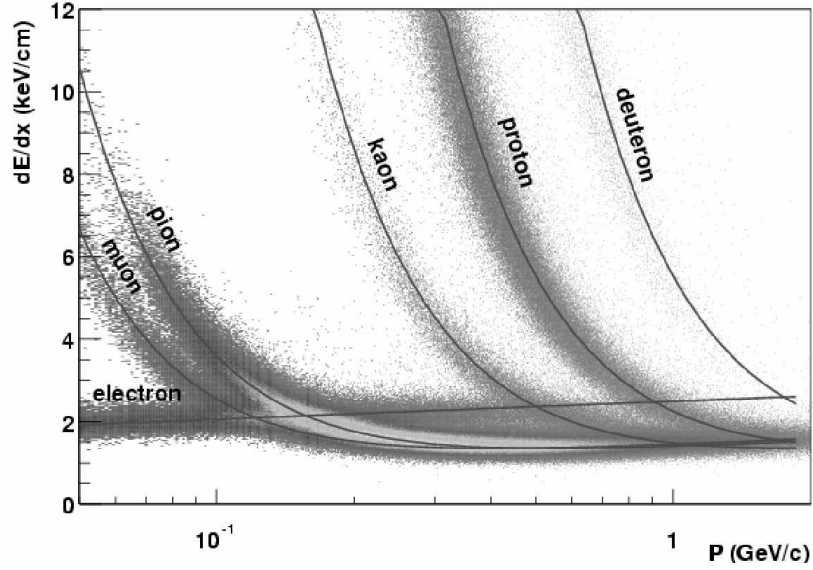


Fig. 2.4: The energy loss distribution for primary and secondary particles in the STAR TPC as a function of the momentum of the primary particles [39].

the z coordinate of the hit location. Using the hit point coordinates (x, y, z) the helix of a particle's motion can be reconstructed. The particle's helix is used in conjunction with the magnitude of the STAR magnetic field to determine its momentum and the sign of its charge via the Lorentz force equation of motion.

The energy loss (dE/dx) is proportional to the number of electrons measured for that track at each hit. Thus, by carefully calibrating the TPC track's, dE/dx can be measured. Fig. 2.6 shows the measured dE/dx of tracks as a function of total momentum. Clear separation can be seen between the tracks of different species at low momenta. However, the merger of the energy loss bands at high momenta require an alternative method for particle identification at higher momenta.

2.2.2 Time Of Flight (TOF)

One of the important upgrades of the STAR detector is the Time of Flight (TOF) detector which increases STAR's particle identification capability over an extended momentum range [40]. The TOF detector was installed in 2010. As its name proposes, TOF measures the time of flight of a charged particles, starting from the collision vertex, as it traverses the TPC and hits the TOF detector itself. The detectors timing resolution of ~ 100 ps serve to extend the momentum range for particle identification.

The TOF system consists of two sub-systems: the upgraded pseudo-Vertex Position Detector (up-VPD) and the TOF detector itself. The up-VPD detector is designed to measure the collision time of an event with a resolution of 10-20 ps. The up-VPDs are placed around the beam pipe and are located at $z = \pm 5.7$ m away from the center, covering $4.24 < |\eta| < 5.1$. The up-VPD measures the start time (t-start) of the charged particles. The TOF measures the stop time (t-stop) or time of flight, i.e., $\Delta t = (t_{stop} - t_{start})$.

In general one can write the reciprocal speed of a particle as;

$$\frac{1}{\beta} = \frac{\Delta t}{L} = \sqrt{\frac{m^2 + p^2}{p^2}}, \quad (2.1)$$

which gives the mass of the particle as;

$$m^2 = \frac{p^2}{(\beta\gamma)^2} = p^2 \left(\frac{(c\Delta t)^2}{L^2} - 1 \right), \quad (2.2)$$

where

$$\begin{aligned} \Delta t &= \text{Time of Flight} \\ L &= \text{Path Length} \\ p &= \text{Momentum} \\ \gamma &= \text{Gamma Factor} \end{aligned}$$

The computed masses of the particles can then be used for particle identification. Fig. 2.2.2 shows the computed m^2 vs. particle momentum multiplied by the particle charge, for different measured tracks. The various species are clearly discernible over a wide range of momenta. However, it is apparent that they become indistinguishable as their momenta become larger than their mass and their velocities approach the speed of light.

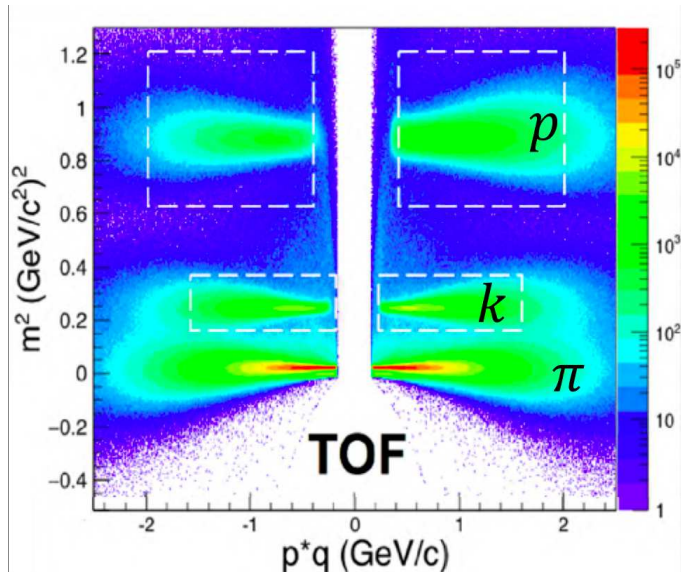


Fig. 2.5: m^2 vs. total momentum multiplied by the particle charge q [41]. m^2 is computed with the time of flight measurements obtained with the TOF detector.

2.3 Centrality Definition in Heavy-Ion Collisions

The impact parameter b of a collision measures the distance between the centers of two colliding nuclei. It varies from event to event and ranges from central collision with $b = 0$ leading to complete area overlap (for symmetric systems) to peripheral collision with large b values corresponding to a small overlap zone. Experimentally, the full range of b values are obtained in collisions spanning very many events. Each of these b values can be linked to a corresponding multiplicity distribution for charged tracks. Therefore, cuts on the total multiplicity distribution can be used to select b or the centrality of the collisions. The calibration for these cuts is usually obtained via a Glauber Model [42].

For a given b , the Glauber Monte Carlo model generates the distribution of nucleons which collide, assuming that nucleons are moving in straight lines, and each N+N collision occurs independently. Each nucleon in a nucleus interacts with the nucleons in the other nucleus in their path. The N+N

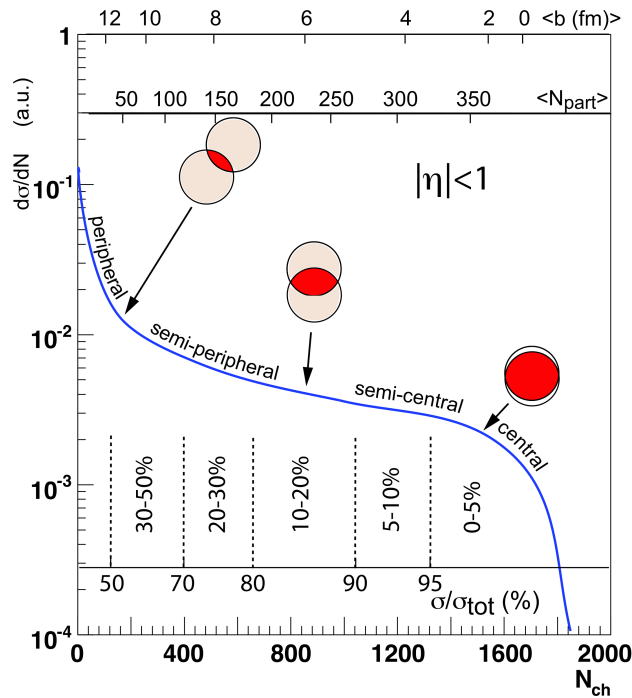


Fig. 2.6: Illustration of the calibrated relationship between Glauber Model parameters (b , N_{part}) and the number of charged tracks. The figure taken from Ref. [42]

collisions occur when the distance of nucleons are within a range fixed by the $N+N$ inelastic cross section. In this way, the model is able to give estimates of the total number of collisions N_{coll} , that occur, as well the number of nucleons which participate in the collision N_{part} , for a given b . The model also gives other initial-state geometric quantities such as the eccentricity. A primary assumption for the calibration is that track multiplicity should be a monotonic function of the impact parameter b . Fig.(2.6) illustrate the centrality selections which are obtained from a calibration of the measured inclusive charged particle tracks. Note that the larger the multiplicity, the smaller the value of b . The dashed lines show typical centrality binning.

Collision system	Collision energy	Run	Vertex Cut	
			$ V_z <$	$V_r = \sqrt{V_x^2 + V_y^2} <$
<i>Cu + Cu</i>	200 GeV	5	40	2
<i>Cu + Au</i>	200 GeV	12	30	2
<i>U + U</i>	193 GeV	12	30	2
<i>Au + Au</i>	200 GeV	11	30	2
<i>Au + Au</i>	62.4 GeV	4	30	2
<i>Au + Au</i>	54 GeV	17	30	2
<i>Au + Au</i>	39 GeV	10	40	2
<i>Au + Au</i>	27 GeV	11	40	2
<i>Au + Au</i>	19.6 GeV	11	40	2
<i>Au + Au</i>	14.5 GeV	14	40	1
<i>Au + Au</i>	11.5 GeV	10	50	2
<i>Au + Au</i>	7.7 GeV	10	70	2

Tab. 2.1: The run year and the vertex cut used for the different collision systems and energies studied in this thesis.

2.4 Data Sets

In this section the data sets used in this thesis, as well as the event and track cuts used in subsequent analyses⁷ are presented. Table 2.4 gives a summary of this information for all systems and energies.

One set of track cuts was used for all systems and energies. These cuts are summarized in Table. 2.4.

Quantities	The cut used
DCA	< 3.0
$ \eta $	≤ 1.0
p_T (GeV/c)	> 0.2 < 4.0
Minimum number of TPC hist	15

Tab. 2.2: Track-cuts used in subsequent analyses’.

Chapter 3

Flow Analysis Methodology

In the last decade, significant effort, both experimental and theoretical, has gone towards studying the transport properties of the hot and dense matter created in heavy ion collisions using the anisotropic flow coefficients v_n [29, 43–71]. In this chapter anisotropic flow and its associated coefficients v_n , are introduced. The analysis methods for the extraction of the v_n coefficients are also discussed.

3.1 Anisotropic Flow

In this section, we will start by first outlining the traditional definition for the anisotropic flow harmonics v_n . The azimuthal distribution, $r(\phi)$, of the total transverse momentum of particles produced in a heavy-ion collision, is a periodic quantity and it is reasonable to expand it in a Fourier series as:

$$r(\phi) = \frac{x_0}{2\pi} + \frac{1}{\pi} \sum_{n=1}^{\infty} [x_n \cos(n\phi) + y_n \sin(n\phi)], \quad (3.1)$$

where,

$$x_n = \int_0^{2\pi} r(\phi) \cos(n\phi) d\phi, \quad (3.2)$$

$$y_n = \int_0^{2\pi} r(\phi) \sin(n\phi) d\phi \quad (3.3)$$

For each Fourier coefficient, x_n and y_n , we can define the corresponding n^{th} order flow harmonic, v_n , as:

$$v_n = \sqrt{x_n^2 + y_n^2}. \quad (3.4)$$

For symmetric collisions with equal probability for particles to be emitted in the ϕ and $-\phi$ directions, the average of the $\sin(n\phi)$ contribution will always cancel, $y_n = 0$. Also the equal probability for particles to be emitted in directions of ϕ and $\phi + \pi$ will lead to $x_n = \langle \cos(n\phi) \rangle = 0$ for the odd harmonics.

$$\cos(n\phi) + \cos(n(\phi + \pi)) = \cos(n\phi)[1 + (-1)^n] = 0 \text{ for odd } n \quad (3.5)$$

These symmetries lead to the flow harmonics v_n being equal to x_n , which are non-zero for even harmonics. The n^{th} harmonic can be related to the starting distribution $r(\phi)$ as:

$$\langle \cos(n\phi) \rangle = \frac{\int_0^{2\pi} r(\phi) \cos(n\phi) d\phi}{\int_0^{2\pi} r(\phi) d\phi}. \quad (3.6)$$

By using a normalized distribution for $r(\phi)$ for which $\int_0^{2\pi} r(\phi) d\phi = 1$, we can write

$$\langle \cos(n\phi) \rangle = \frac{1}{\pi} v_n \int_0^{2\pi} \cos(n\phi)^2 d\phi, \quad (3.7)$$

using the orthogonality relationship of the cosine functions,

$$\int_0^{2\pi} \cos(n\phi) \cos(m\phi) d\phi = \pi \delta_{nm}, \quad (3.8)$$

where δ_{nm} is the Kronecker delta function. Therefore,

$$v_n = \langle \cos(n\phi) \rangle \quad (3.9)$$

The orientation of the impact parameter vector b (the vector connecting the centers of two colliding nuclei) changes event-by-event in heavy-ion collisions, which in turn yields a random reaction plane angle Ψ_R (the plane spanned by the impact parameter and the beam axis z see Fig. 3.1. Due to these random orientations, it is useless to measure the azimuthal angles in

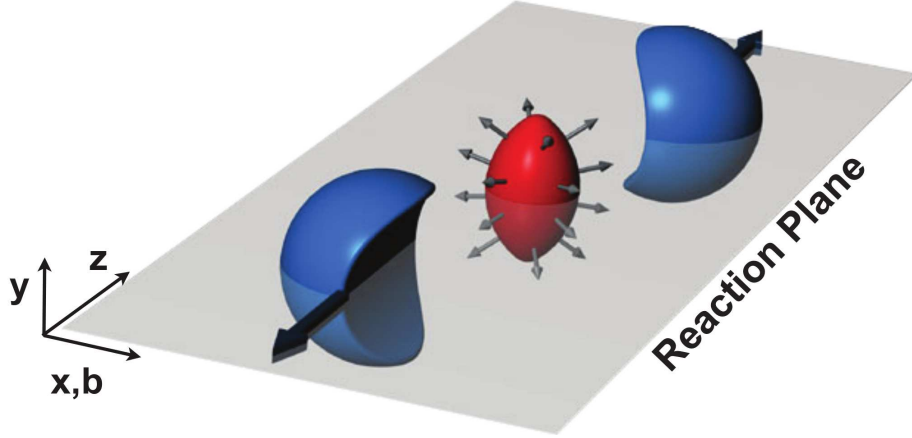


Fig. 3.1: A representation of the formation of almond-shaped interaction volume created in mid-central collision of two nuclei. The spatial anisotropy of the interaction volume with respect to reaction-plane (x-z plane), leads to a momentum anisotropy of the produced particles.

a fixed coordinate system in the laboratory. Therefore Eq.(3.9) is not much used in the v_n measurements. The way to avoid this problem is to use observables which are sensitive only to flow harmonics v_n but do not require the knowledge of reaction plane orientation event-by-event. Such observables will be discussed, but more on that later.

In addition to the spatial anisotropy (c.f. Fig. 3.1) which stems from the collision geometry, there are also the anisotropies arising from the fluctuations in the initial positions of participating nucleons within the created system[72]. This fluctuation can in principle, generates anisotropy in coordinate space, which will be also transferred to momentum space, where they can give rise to the harmonics v_n . To understand more the fluctuations effects on the anisotropic flow analysis we will need to rewrite Eq.(3.1) by using the well-known identities:

$$\begin{aligned}\cos(n\phi) &= \frac{1}{2}(e^{in\phi} + e^{-in\phi}), \\ \sin(n\phi) &= \frac{1}{2i}(e^{in\phi} - e^{-in\phi}),\end{aligned}\tag{3.10}$$

then,

$$\begin{aligned}
v_n &= x_n - iy_n, \quad n > 0, \\
&= x_n + iy_n, \quad n < 0, \\
&= x_0, \quad n = 0.
\end{aligned} \tag{3.11}$$

Using Eq.(3.10) we can rewrite Eq.(3.1) as,

$$\begin{aligned}
r(\phi) &= \frac{x_0}{2\pi} + \frac{1}{2\pi} \sum_{n=1}^{\infty} (x_n - iy_n) e^{in\phi} + \frac{1}{2\pi} \sum_{n=1}^{\infty} (x_n + iy_n) e^{-in\phi}, \\
&= \frac{x_0}{2\pi} + \frac{1}{2\pi} \sum_{n=1}^{\infty} (x_n - iy_n) e^{in\phi} + \frac{1}{2\pi} \sum_{n=-\infty}^{-1} (x_{-n} + iy_{-n}) e^{in\phi}, \tag{3.12}
\end{aligned}$$

by inserting the definitions Eq.(3.11),

$$r(\phi) = \frac{v_0}{2\pi} + \frac{1}{2\pi} \left\{ \sum_{n=1}^{\infty} v_n e^{in\phi} + \sum_{n=1}^{\infty} v_{-n}^* e^{-in\phi} \right\}, \tag{3.13}$$

where v_n in general is complex, so we can use $v_n = v_{-n}^*$:

$$r(\phi) = \frac{v_0}{2\pi} + \frac{1}{\pi} \sum_{n=1}^{\infty} \text{Re}\{v_n e^{in\phi}\}. \tag{3.14}$$

Since v_n is complex, and in general each harmonic can be defined relative to its own symmetry plane (the so called participant plane) Ψ_n as $v_n \equiv |v_n| e^{-in\Psi_n}$.

$$\begin{aligned}
r(\phi) &= \frac{v_0}{2\pi} + \frac{1}{\pi} \sum_{n=1}^{\infty} |v_n| \text{Re}\{e^{in(\phi - \Psi_n)}\}, \\
r(\phi) &= \frac{v_0}{2\pi} + \frac{1}{\pi} \sum_{n=1}^{\infty} v_n \cos[n(\phi - \Psi_n)]
\end{aligned} \tag{3.15}$$

Therefore, anisotropic flow analysis in the general case, requires the measurement of both Ψ_n and v_n . By generalizing Eq.(3.9) one can show straightforwardly that:

$$v_n = \langle \cos[n(\phi - \Psi_n)] \rangle, \tag{3.16}$$

The harmonic v_1 is called directed flow, the harmonic v_2 elliptic flow, the harmonic v_3 triangular flow, etc. When v_n are considered as a function of transverse momentum or rapidity, we refer to them as differential flow harmonics.

In this thesis the two-particle mixed-events method [30] as well as the multi-particle correlation (cumulant) method [31–34] are used. Both methods are discussed in the following sections.

3.2 Two-Particle Azimuthal Correlations (Event-Mixing Technique)

All techniques used to extract v_n are related to the azimuthal correlation function that can be expressed as,

$$C(\Delta\phi, \Delta\eta) = \frac{(dN/d\Delta\phi)_{Same}}{(dN/d\Delta\phi)_{Mix}} \quad (3.17)$$

$$\Delta\phi = \phi_a - \phi_b \quad (3.18)$$

$$\Delta\eta = \eta_a - \eta_b \quad (3.19)$$

where $(dN/d\Delta\phi)_{Same}$ is the azimuthal distribution of charged hadron pairs from the *same* event and $(dN/d\Delta\phi)_{Mix}$ is the azimuthal pair distribution for particles from different events belonging to the same class; $\Delta\phi$ is the azimuthal angle difference for particle pairs. Event classes, which retain the residual detector single particle relative efficiencies etc., eliminate the genuine two-particle physics correlations. To optimize mixing, events are pooled into classes to ensure similar global characteristics for same-event and mixed-event tracks. Twenty V_z classes and ten centrality classes were used. A pool depth of ten events was employed for mixing.

The Fourier coefficients v_{nn} , used to characterize the magnitude of the azimuthal anisotropy, are obtained from the correlation function as,

$$v_{nn} = \frac{\sum_{\Delta\phi} C(\Delta\phi, \Delta\eta) \cos(n\Delta\phi)}{\sum_{\Delta\phi} C(\Delta\phi, \Delta\eta)}, \quad (3.20)$$

where $C(\Delta\phi, \Delta\eta) = \frac{(dN/d\Delta\phi)_{Same}}{(dN/d\Delta\phi)_{Mix}}$. The two-particle correlations contain

flow, as well as so-called non-flow (NF) contributions [30, 73–75]:

$$v_{nn}(a, b) = v_n(a)v_n(b) + \delta_{NF}, \quad (3.21)$$

where δ_{NF} include contributions from resonance decays, Bose-Einstein correlations, jets, and global momentum conservation (GMC). This non-flow can be classified into both a short- and a long-range component. The suppression of both components is required for reliable v_n measurements.

3.2.1 Suppression of short range non-flow effects

The short-range non-flow, typically involving particles emitted within a localized region in η , is dominated by resonance decays and Bose-Einstein correlations. Since resonance decays often lead to unlike-sign charged pairs, one expects the correlations for such pairs to be influenced by short-range non-flow effects. For Bose-Einstein correlations, one expects the correlations for like-sign pairs to be similarly influenced. Since $\Delta\eta$ cuts enforce a separation between same-sign and unlike-sign particle pairs, such cuts can suppress resonance decays and reduce the influence of Bose-Einstein correlations. Therefore, studies of the influence of $\Delta\eta$ cuts on like-sign and unlike-sign correlation functions and their associated v_n values, can provide unique constraints for the cuts required to suppress short-range non-flow effects.

Representative examples of the correlation function for like-sign and unlike-sign charged particle pairs are shown in Figs. 3.2 and 3.3 for 0–5%, 40–50% and 70–80% central Au+Au collisions ($\sqrt{s_{NN}} = 200$ GeV) for several $|\Delta\eta|$ selections as indicated. The solid lines in the figures represent the fit function:

$$C_r = A \left(1 + 2 \sum_n v_{nn} \cos(n\Delta\phi) \right), \quad (3.22)$$

where A is a constant and v_{nn} is the product n^{th} -order flow harmonic. These correlation functions reflect both flow and non-flow contributions, as well as some residual detector/tracking effects. The latter effects are especially evident in the central collisions (Figs. 3.2(a) and 3.3 (a)) where a dip and a peak in the correlation function at $\Delta\phi \sim 0$ is evident. We attribute the dip (peak) to track merging (splitting) effects.

The short-range non-flow contributions and the residual detector effects (track merging/splitting) are expected to dominate at small $\Delta\eta$. This is

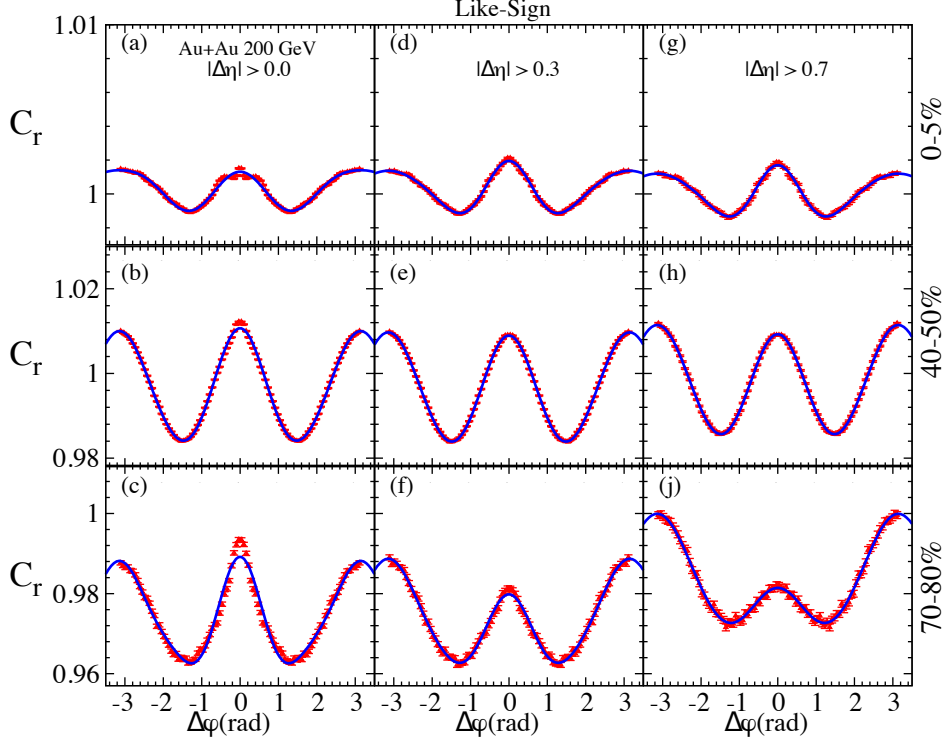


Fig. 3.2: Like-sign two-particle correlation function for 0 – 5%, 40 – 50% and 70 – 80% central Au+Au collisions at $\sqrt{s_{NN}} = 200$ GeV for different $\Delta\eta$ cuts.

confirmed by the correlation functions shown in Figs. 3.2 (a, b and c) and 3.3 (a, b and c), which were generated for the full $\Delta\eta$ range for both like-sign (LS) and unlike-sign (US) charged hadron pairs. They indicate that the distortions which result from non-flow contributions and detector effects persist over different ranges of centrality selections.

To suppress these distortions, the correlation functions were studied as a function of $\Delta\eta$ cut, for several centrality selections, over the full span of beam energies. This comprehensive study indicated that the cut $|\Delta\eta| > 0.7$ leads to significant suppression of track merging/splitting and non-flow contributions, while allowing reasonable statistical significance for our study over the full beam energy range. Here, it is noteworthy that a large $|\Delta\eta|$ leads to a significant reduction in the available statistics, especially for the lower beam

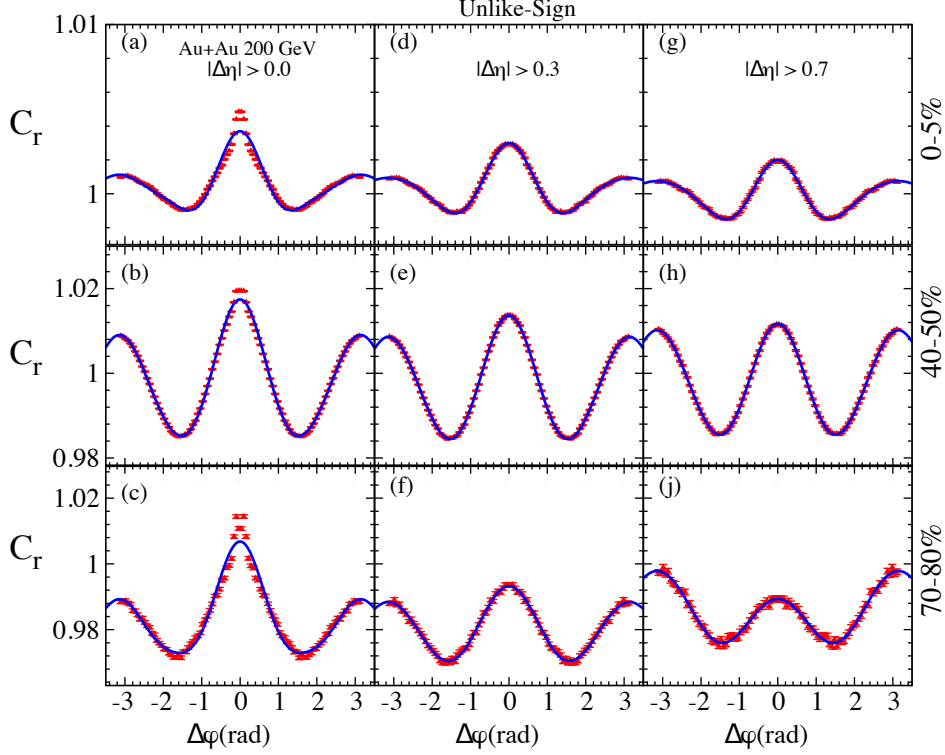


Fig. 3.3: Unlike-sign two-particle correlation functions for 0–5%, 40–50% and 70–80% central Au+Au collisions at $\sqrt{s_{NN}} = 200$ GeV, for different $|\Delta\eta|$ cuts.

energies. The representative set of correlation functions shown in Figs. 3.2 and 3.3 (g, h and j) clearly indicate that the distortions are suppressed for $|\Delta\eta| > 0.7$.

A further study, involving LS and US charged hadrons was employed to validate the effectiveness of the $|\Delta\eta|$ cut for suppressing short-range non-flow contributions and to estimate their influence on the magnitude of the extracted values of v_n . Here, the essential idea is that the LS and US selections can be used to enhance the respective short-range contributions due to HBT, Resonance decay, Jet-like correlation, etc. We use the similarity between the v_n values extracted from LS and US correlation functions as a figure of merit for the suppression of short-range non-flow contributions.

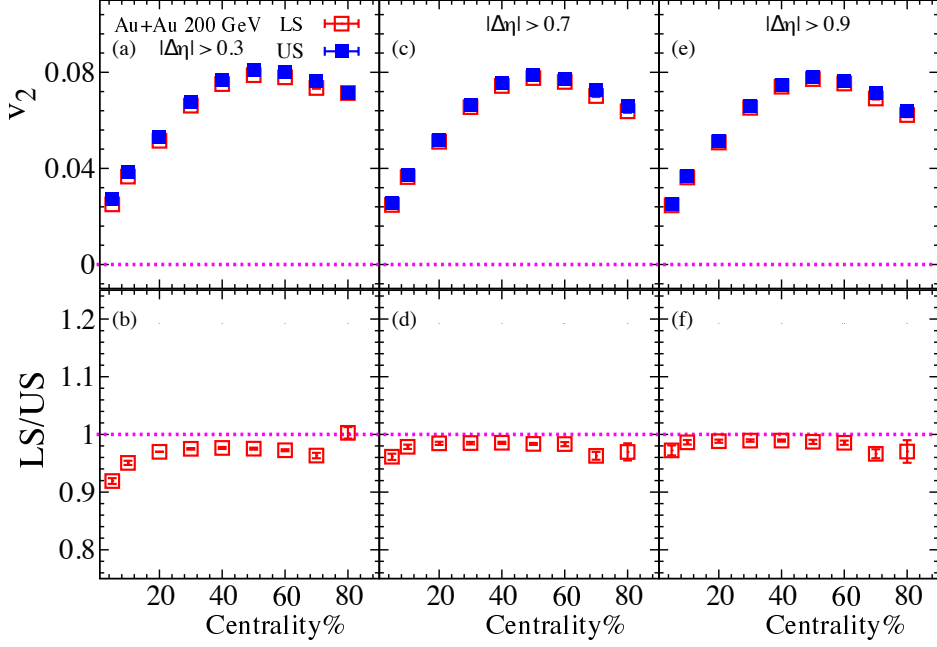


Fig. 3.4: Comparison of LS- and US- v_2 values for Au+Au collisions at $\sqrt{s_{NN}} = 200$ GeV. Results are shown for $|\Delta\eta| > 0.3, 0.7$ and 0.9 respectively.

For each beam energy, correlation functions were generated for several $|\Delta\eta|$ selections for both LS and US charged hadrons. The resulting correlation functions were then Fourier analyzed (cf. Eqs. 3.83 and 3.84) to obtain $v_n(\text{cent})$ for further comparisons. Representative results from this study are shown for Au+Au collisions at $\sqrt{s_{NN}} = 200$ GeV in Figs. 3.4, 3.5 and 3.6. The bottom panels in these figures give the ratio (LS/US) of the v_n values shown in the top panels.

The comparisons shown in Figs. 3.4, 3.5 and 3.6 (a) for LS- and US- v_n for $|\Delta\eta| > 0.3$, indicate clear differences which vary with centrality. We attribute these differences to the influence of short-range non-flow contributions. Figs. 3.4, 3.5 and 3.6 (b) show that these differences are significantly reduced for $|\Delta\eta| > 0.7$, confirming the utility of this cut for suppressing non-flow contributions. Figs. 3.4, 3.5 and 3.6 (c) indicate that a further increase to $|\Delta\eta| > 0.9$ leads to little, if any, improvement in the agreement between

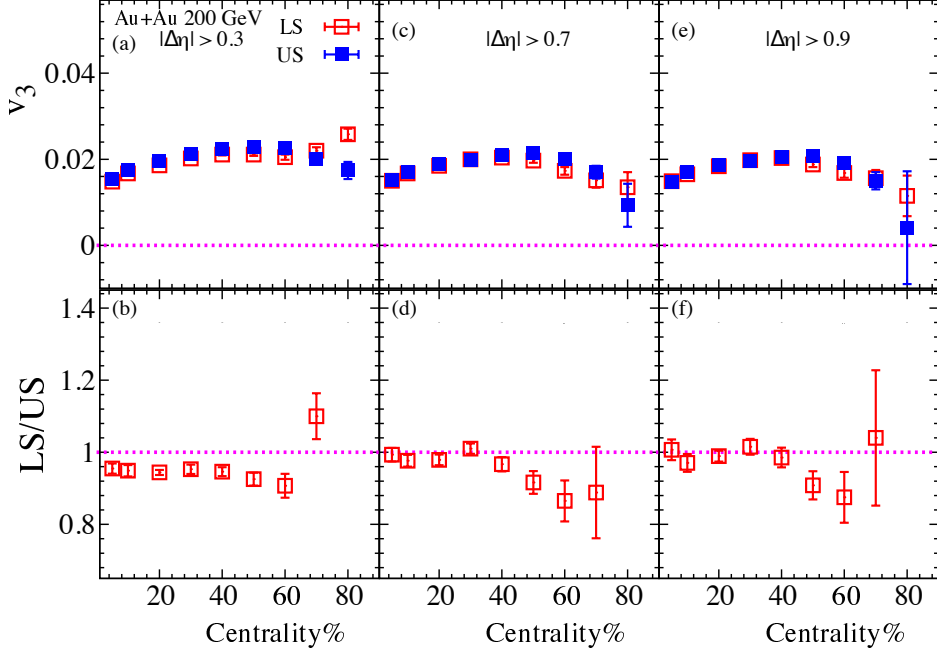


Fig. 3.5: Comparison of LS- and US- v_3 for Au+Au collisions at $\sqrt{s_{NN}} = 200$ GeV for $|\Delta\eta| > 0.3, 0.7$ and 0.9 respectively.

the LS- and US- v_n values. However, one can see a clear deterioration in the statistical significance of the measured v_n values, especially for the higher harmonics. Consequently, the cut $|\Delta\eta| > 0.7$, was employed to suppress short-range non-flow contributions for the data sets studied.

3.2.2 Supression of long-range non-flow (Global Momentum Conservation)

The conventional image of heavy-ion collisions is that a relatively thermalized fluid is formed which ultimately hadronizes into particles. Particles are emitted independently in each event, with an azimuthal distribution that fluctuates from one event to another. This leads to two-particle correlations which factorize into the product of two single-particle distributions [76] in

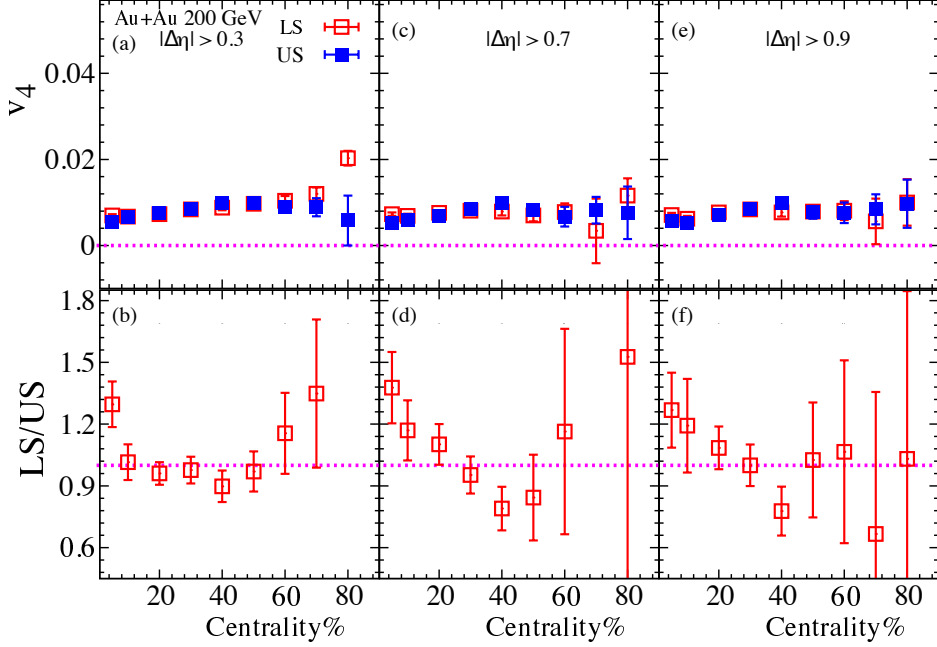


Fig. 3.6: Comparison of LS- and US- v_4 for Au+Au collisions at $\sqrt{s_{NN}} = 200$ GeV and $|\Delta\eta| > 0.3, 0.7$ and 0.9 respectively.

the absence of the short range non-flow effect:

$$v_{nn}(p_T^a, p_T^b) = v_n(p_T^a)v_n(p_T^b), \quad (3.23)$$

where the superscripts a and b are two different particles that can be selected from different bins in transverse momentum, and $v_n(p_T)$ is the anisotropic flow coefficient.

This factorization (Eq. 3.23) has been tested at the LHC for Pb+Pb collisions [77]. The tests were performed via fits to the left-hand side of Eq. 3.23, an $N \times N$ symmetric matrix for N bins in p_T , with the right-hand side of Eq. (3.23), using the N values of $v_n(p_T)$ as fit parameters. The ALICE collaboration showed that, while the data does factorize for $n > 1$, this factorization does not hold for $n = 1$ [77]. This is expected because the additional long-range correlation produced by momentum conservation largely affects the first harmonic [78].

As discussed in a later chapter, the first harmonic v_1 is comprised of

both a symmetric component v_1^{even} , and anti-symmetric component commonly termed sideways flow. The nature and the physics of the v_1^{even} will be discussed in the coming chapter. Here, I will present a representative example on how long-range non-flow is suppressed to enable reliable extraction of v_1^{even} .

In general, the constraint that all transverse momenta adds up to zero yields a back-to-back correlation between pairs, which grows linearly with the transverse momenta of both particles. This correlation adds to the correlation from flow as:

$$v_{11}(p_T^a, p_T^b) = v_1^{even}(p_T^a)v_1^{even}(p_T^b) - K p_T^a p_T^b. \quad (3.24)$$

Here, $K \propto 1/(\langle N_{ch} \rangle \langle p_T^2 \rangle)$ takes into account the non-flow correlations induced by global momentum conservation [74, 75]; $\langle N_{ch} \rangle$ is the mean multiplicity and $\langle p_T^2 \rangle$ is proportional to the variance of the transverse momentum over the full phase space. The charged particle multiplicity measured in the TPC acceptance is used as a proxy for $\langle N_{ch} \rangle$. For a given centrality selection, the left hand side of Eq. (3.24) represents a N-by-M v_{11} matrix (i.e., N values for p_T^b for each of the M p_T^a selections) which we fit with the right hand side using N + 1 parameters; N values of $v_1^{even}(p_T)$ and one additional parameter, K, which represent the momentum conservation effect [79].

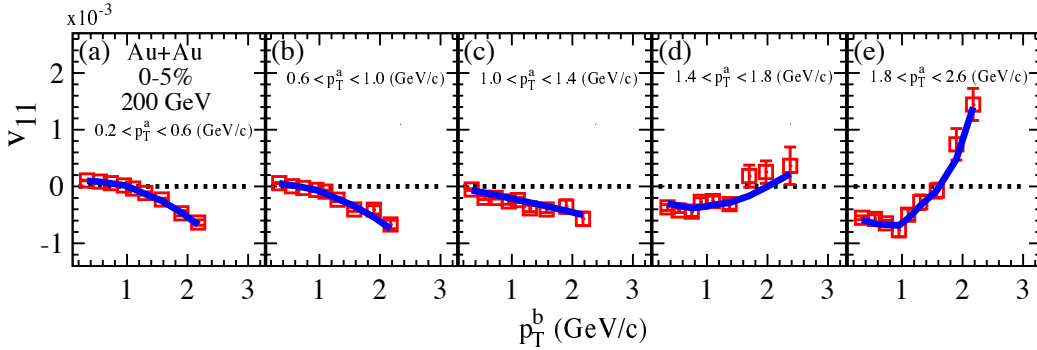


Fig. 3.7: v_{11} vs. p_T^b for several selections of p_T^a for 0-5% central Au+Au collisions at $\sqrt{s_{NN}} = 200$ GeV. The curve shows the result of the simultaneous fit with Eq. (3.24). The fit resulted in the value $\chi^2 = 1.1$ per degree of freedom.

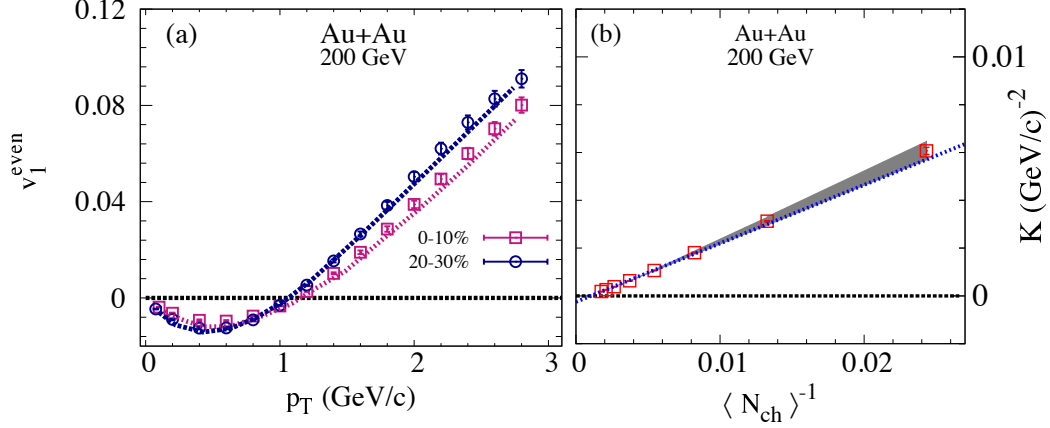


Fig. 3.8: The extracted values of v_1^{even} vs. p_T for Au+Au collisions at $\sqrt{s_{NN}} = 200$ GeV. (b) A representative set of the associated values of K vs. $\langle N_{ch} \rangle^{-1}$ from the same fits. The lines in panel (a) represent the result from a hydrodynamic calculations [74]. In panel (b) the associated momentum conservation coefficient, K vs. $\langle N_{ch} \rangle^{-1}$ is presented

Figure. 3.7 illustrates the efficacy of the fitting procedure for 0-5% central Au+Au collisions at $\sqrt{s_{NN}} = 200$ GeV. The solid curve (obtained with Eq. (3.24)) in each panel illustrates the effectiveness of the simultaneous fits, as well as the constraining power of the data. That is, $v_{11}(p_T^b)$ evolves from purely negative to negative and positive values as the selection range for p_T^a is increased.

The values of $v_1^{even}(p_T)$ extracted for different centrality selections are shown in Fig. 3.8(a). They indicate the characteristic pattern of a change from negative $v_1^{even}(p_T)$ at low p_T to positive $v_1^{even}(p_T)$ for $p_T > 1$ GeV/c. They also show the expected increase of v_1^{even} as collisions become more peripheral [74, 80]. Also, they show a good agreement with the hydrodynamic calculations [74]. Fig. 3.8(b) shows the results for the associated momentum conservation coefficients, K ; they indicate the expected linear dependence on $\langle N_{ch} \rangle^{-1}$. More details about the v_1^{even} will be discussed in the coming chapter.

3.3 Multi-Particle Correlation Technique

The multi-particle correlation technique or the cumulant technique [31–34] was also used in this work. The framework for the cumulant method is described in Refs. [32, 33], which was recently extended to the case of sub-event cumulants in Ref. [34, 81]. The cumulant technique requires a uniform detector acceptance. Therefore we will first discuss the procedure often used to account for non-uniform detector acceptance.

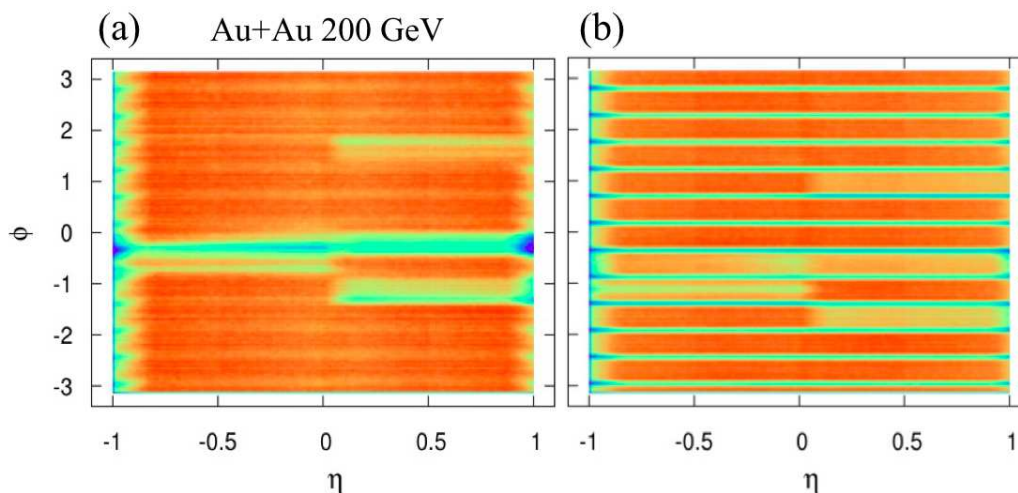


Fig. 3.9: The ϕ - η map for Au+Au $\sqrt{s_{NN}} = 200$ GeV before weighting for low (a) and high (b) p_T .

3.3.1 Correcting for detector acceptance

Since the event plane angle fluctuates randomly from event to event, the ϕ distribution of the emitted particles averaged over many events, should be flat. Deviations from this flat distribution would indicate detector acceptance effects as illustrated in Fig3.9. These effects can be corrected for using track-by-track weights (w_i). This weighting procedure involves first binning particles in ϕ - η maps and averaging over all events to obtain inverse weights which reflect deviations from a flat distribution. Since acceptance depends on particle charge, track curvature (related to p_T), Z-vertex, and centrality, separate ϕ - η maps were created for tracks with different event Z-vertex, event centrality, curvature, and charge. Subsequently, the weights

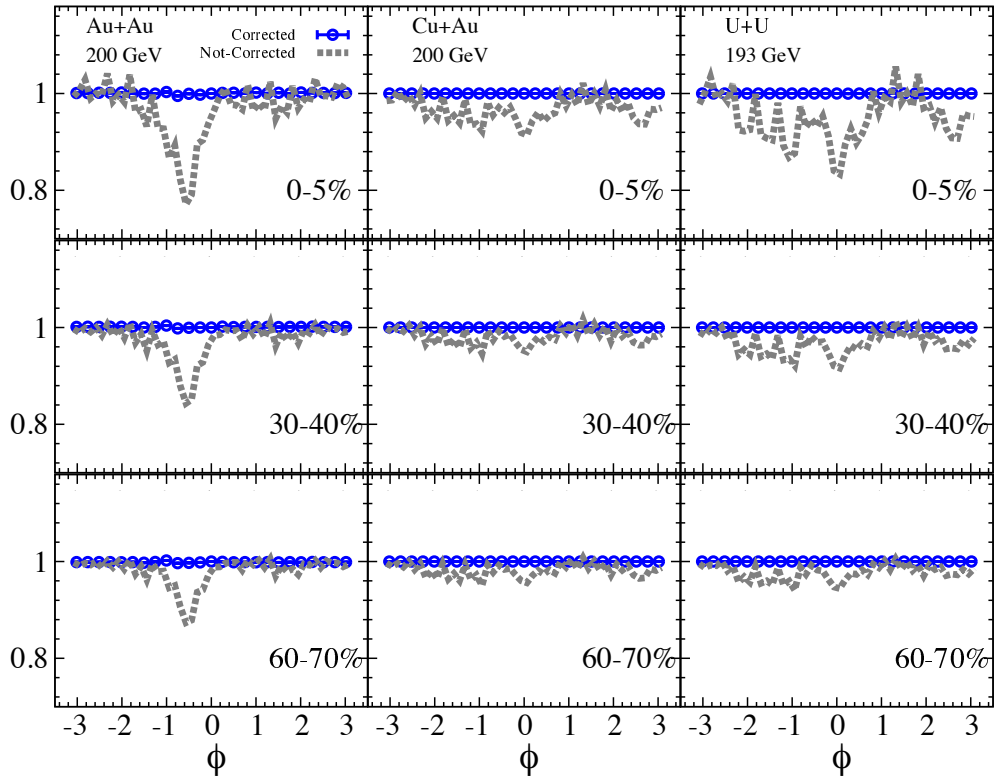


Fig. 3.10: The ϕ distribution for different collision systems before and after the acceptance correction.

were used to carry out acceptance corrections on the ϕ - η maps. After correction, we verified that for each ϕ - η map, the distribution of tracks was flat, as illustrated for several collision systems in Fig. 3.10.

3.3.2 Standard cumulant method

All of our differential and integrated four- and six-particle cumulants were constructed using the standard cumulant method with particle weights; in this method all quadruplets and pairs are selected using the entire TPC detector acceptance, $|\eta| < 1$.

The multi-particle correlations could be defined using the event-by-event

weighted Q vector evaluated for harmonic n as:

$$Q_{n,k} = \sum_{i=1}^M w_i^k e^{in\phi_i} \quad (3.25)$$

where w_i is the particle weight of the i 'th particle and M is the total number of Reference Particles (REP) in an event. For the REP we can also introduce the relation,

$$S_{p,k} = \left[\sum_{i=1}^M w_i^k \right]^p \quad (3.26)$$

Using Eqs. (3.25) and (3.26) we can write the two-particle correlations:

$$\langle 2 \rangle_n = \frac{|Q_{n,1}|^2 - S_{1,2}}{M_2}, \quad (3.27)$$

$$\langle \langle 2 \rangle \rangle_n = \frac{\sum_{i=1}^N (M_2 \langle 2 \rangle_n)_i}{\sum_{i=1}^N (M_2)_i}, \quad (3.28)$$

where N is the total number of events and M_2 is:

$$M_2 = S_{2,1} - S_{1,2} \quad (3.29)$$

$$\begin{aligned} \langle 4 \rangle_{n,m} = & \left[|Q_{n,1}|^2 |Q_{m,1}|^2 + |Q_{m+n,2}|^2 + |Q_{n-m,2}|^2 \right. \\ & - 2 \operatorname{Re} (Q_{m+n,2} Q_{n,1}^* Q_{m,1}^* - 2 Q_{n-m,2} Q_{m,1} Q_{n,1}^*) \\ & + 4 \operatorname{Re} (Q_{m,3} Q_{m,1}^* + Q_{n,3} Q_{n,1}^*) \\ & - S_{1,2} \operatorname{Re} (Q_{m,1} Q_{m,1}^* + Q_{n,1} Q_{n,1}^*) \\ & \left. + S_{2,2} - 6 S_{1,4} \right] / M_4, \end{aligned} \quad (3.30)$$

$$\langle \langle 4 \rangle \rangle_{n,m} = \frac{\sum_{i=1}^N (M_4 \langle 4 \rangle_{n,m})_i}{\sum_{i=1}^N (M_4)_i}, \quad (3.31)$$

where n and m are harmonic orders and M_4 is:

$$M_4 = S_{4,1} - 6S_{2,2}S_{2,1} + 8S_{1,3}S_{1,1} + 3S_{2,2} - 6S_{1,4} \quad (3.32)$$

The four-particle cumulant can be given as:

$$C_n\{4\} = \langle\langle 4 \rangle\rangle_{n,n} - 2 \langle\langle 2 \rangle\rangle_n \langle\langle 2 \rangle\rangle_n, \quad (3.33)$$

which leads to the four-particle flow harmonics:

$$v_n^4\{4\} = C_n\{4\}, \quad (3.34)$$

In similar fashion, the 6-particle cumulant can be written as:

$$\begin{aligned} \langle 6 \rangle_n &= (|Q_{n,1}|^6 - 6|Q_{n,1}|^2 \mathcal{R}e(Q_{2n,2} Q_{n,1}^* Q_{n,1}^*)) \\ &+ 9|Q_{2n,2}|^2 |Q_{n,1}|^2 + 4 \mathcal{R}e(Q_{3n,3} Q_{n,1}^* Q_{n,1}^* Q_{n,1}^*) \\ &+ 18S_{1,2} \mathcal{R}e(Q_{2n,2} Q_{n,1}^* Q_{n,1}^*) \\ &- 36 \mathcal{R}e(Q_{2n,4} Q_{n,1}^* Q_{n,1}^*) - 36 \mathcal{R}e(Q_{n,3} Q_{n,1} Q_{2n,2}^*) + 18S_{2,2} |Q_{n,1}|^2 \\ &- 54S_{1,4} |Q_{n,1}|^2 - 72S_{1,2} \mathcal{R}e(Q_{n,3} Q_{n,1}^*) + 36|Q_{n,3}|^2 \\ &+ 144 \mathcal{R}e(Q_{n,5} Q_{n,1}^*) - 9S_{1,2} |Q_{n,1}|^4 \\ &+ 36|Q_{n,1}|^2 \mathcal{R}e(Q_{n,3} Q_{n,1}^*) - 9S_{1,2} |Q_{2n,2}|^2 + 36 \mathcal{R}e(Q_{2n,4} Q_{2n,2}^*) \\ &- 12 \mathcal{R}e(Q_{3n,3} Q_{2n,2}^* Q_{n,1}^*) + 4|Q_{3n,3}|^2 \\ &+ 54S_{1,4}S_{1,2} - 6S_{3,2} - 120S_{1,6}) / (S_{6,1} - 15S_{1,2}S_{4,1} + 40S_{1,3}S_{3,1} + 45S_{2,2}S_{2,1} \\ &- 90S_{1,4}S_{2,1} - 120S_{1,3}S_{1,2}S_{1,1} - 15S_{3,2} \\ &+ 144S_{1,5}S_{1,1} + 90S_{1,4}S_{1,2} + 40S_{2,3} - 120S_{1,6}) \end{aligned} \quad (3.35)$$

$$\langle\langle 6 \rangle\rangle_n = \frac{\sum_{i=1}^N (M_6 \langle 6 \rangle_n)_i}{\sum_{i=1}^N (M_6)_i}, \quad (3.36)$$

where n is the harmonic order and M_6 is:

$$\begin{aligned} M_6 &= S_{6,1} - 15S_{1,2}S_{4,1} + 40S_{1,3}S_{3,1} + 45S_{2,2}S_{2,1} \\ &- 90S_{1,4}S_{2,1} - 120S_{1,3}S_{1,2}S_{1,1} - 15S_{3,2} \\ &+ 144S_{1,5}S_{1,1} + 90S_{1,4}S_{1,2} + 40S_{2,3} - 120S_{1,6}. \end{aligned} \quad (3.37)$$

Thus,

$$C_n\{6\} = \langle\langle 6 \rangle\rangle_n - 9 \langle\langle 4 \rangle\rangle_{n,n} \langle\langle 2 \rangle\rangle_n + 12 \langle\langle 2 \rangle\rangle_n^3 \quad (3.38)$$

and

$$v_n^6\{6\} = \frac{1}{4}C_n\{6\} \quad (3.39)$$

The two- and four-particle differential flow can also be obtained using a differential vector for the particle of interest (POI) as,

$$p_{n,k} = \sum_{i=1}^{m_p} w_i^k e^{in\phi_i}, \quad (3.40)$$

$$mp_{p,k} = \left[\sum_{i=1}^{m_p} w_i^k \right]^p. \quad (3.41)$$

For particles labeled as POI $w_i = 1$. For the subset labeled as both POI and REP we can introduce the expressions,

$$q_{n,k} = \sum_{i=1}^{m_q} w_i^k e^{in\phi_i}, \quad (3.42)$$

$$s_{p,k} = \left[\sum_{i=1}^{m_q} w_i^k \right]^p. \quad (3.43)$$

Thus, the weighted reduced 2- and 4-particle azimuthal correlations can be expressed as:

$$\langle 2^d \rangle_n = \frac{p_{n,0} Q_{n,1}^* - s_{1,1}}{M_2^d} \quad (3.44)$$

$$\langle \langle 2^d \rangle \rangle_n = \frac{\sum_{i=1}^N (M_2^d \langle 2^d \rangle_n)_i}{\sum_{i=1}^N (M_2^d)_i}, \quad (3.45)$$

$$M_2^d = mp_{1,1} s_{1,1} - s_{1,1} \quad (3.46)$$

$$\begin{aligned}
\langle 4^d \rangle &= \left[p_{n,0} Q_{n,1} Q_{n,1}^* Q_{n,1}^* \right. \\
&\quad - q_{2n,1} Q_{n,1}^* Q_{n,1}^* - p_{n,0} Q_{n,1} Q_{2n,2}^* \\
&\quad - 2 S_{1,2} p_{n,0} Q_{n,1}^* - 2 s_{1,1} |Q_{n,1}|^2 \\
&\quad + 7 q_{n,2} Q_{n,1}^* - Q_{n,1} q_{n,2}^* \\
&\quad + q_{2n,1} Q_{2n,2}^* + 2 p_{n,0} Q_{n,3}^* \\
&\quad \left. + 2 s_{1,1} S_{1,2} - 6 s_{1,3} \right] / M_4^d \tag{3.47}
\end{aligned}$$

$$\langle \langle 4^d \rangle \rangle = \frac{\sum_{i=1}^N (M_4^d \langle 4^d \rangle)_i}{\sum_{i=1}^N (M_4^d)_i}, \tag{3.48}$$

$$\begin{aligned}
M_4^d &= mp_{1,1} [S_{3,1} - 3 S_{1,1} S_{1,2} + 2 S_{1,3}] \\
&\quad - 3 [s_{1,1} (S_{2,1} - S_{1,2}) + 2 (s_{1,3} - s_{1,2} S_{1,1})]. \tag{3.49}
\end{aligned}$$

The four-particle differential cumulant can also be expressed as:

$$C_n^d\{4\} = \langle \langle 4^d \rangle \rangle_{n,n} - 2 \langle \langle 2^d \rangle \rangle_n \langle \langle 2 \rangle \rangle_n, \tag{3.50}$$

and the four-particle differential flow harmonics can be written as:

$$v_n^d\{4\} = \frac{C_n^d\{4\}}{(-C_n\{4\})^{3/4}} \tag{3.51}$$

3.3.3 The two-subevents cumulant method

A major advantage of the cumulant method is that it is designed to suppress non-flow contributions which originate from resonance decays, HBT, jet correlation and so on. In contrast to flow, this non-flow usually involves fewer particles. The multi-particle correlation method does not completely suppress such non-flow contributions [34]. For this reason, the sub-event cumulant method [34] was developed to further suppress the residual non-flow that the traditional method does not suppress.

In this method particles can be grouped into two different sub-events (A and B) in η . Each sub-event covers a non-overlapping η interval with

$|\Delta\eta| > 0.7$. Therefore the event-by-event weighted Q vector is evaluated for harmonic n as:

$$Q_{A,n,k} = \sum_{i=1}^M w_i^k(A) e^{in\phi_i^A}, \quad (3.52)$$

$$S_{A,p,k} = \left[\sum_{i=1}^M w_i^k(A) \right]^p, \quad (3.53)$$

$$Q_{B,n,k} = \sum_{i=1}^M w_i^k(B) e^{in\phi_i^B}, \quad (3.54)$$

$$S_{B,p,k} = \left[\sum_{i=1}^M w_i^k(B) \right]^p. \quad (3.55)$$

Accordingly the two-particle cumulant is expressed as:

$$\langle 2_{\text{Sub-2}} \rangle_n = \frac{Q_{A,n,1} Q_{B,n,1}^*}{S_{A,1,1} S_{B,1,1}}, \quad (3.56)$$

$$\langle \langle 2_{\text{Sub-2}} \rangle \rangle_n = \frac{\sum_{i=1}^N ((S_{A,1,1} S_{B,1,1}) \langle 2_{\text{Sub}} \rangle_n)_i}{\sum_{i=1}^N (S_{A,1,1} S_{B,1,1})_i}, \quad (3.57)$$

where N is the total number of events in a particular subevent class, and A and B represent two different subevents in η . The resulting two-particle cumulant and flow harmonics are:

$$C_n^{\text{Sub-2}}\{2\} = \langle \langle 2_{\text{Sub-2}} \rangle \rangle_n, \quad (3.58)$$

$$v_n\{2\} = \sqrt{C_n^{\text{Sub-2}}\{2\}}. \quad (3.59)$$

Similarly, the four-particle cumulant can be obtained as:

$$\begin{aligned} \langle 4_{\text{Sub-2}} \rangle_n &= |Q_{A,n,1}|^2 |Q_{B,n,1}|^2 \\ &- Q_{A,2n,2} Q_{B,n,1}^* Q_{B,n,1}^* \\ &- Q_{B,2n,2} Q_{A,n,1}^* Q_{A,n,1}^* \\ &- Q_{B,2n,2} Q_{A,2n,2}^* / (M_4^{\text{Sub}}). \end{aligned} \quad (3.60)$$

and

$$\langle\langle 4_{\text{Sub-2}} \rangle\rangle_n = \frac{\sum_{i=1}^N (M_4^{\text{Sub-2}} \langle 4_{\text{Sub-2}} \rangle_n)_i}{\sum_{i=1}^N (M_4^{\text{Sub-2}})_i}, \quad (3.61)$$

where n and m are harmonic orders and

$$M_4^{\text{Sub-2}} = (S_{A,2,1} - S_{A,1,2})(S_{B,2,1} - S_{B,1,2}). \quad (3.62)$$

The four-particle cumulant [34] is therefore given as:

$$C_n^{\text{Sub-2}}\{4\} = \langle\langle 4_{\text{Sub-2}} \rangle\rangle_n - 2 \langle\langle 2_{\text{Sub-2}} \rangle\rangle_n \langle\langle 2_{\text{Sub-2}} \rangle\rangle_n, \quad (3.63)$$

and the four-particle flow harmonics given as:

$$v_n^4\{4\} = C_n^{\text{Sub-2}}\{4\} \quad (3.64)$$

The two-particle differential flow harmonics can also be obtained via a differential vector for the particle of interest (POI) in sub-events B as:

$$\langle 2_{\text{Sub-2}}^d \rangle_n = \frac{Q_{n,1}^A P_{n,1}^B}{S_{1,1}^A m p_{1,1}^B}, \quad (3.65)$$

$$\langle\langle 2_{\text{Sub-2}}^d \rangle\rangle_n = \frac{\sum_{i=1}^N ((S_{1,1}^A m p_{1,1}^B) \langle 2_{\text{Sub-2}}^d \rangle_n)_i}{\sum_{i=1}^N (S_{1,1}^A m p_{1,1}^B)_i}, \quad (3.66)$$

to give the two-particle differential cumulants and flow harmonics as:

$$C_n^d\{2\} = \langle\langle 2_{\text{Sub-2}}^d \rangle\rangle_n, \quad (3.67)$$

$$v_n^d\{2\} = \frac{C_n^d\{2\}}{\sqrt{C_n\{2\}}}. \quad (3.68)$$

3.3.4 The three sub-events cumulant method

As stated before, multi-particle correlations [34] can suppress the non-flow contributions to the correlations. However, for jets multiple particles can be correlated, which renders the standard cumulant ineffective for suppression of such non-flow contributions. The three sub-events cumulant method was

introduced to suppress this non-flow contribution especially for collisions in which jet production is significant.

In this method [34], particles are grouped into three different sub-events (A, B and C) in η , with non-overlapping η intervals. In each event, particles are then selected from these sub-events to form correlated multiplets. The introduction of this additional sub-event serves to further reduce the short-range (in η) non-flow correlations usually associated with jets. An additional benefit is that the three sub-events method is also able to reduce the effects of long-range non-flow correlations, i.e. back-to-back di-jet correlations. This is primarily because the particles from the two correlated jets (near- and away-side jets) can only fall into two out of the three sub-events. Thus there will always be at least one particle in the four-particle correlation that is not associated with the di-jet. After averaging all the combinations, the di-jet correlation is significantly suppressed [34]. The di-jet contribution can be further reduced via a small η gaps between the three subevents if the statistical significance of the data allow these additional cuts [34].

For this method, the event-by-event weighted Q vector is evaluated for harmonic n as:

$$Q_{A,n,k} = \sum_{i=1}^M w_i^k(A) e^{in\phi_i^A}, \quad (3.69)$$

$$S_{A,p,k} = \left[\sum_{i=1}^M w_i^k(A) \right]^p, \quad (3.70)$$

$$Q_{B,n,k} = \sum_{i=1}^M w_i^k(B) e^{in\phi_i^B}, \quad (3.71)$$

$$S_{B,p,k} = \left[\sum_{i=1}^M w_i^k(B) \right]^p. \quad (3.72)$$

$$Q_{C,n,k} = \sum_{i=1}^M w_i^k(C) e^{in\phi_i^C}, \quad (3.73)$$

$$S_{C,p,k} = \left[\sum_{i=1}^M w_i^k(C) \right]^p. \quad (3.74)$$

Due to symmetry, there are six ways to construct the 4-particle correlations:

$$\begin{aligned}
\langle 4^{Sub-3} \rangle &= e^{\phi_A + \phi_A^* - \phi_B - \phi_C}, \\
&= e^{\phi_B + \phi_B^* - \phi_A - \phi_C}, \\
&= e^{\phi_C + \phi_C^* - \phi_A - \phi_B}, \\
&= e^{\phi_A + \phi_B - \phi_A^* - \phi_C}, \\
&= e^{\phi_B + \phi_C - \phi_B^* - \phi_A}, \\
&= e^{\phi_C + \phi_A - \phi_C^* - \phi_B},
\end{aligned} \tag{3.75}$$

where ϕ_X^* belong to the same sub-event X but different from ϕ_X . Further details can be found in Ref.[34].

We will focus only on the first one $e^{\phi_A + \phi_A^* - \phi_B - \phi_C}$, which leads to:

$$\begin{aligned}
\langle 4^{Sub-3} \rangle &= (Re(Q_{A,n,1} Q_{b,n,1}^* Q_{A,n,1} Q_{C,n,1}^* \\
&\quad - Re(Q_{A,2n,2} Q_{B,n,1}^* Q_{C,n,1}^*))/M_4^{Sub-3}.
\end{aligned} \tag{3.76}$$

Then,

$$\langle \langle 4_{Sub-3} \rangle \rangle_n = \frac{\sum_{i=1}^N (M_4^{Sub-3} \langle 4_{Sub-3} \rangle_n)_i}{\sum_{i=1}^N (M_4^{Sub-3})_i}, \tag{3.77}$$

where n and m are harmonic orders and M_4 is:

$$M_4^{Sub-3} = (S_{A,2,1} - S_{A,1,2})(S_{B,1,1} S_{C,1,1}) \tag{3.78}$$

This gives the four-particle cumulants as:

$$C_n^{Sub-3}\{4\} = \langle \langle 4_{Sub-3} \rangle \rangle_n - 2 \langle \langle 2_{Sub-2} \rangle \rangle_n^{AB} \langle \langle 2_{Sub-2} \rangle \rangle_n^{AC}, \tag{3.79}$$

and the four-particle flow harmonics as:

$$v_n^4\{4\} = C_n^{Sub-3}\{4\} \tag{3.80}$$

3.3.5 Flow fluctuations effects

In addition to non-flow, fluctuations also impact v_n experimental measurements. When the heavy-ion collision starts, the nucleon distributions in the overlap region fluctuates event-by-event. These initial geometry fluctuations will drive flow fluctuations in the final state. As discussed earlier

the $2m$ -particle azimuthal correlator is obtained by averaging over all unique combinations in one event then overall events [32, 82]:

$$\langle 2m \rangle = \langle e^{in \sum_{j=1}^m (\phi_{2j-1} - \phi_{2j})} \rangle \quad (3.81)$$

where the mean $\langle \dots \rangle$ is taken within a single event. Assuming that the non-flow contributions are negligible, we can write:

$$\begin{aligned} v_n\{2\}^2 &= \langle \langle 2 \rangle \rangle, \\ v_n\{4\}^4 &= 2\langle \langle 2 \rangle \rangle - \langle \langle 4 \rangle \rangle. \end{aligned} \quad (3.82)$$

Therefore we can relate the ratio $v_n\{4\}/v_n\{2\}$ to the variance of v_n^2 , $\sigma^2(v_n^2) \equiv \langle v_n^4 \rangle - \langle v_n^2 \rangle^2$

$$\begin{aligned} \left(\frac{v_n\{4\}}{v_n\{2\}} \right)^4 &= 2 - \frac{\langle v_n^4 \rangle}{\langle v_n^2 \rangle^2}, \\ \left(\frac{v_n\{4\}}{v_n\{2\}} \right)^4 &= 1 - \frac{\sigma^2(v_n^2)}{\langle v_n^2 \rangle^2}. \end{aligned} \quad (3.83)$$

Therefore, the ratio $v_n\{4\}/v_n\{2\}$ can be used to estimate the strength of the flow fluctuations as a fraction of the measured flow harmonic. Here, a large value of $v_n\{4\}/v_n\{2\}$ indicates less fluctuations whereas a smaller value indicate large fluctuations.

Chapter 4

Beam Energy and Collision System Dependence of Flow Harmonics

Anisotropic flow is derived from an eccentricity-driven hydrodynamic expansion of the plasma created in the collision zone [83–88] produced by the colliding ions. That is, the eccentricity ϵ_n , drives unequal pressure gradients in- and out of the event plane Ψ_n , leading to an anisotropic expansion that results in the anisotropic emission of particles about this plane. Thus, anisotropic flow measurements are sensitive to the initial-state eccentricity, the equation of state (EOS) and the transport properties of the medium. Accordingly, such measurements are at the forefront of ongoing efforts to extract the T and μ_B dependence of the transport coefficient η/s , as well as to constrain the initial-state eccentricity spectrum.

In this chapter, the differential and p_T -integrated flow harmonics for the systems studied are presented and discussed.

4.1 Beam Energy Dependence of v_n

The v_n measurements from the RHIC BES can aid the study of η/s for the broad range of μ_B and T , produced in these collisions [89]. Currently, there is little, if any, experimental constraints for the μ_B and T dependence of η/s , especially for the lower beam energies i.e, low T and large μ_B .

Theory suggests that η/s depends on both μ_B and T , and could have a

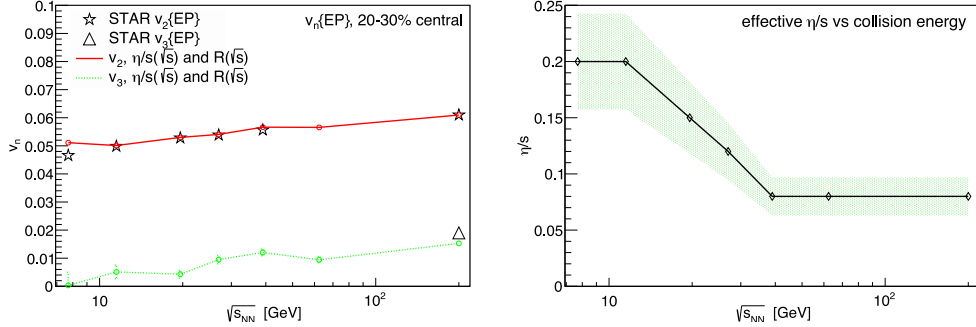


Fig. 4.1: The left panel shows the p_T integrated v_2 and v_3 coefficients vs. $\sqrt{s_{NN}}$. The lines represent the results obtained using $\sqrt{s_{NN}}$ dependent η/s . The experimental data is from the STAR collaboration [90]. The right panel shows the effective values of η/s used to describe the experimental data at different collision energies. The green-band represents the estimated uncertainty. Both panels are taken from Ref. [89].

minimum in the vicinity of the critical point [91]. A recent study involving the theoretical calculation of v_2 for different values of η/s at each beam energy [89], indicate agreement with the data (Fig.4.1) only for an increase in η/s as the beam energy is lowered. For these calculations η/s was assumed to be constant during the evolution of the fireball at each collision energy. Since smaller values of $\sqrt{s_{NN}}$ result in larger values of μ_B and lower temperatures, Fig.4.1 suggests that η/s could have a dependence on both μ_B and T . The new BES v_n measurements presented in the following are expected to provide better constraints for theoretical models and hence, lead to a better characterization of $\frac{\eta}{s}(\mu_B, T)$.

4.1.1 Flow harmonics measurements for $v_{n>1}$

A representative set of results for differential and integrated $v_{n \geq 2}$ for Au+Au collisions at $\sqrt{s_{NN}} = 7.7-200$ GeV is summarized in Figs. 4.2, 4.3, 4.4, and 4.5. Fig. 4.2 shows the η dependence of v_n for the centrality selection 0-40%, for $\sqrt{s_{NN}} = 7.7-200$ GeV. It indicates a sizable dependence of the magnitude of v_n on the harmonic number, n , with similar trends for each beam energy. By contrast, the figure shows a weak dependence of v_n on η over the full range of beam energies. These respective dependencies can

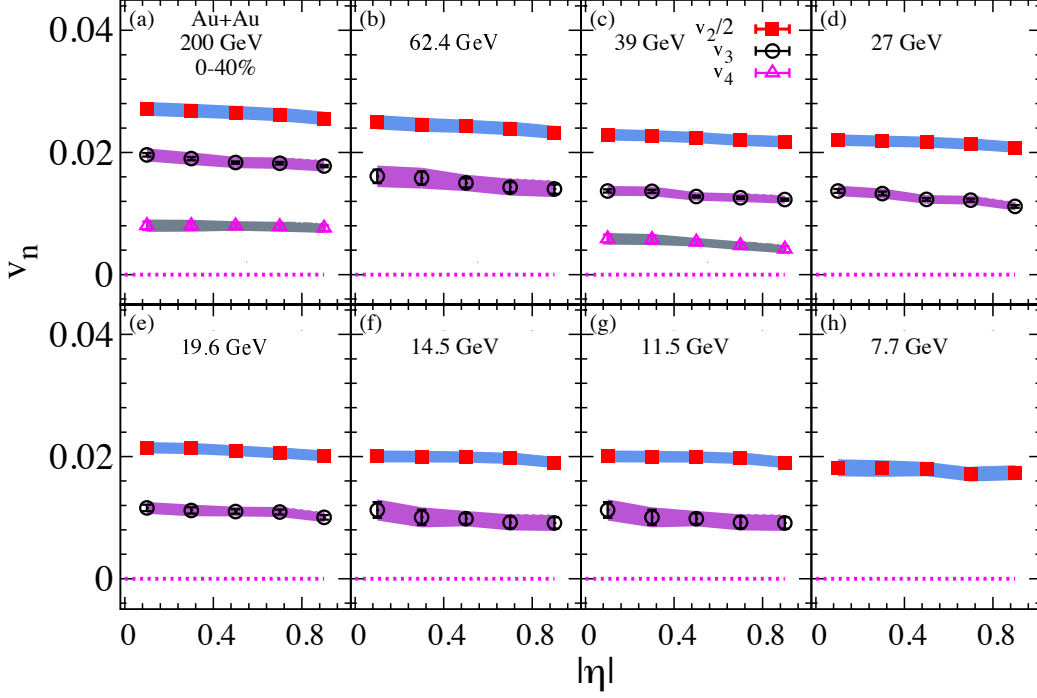


Fig. 4.2: The $v_{n \geq 2}$ as a function of $|\eta|$ for charged particles with $0.2 < p_T < 4$ GeV/c in 0-40% central Au+Au collisions at $\sqrt{s_{NN}} = 7.7$ -200 GeV. The shaded bands represent the systematic uncertainty.

serve as important constraints for theoretical models.

The p_T -differential measurements are shown in Fig 4.3 for the centrality selection 0-40%, for Au+Au at $\sqrt{s_{NN}} = 7.7$ -200 GeV. They indicate sizable dependencies on p_T and the harmonic number, with similar trends for each beam energy. These data also indicate a weak dependence on $\sqrt{s_{NN}}$.

The centrality dependence of v_n is shown in Fig. 4.4 for a similar beam energy range for Au+Au collisions. The figure shows a weak centrality dependence for the higher harmonics, which all decrease with decreasing values of $\sqrt{s_{NN}}$. These patterns may be related to the detailed dependence of the viscous effects in the created medium, which serve to attenuate the magnitude of v_n .

Figure 4.5 shows the excitation functions for the p_T -integrated $v_{2,3,4}$ for 0 – 40% central Au+Au collisions. An essentially monotonic trend for v_2 , v_3 and v_4 with $\sqrt{s_{NN}}$ can be observed, as might be expected for a temperature

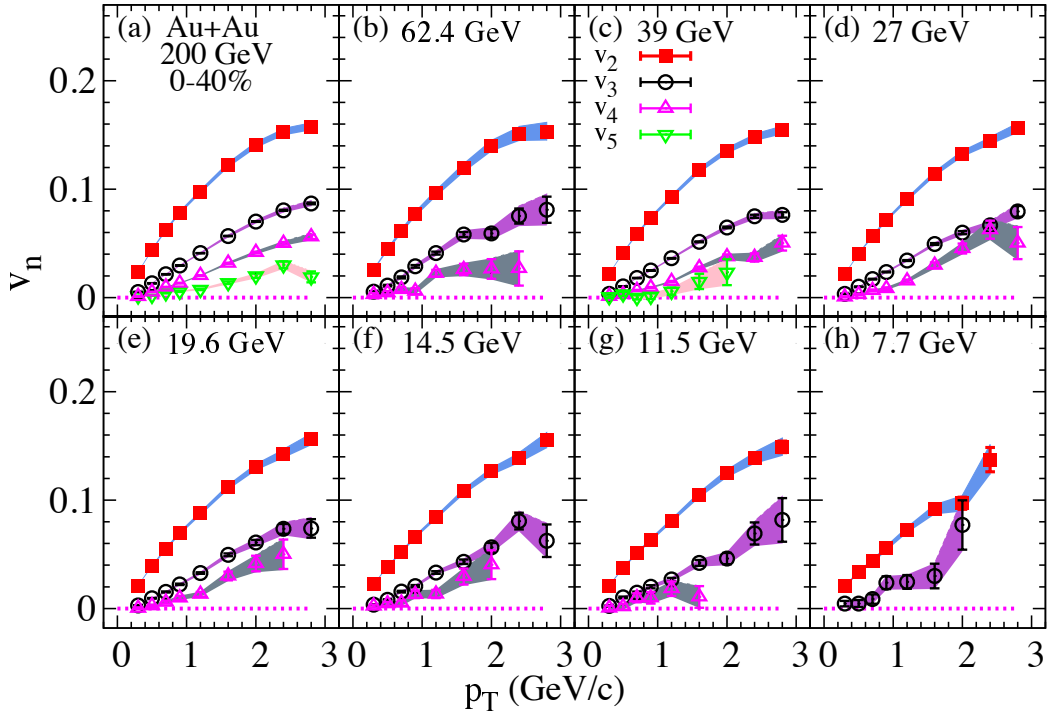


Fig. 4.3: The $v_{n \geq 2}$ as a function of p_T for charged particles in 0-40% central Au+Au collisions at $\sqrt{s_{NN}} = 7.7\text{-}200$ GeV. The shaded bands represent the systematic uncertainty.

increase with $\sqrt{s_{NN}}$.

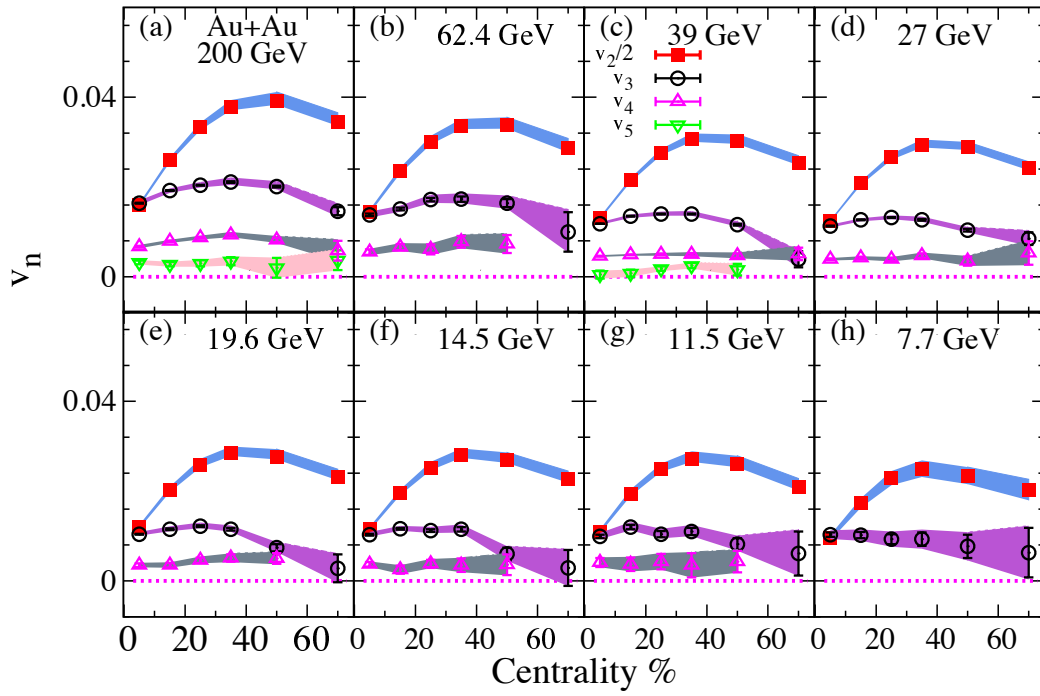


Fig. 4.4: The integrated $v_n(\text{Centrality}\%)$ as a function of Au+Au collision centrality for charged particles with $0.2 < p_T < 4$ GeV/c. The shaded bands represent the systematic uncertainty.

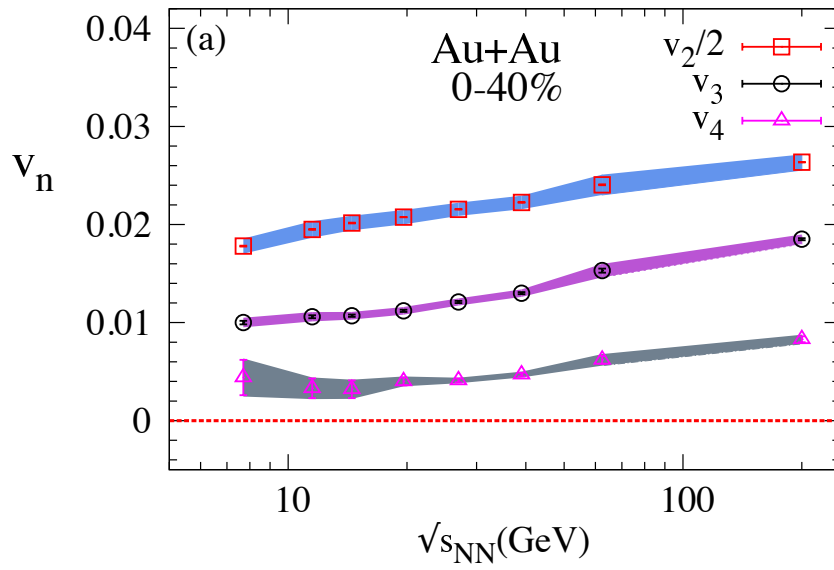


Fig. 4.5: The integrated $v_n(\sqrt{s_{NN}})$ for charged particles with $0.2 < p_T < 4$ GeV/c for 0-40% central Au+Au collisions. The shaded bands represent the systematic uncertainty.

4.1.2 The rapidity-even dipolar flow v_1^{even}

In the absence of fluctuations, the directed flow v_1 develops along the direction of the impact parameter [92] which is an odd function, $v_1^{odd}(\eta) = -v_1^{odd}(-\eta)$, of pseudorapidity. However, initial-state fluctuations, acting in concert with hydrodynamic-like expansion, gives an additional rapidity-even, $v_1^{even}(\eta) = v_1^{even}(-\eta)$, component [73, 80] resulting in the total:

$$v_1(\eta) = v_1^{even}(\eta) + v_1^{odd}(\eta). \quad (4.1)$$

The magnitude of $v_1^{odd}(\eta)$ can be made negligible via a symmetric pseudorapidity selection, to give a straightforward measurement of $v_1^{even}(\eta)$.

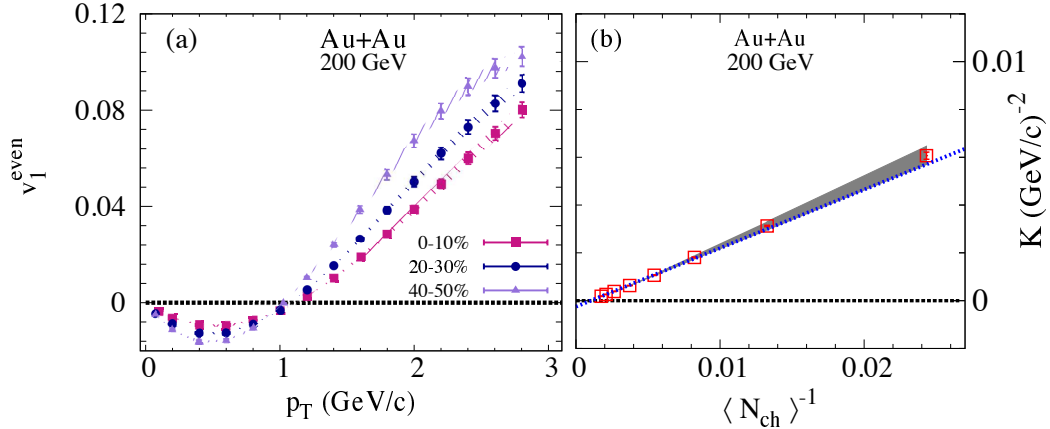


Fig. 4.6: (a) The extracted values of v_1^{even} vs. p_T for Au+Au collisions at $\sqrt{s_{NN}} = 200$ GeV. (b) A representative set of the associated values of K vs. $\langle N_{ch} \rangle^{-1}$ from the same fits. The shaded bands represent the systematic uncertainty.

The rapidity-even v_1 is proportional to the fluctuations-driven dipole asymmetry ε_1 of the system [73, 80, 93]; $v_1^{even} \propto \varepsilon_1$, where $\varepsilon_1 \equiv \langle |r^3 e^{i\phi}| \rangle / \langle r^3 \rangle$ and averaging is taken over the initial energy density after re-centering the coordinate system, i.e., $\langle |r e^{i\phi}| \rangle = 0$. Hydrodynamical model calculations [74] indicate that the magnitude of v_1^{even} is sensitive to η/s , albeit with less sensitivity than for the higher order harmonics, $n \geq 2$. It has not been experimentally established whether this sensitivity depends on the temperature T , baryon chemical potential μ_B or both. Similarly it has not been established whether this sensitivity could reflect the influence of a possible critical

end point (CEP) in the phase diagram for nuclear matter [94]. Therefore, differential v_1^{even} measurements that span a broad range of $\sqrt{s_{\text{NN}}}$ (T and μ_B), could potentially provide (i) unique supplemental constraints to discern between different initial-state models, (ii) aid precision extraction of η/s and study its possible dependence on T and μ_B , and (iii) give insight on the CEP.

As stated in section 3.2.2, for a given centrality selection, the left hand side of Eq. (3.24) represents a N -by- M v_{11} matrix which we fit with the right hand side using $N + 1$ parameters; N values of $v_1^{\text{even}}(p_T)$ and one additional parameter, K , which represent the momentum conservation effect [79, 95]. The extracted values of $v_1^{\text{even}}(p_T)$ for different centrality selections (0-10%, 20-30% and 40-50%) are shown in Fig. 4.6(a). They indicate the characteristic pattern of a change from negative $v_1^{\text{even}}(p_T)$ at low p_T to positive $v_1^{\text{even}}(p_T)$ for $p_T > 1$ GeV/c. They also show the expected increase of v_1^{even} as collisions become more peripheral, in line with the expected centrality dependence of the dipole asymmetry ε_1 , where $\varepsilon_1 \equiv |(r^3 e^{i\phi})|/r^3$ [80, 96]. Fig. 4.6(b) shows the results for the associated momentum conservation coefficients, K ; they indicate the expected linear dependence on $\langle N_{ch} \rangle^{-1}$.

The resulting extracted values of $v_1^{\text{even}}(p_T)$ for 0-10% central Au+Au collisions are shown for the full span of BES-I energies in Fig. 4.7. These values indicate the characteristic pattern of a change from negative $v_1^{\text{even}}(p_T)$ at low p_T , to positive $v_1^{\text{even}}(p_T)$ for $p_T \gtrsim 1$ GeV/c, with a crossing point that only very slowly shifts with $\sqrt{s_{\text{NN}}}$. This predicted pattern for rapidity-even dipolar flow [73, 80] is also indicated by the solid line in panel (a), which shows the result of a hydrodynamic model calculation [74]. It stems from the requirement that the net transverse momentum of the system is zero, i.e., $\langle p_T v_1^{\text{even}}(p_T) \rangle = 0$, which implies that the hydrodynamic flow direction of low- p_T particles is opposite to those for high- p_T particles Fig. 4.8. Crosschecks made with a large sample of the data, confirmed that $\langle p_T v_1^{\text{even}}(p_T) \rangle \sim 0$, within systematic uncertainties. The crossing point is also expected to shift with $\sqrt{s_{\text{NN}}}$ since the $\langle p_T \rangle$ and $\langle p_T^2 \rangle$ values change with $\sqrt{s_{\text{NN}}}$ [79, 95]. For these data, there is little, if any, shift due to the weak dependence of the $\langle p_T \rangle$ on $\sqrt{s_{\text{NN}}}$ for the indicated centrality selection. It is noteworthy that the low statistical significance of the data for $\sqrt{s_{\text{NN}}} < 19.6$ GeV, precluded similar centrality dependent plots for these beam energies.

The centrality dependencies of the p_T -weighted $|v_1^{\text{even}}|$ and K are shown in Figs. 4.9 and 4.10 for several $\sqrt{s_{\text{NN}}}$ values as indicated, and for $0.4 < p_T < 0.7$ GeV/c; this p_T range was selected to minimize the associated statistical uncertainties and a possible influence from a change in the crossing point

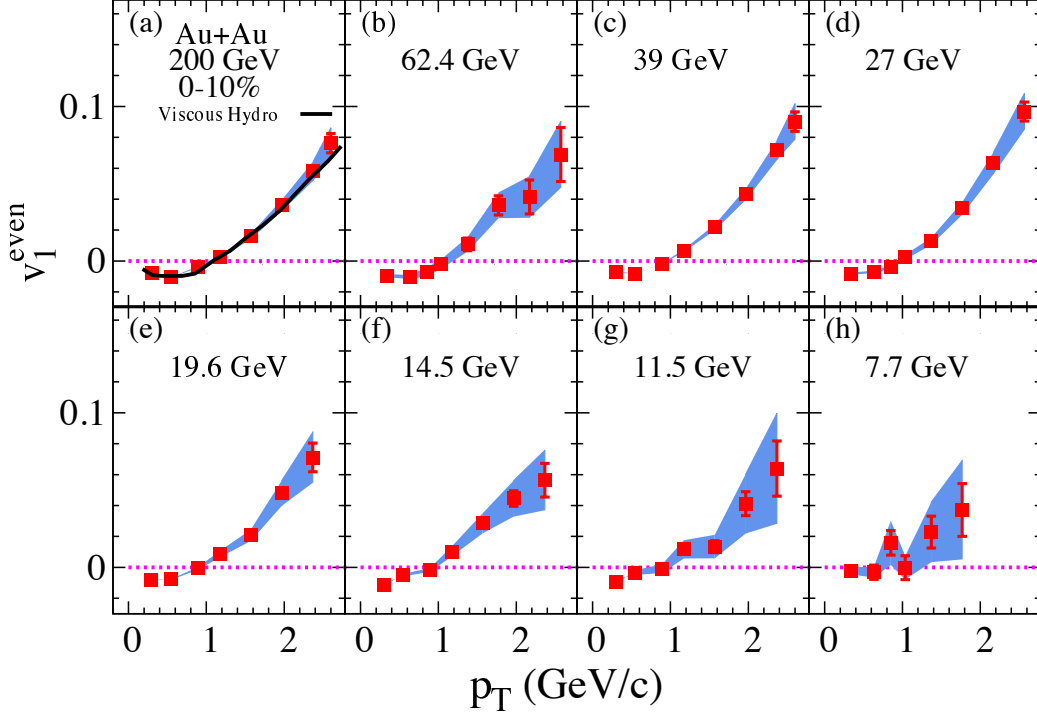


Fig. 4.7: Extracted values of v_1^{even} vs. p_T for 0-10% central Au+Au collisions for several values of $\sqrt{s_{\text{NN}}}$ as indicated. The curve in panel (a) shows the result from a viscous hydrodynamically based predictions [74]. The shaded bands indicate the systematic uncertainties.

with $\sqrt{s_{\text{NN}}}$. For each value of $\sqrt{s_{\text{NN}}}$, Fig. 4.10 indicates a linear dependence of K on $\langle N_{\text{ch}} \rangle^{-1}$ with slopes that decrease with increasing $\sqrt{s_{\text{NN}}}$. This is to be expected since $K \propto 1/(\langle N_{\text{ch}} \rangle \langle p_T^2 \rangle)$ and the values for $\langle p_T^2 \rangle$ increase with $\sqrt{s_{\text{NN}}}$ for most of the centrality range. The increase in the magnitude of $|v_1^{\text{even}}|$ as collisions become more peripheral (Fig. 4.9), is expected since v_1^{even} is driven by fluctuations which become more important for smaller systems, i.e., for more peripheral collisions.

Figure 4.9 also hints at both a sizable decrease in the magnitude of $|v_1^{\text{even}}|$ and a possible weakening of its centrality dependence, as the beam energy is reduced. These patterns and the ones shown in Fig. 4.7 cannot be explained solely by the small change in the Glauber model eccentricity values at a given centrality which result from a change in the beam energy. Thus, they provide a new set of supplemental constraints for the extraction of $\frac{\eta}{s}(T)$.

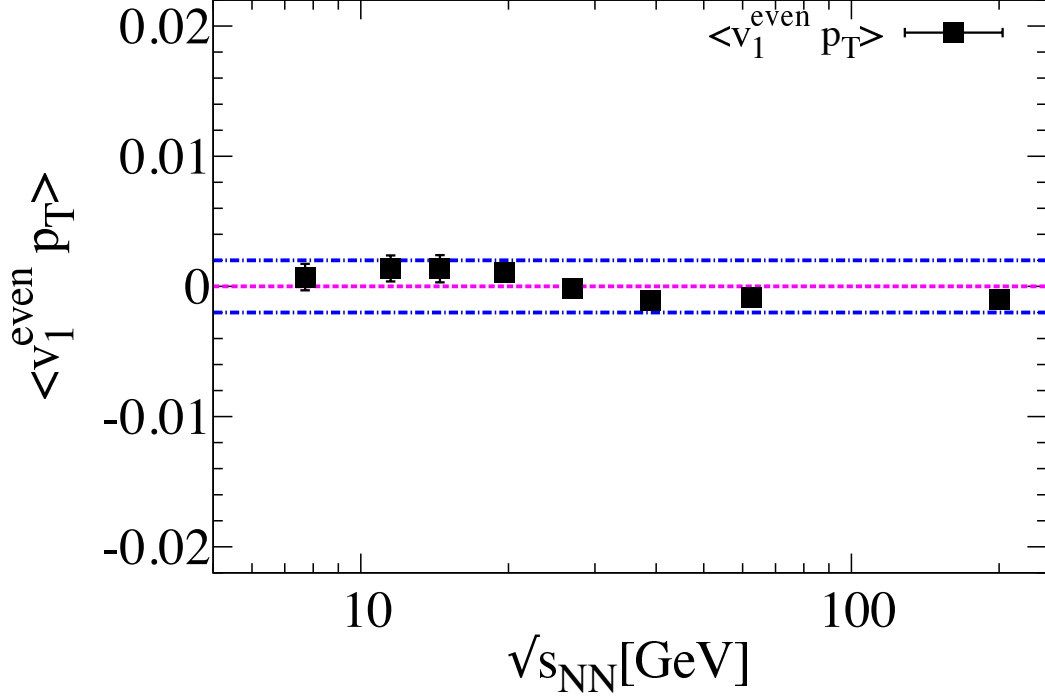


Fig. 4.8: Extracted values of $\langle p_T v_1^{\text{even}}(p_T) \rangle$ vs. $\sqrt{s_{\text{NN}}}$ for 0-10% central Au+Au collisions.

The constraining power of v_1^{even} is further illustrated in Fig. 4.11 where a comparison of the excitation functions for v_1^{even} and v_3 is shown for $0.4 < p_T < 0.7$ GeV/c; the v_1^{even} data are reflected about zero to facilitate a comparison of the magnitudes. The v_3 data, which are obtained from the present analysis, are in good agreement with the data reported in Ref. [97] for the same centrality and p_T cuts. The comparison indicates strikingly similar magnitudes and trends for $|v_1^{\text{even}}|$ and v_3 , suggesting a much larger viscous attenuation of v_3 . Note that while ε_1 and ε_3 are both fluctuation-driven, $\varepsilon_3 \sim 2\varepsilon_1$ for 0-10% central Au+Au collisions [80, 96] over the $\sqrt{s_{\text{NN}}}$ range of interest. A similar pattern was observed for comparisons made at higher p_T , albeit with lower statistical significance. These excitation functions are expected to provide important experimental input to ongoing theoretical attempts to pin down initial state models and make precision extractions of the specific shear viscosity.

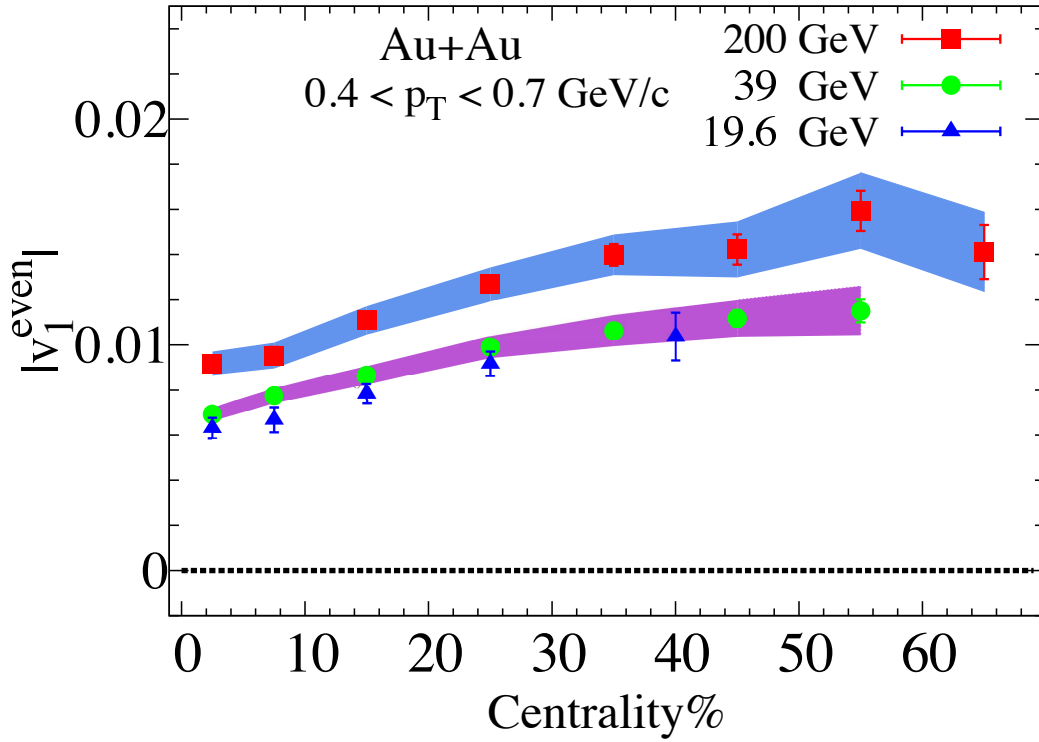


Fig. 4.9: Centrality dependence of v_1^{even} for $0.4 < p_T < 0.7 \text{ GeV}/c$ for Au+Au collisions at $\sqrt{s_{\text{NN}}} = 200, 39, \text{ and } 19.6 \text{ GeV}$. The shaded bands represent the systematic uncertainties.

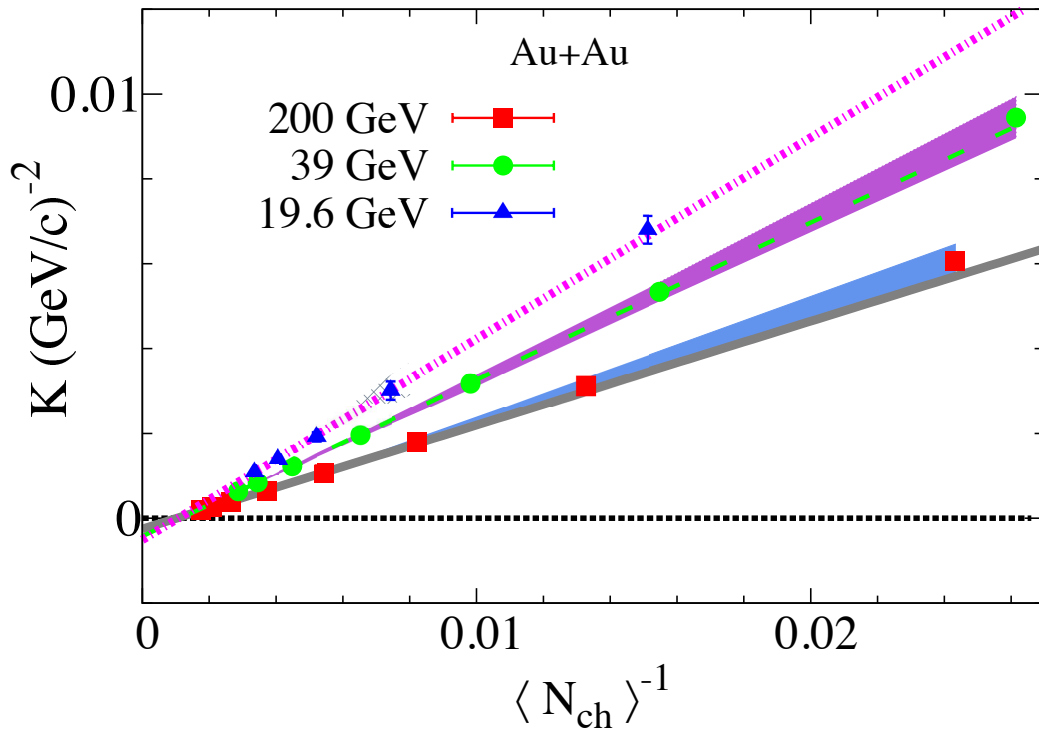


Fig. 4.10: The extracted K vs. $\langle N_{\text{ch}} \rangle^{-1}$ for the v_1^{even} values shown in Fig. 4.9. The indicated lines show linear fits to the data; the shaded bands represent the systematic uncertainties.

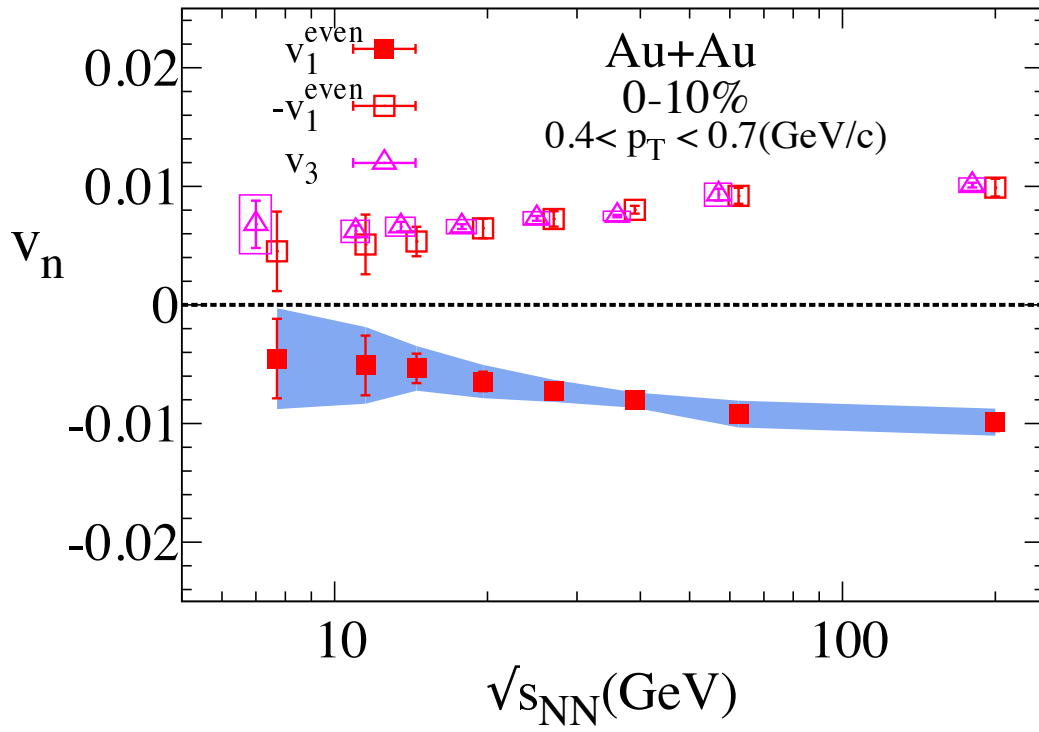


Fig. 4.11: Comparison of the $\sqrt{s_{NN}}$ dependence of v_1^{even} and v_3 for $0.4 < p_T < 0.7$ GeV/c in 0-10% central Au+Au collisions. The v_1^{even} results are reflected about zero (and shifted horizontally) to facilitate a comparison of the magnitudes. The shaded bands indicate the systematic uncertainties.

4.2 Collision System Dependence of v_n

Recent measurements at both the RHIC and the Large Hadron Collider (LHC), have indicated sizable v_2 and v_3 values in high multiplicity p+p [98, 99], d+Au [100, 101] and p+Pb collisions [102–104], reminiscent of those observed in peripheral A+A collisions. These measurements have generated considerable debate on whether the final-state collective effects, which dominate the mechanism for anisotropic flow in A+A collisions also drive the anisotropy measured in high-multiplicity p+p and p+A (d+A) collisions [105–107]. The related question of whether the properties of the medium produced in the small p+p, p+A and d+A systems are similar to those produced in the larger A+A systems is also not fully settled.

Before going any farther in this discussion more insight about the anisotropic flow contribution to the measured anisotropy for U+U collisions at $\sqrt{s_{\text{NN}}} = 193$ GeV, Au+Au, Cu+Cu, Cu+Au, and d+Au collisions at $\sqrt{s_{\text{NN}}} = 200$ GeV could be revealed via studying the two-particle $\Delta\phi$ correlation functions (C_r) with $|\Delta\eta| > 0.7$. Also further checks for the dominance of flow correlations in the studied systems was obtained by measuring the second-order four-particle cumulant $c_2\{4\}$ [31–34]:

$$c_2\{4\} = \langle\langle 4 \rangle\rangle - 2\langle\langle 2 \rangle\rangle^2, \quad (4.2)$$

where $\langle\langle \rangle\rangle$ represents the averaging first over particles in an event and then over all events within a given event class. The three sub-event method [34] was used for these evaluations with sub-events for $\eta_1 < -0.35$, $|\eta_2| < 0.35$ and $\eta_3 > 0.35$.

Figures 4.12, 4.13 and 4.14 show the correlation functions obtained for U+U, Au+Au, Cu+Au, Cu+Cu, and d+Au collisions for different $\langle N_{\text{ch}} \rangle$ value. They indicate patently similar correlation patterns with a visible enhancement of near-side ($\Delta\phi \sim 0$) pairs, reminiscent of the so-called "ridge" observed in high multiplicity p+p [98, 99], d+Au [100, 101] and p+Pb collisions [102, 104].

The extracted values for $c_2\{4\}$ vs. $\langle N_{\text{ch}} \rangle$, using the three-subevent method shown in Fig. 4.15, indicate negative values which confirm the absence of significant non-flow contributions, and the dominance of flow correlations to C_r [82].

In this section we present and compare a comprehensive set of v_1^{even} , v_2 and v_3 measurements for U+U ($\sqrt{s_{\text{NN}}} = 193$ GeV), Au+Au, Cu+Cu,

Cu+Au, and d+Au collisions at $\sqrt{s_{\text{NN}}} = 200$ GeV, which should prove invaluable in ongoing efforts to constrain theoretical models and obtain a robust extraction of $\frac{v_2}{s}(T)$. In turn, we also use these measurements to perform scaling tests within the acoustic model framework [108–110] which give insight on (i) the anisotropic flow contribution to the measured anisotropy for each system, and (ii) the relative influence of final-state viscous attenuation in the medium created in A+A, and d+A collisions at comparable $\langle N_{\text{ch}} \rangle$.

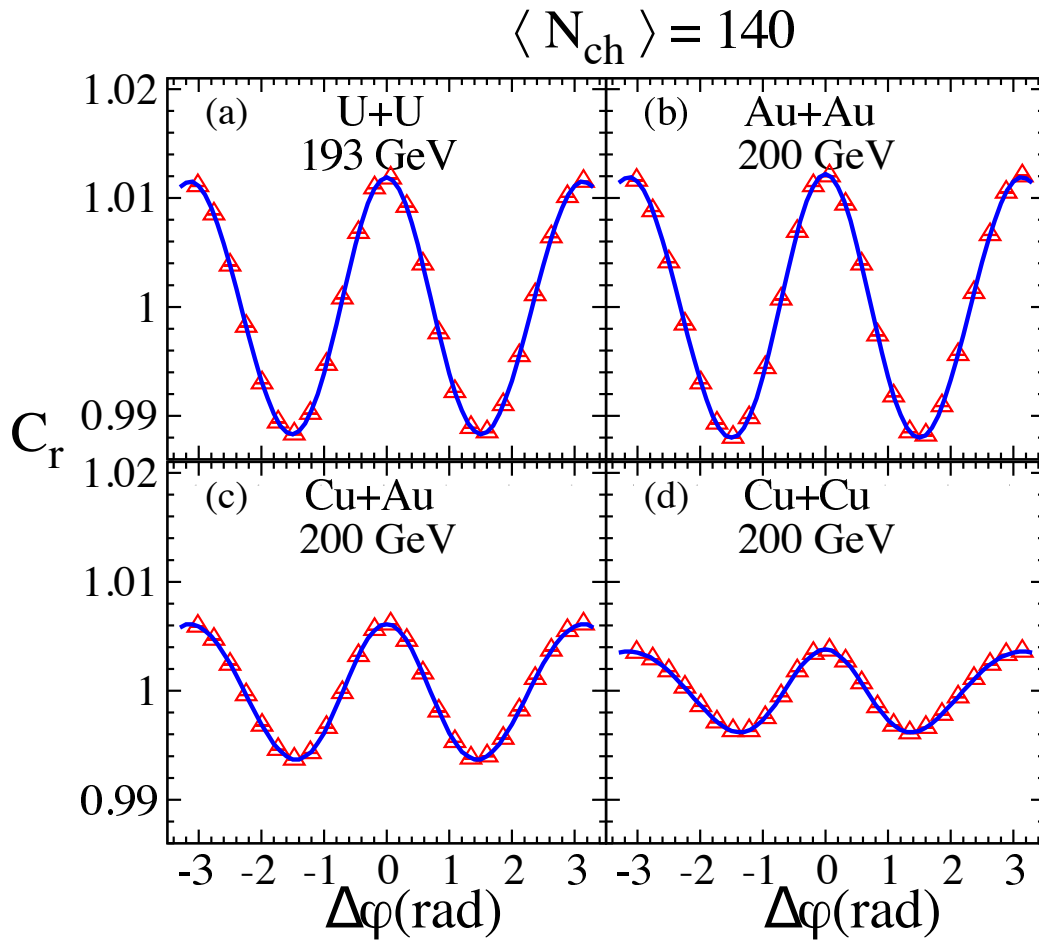


Fig. 4.12: Two-particle correlation functions for p_T -integrated track pairs with $0.7 < |\Delta\eta| < 2.0$. Results are shown for U+U (a) collisions ($\sqrt{s_{\text{NN}}} = 193$ GeV) and Au+Au (b), Cu+Au (c), and Cu+Cu (d) collisions ($\sqrt{s_{\text{NN}}} = 200$ GeV) for $\langle N_{\text{ch}} \rangle = 140$. The solid curves, show the result of a Fourier fit to the data.

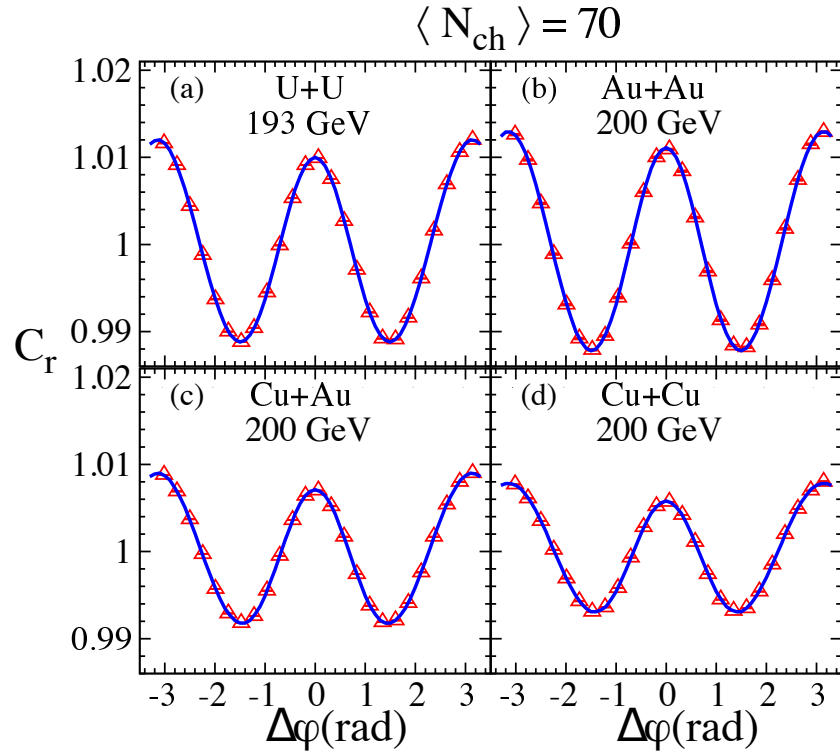


Fig. 4.13: Two-particle correlation functions for p_T -integrated track pairs with $0.7 < |\Delta\eta| < 2.0$. Results are shown for U+U (a) collisions ($\sqrt{s_{\text{NN}}} = 193$ GeV) and Au+Au (b), Cu+Au (c), and Cu+Cu (d) collisions ($\sqrt{s_{\text{NN}}} = 200$ GeV) for $\langle N_{\text{ch}} \rangle = 70$. The solid curves, show the result of a Fourier fit to the data.

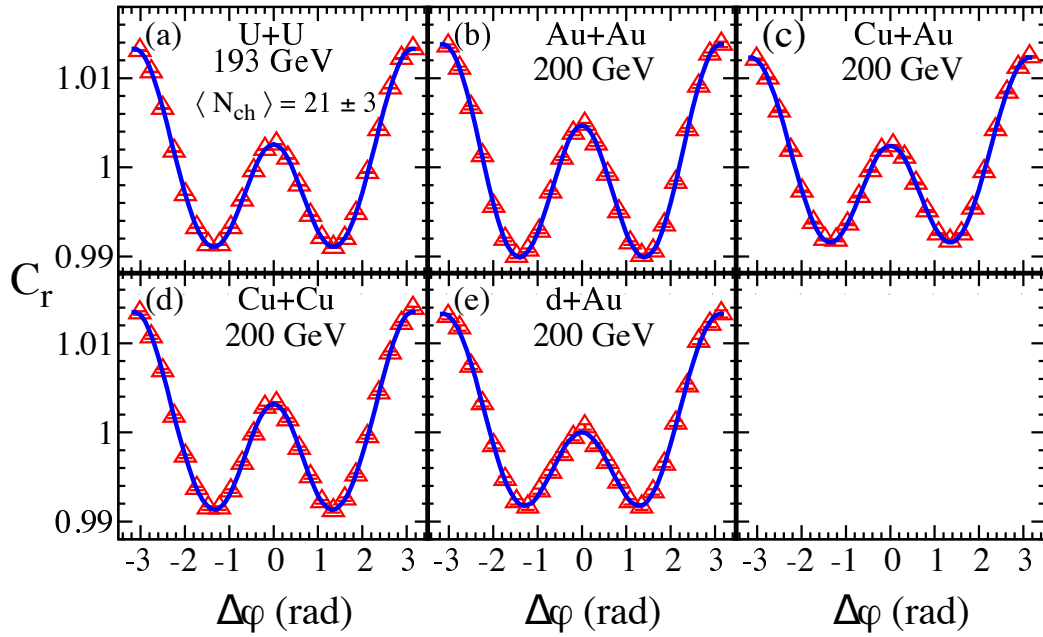


Fig. 4.14: Two-particle correlation functions for p_T -integrated track pairs with $0.7 < |\Delta\eta| < 2.0$. Results are shown for U+U (a) collisions ($\sqrt{s_{NN}} = 193$ GeV) and Au+Au (b), Cu+Au (c), Cu+Cu (d), and d+Au (e) collisions ($\sqrt{s_{NN}} = 200$ GeV) for $\langle N_{ch} \rangle = 21 \pm 3$. The solid curves, show the result of a Fourier fit to the data.

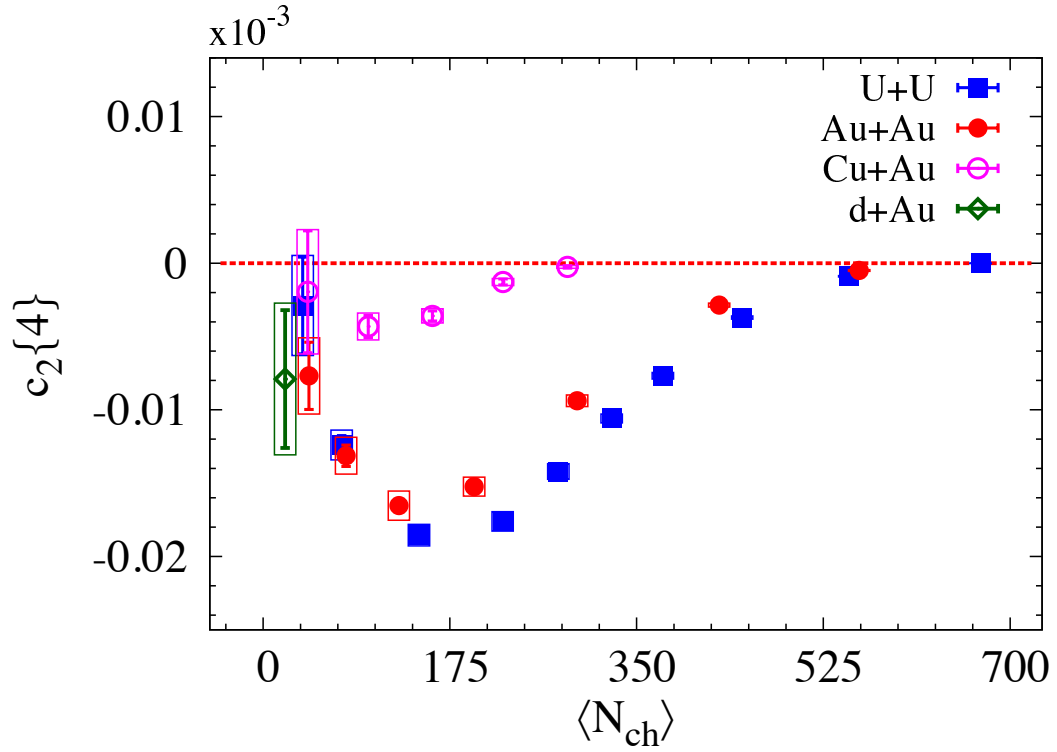


Fig. 4.15: The second-order four-particle for p_T -integrated cumulants, $c_2\{4\}$, vs. $\langle N_{ch} \rangle$, obtained for U+U (a) collisions ($\sqrt{s_{NN}} = 193$ GeV) and Au+Au (b), Cu+Au (c), Cu+Cu (d), and d+Au (e) collisions at $\sqrt{s_{NN}} = 200$ GeV.

4.2.1 An acoustic model for the viscous attenuation of flow

As discussed earlier anisotropic flow measurements are sensitive to initial conditions, the equation of state (EOS) and the transport properties of the medium. Accordingly, studying the anisotropic flow for collision systems (U+U, Cu+Au, Cu+Cu, and d+Au) at $\sqrt{s_{NN}} \sim 200$ GeV will help to understand the effect of the initial conditions on the bulk observables of the QGP. Also will give an important insight about η/s temperature dependence.

Theoretical investigations show that $v_n \propto \varepsilon_n$ for elliptic- and triangular flow ($n = 2$ and 3) [83–88], with proportionality constant that depends on the system size and the specific shear viscosity $\frac{\eta}{s}(T)$, of the created medium. This proportionality constant also known as viscous attenuation which can be understood within an acoustic model framework, akin to that for viscous relativistic hydrodynamics [108–110]:

$$\delta T_{\mu\nu}(n, t) = \exp(-\beta k^2) \delta T_{\mu\nu}(0), \quad (4.3)$$

$$\beta \propto \frac{\eta}{s} \frac{1}{R^2} \frac{t}{T} \quad (4.4)$$

where the energy-momentum tensor $T_{\mu\nu}$ incorporates the dispersion relation for sound propagation [111]. The viscous coefficient $\beta(T) \propto \frac{\eta}{s}$, $t \propto R$ is the expansion time, T is the temperature, $k = n/R$ is the wave number (*i.e.* $2\pi R = n\lambda$ for $n \geq 1$) and R is a characteristic geometric radius of the created medium.

Equation 4.3 suggests that for a given centrality, the viscous corrections to the flow harmonics v_n grow exponentially as n^2 :

$$\frac{v_n}{\varepsilon_n} \propto \exp\left(-n^2 \beta' \frac{1}{RT}\right), \quad (4.5)$$

$$\beta' \propto \frac{\eta}{s}. \quad (4.6)$$

This leads to:

$$\ln\left(\frac{v_n}{\varepsilon_n}\right) \propto -n^2 \beta' \frac{1}{RT}, \quad (4.7)$$

From entropy considerations, the dimensionless size RT , can be expressed in terms of the mean charged particle multiplicity density $\langle N_{ch} \rangle$ for a given centrality selection; $(RT)^3 \propto dN_{ch}/d\eta$ [112]. Therefore:

$$\ln \left(\frac{v_n}{\epsilon_n} \right) \propto -n^2 \beta' \langle N_{ch} \rangle^{-1/3}. \quad (4.8)$$

Consequently, Eq. 4.8 provides a transparent and consistent approach to test and compare the predicted dependence of v_n on ϵ_n , RT and $\frac{\eta}{s}$ in a given collision system – small or large [113, 114].

Equation 4.8 suggests that at a given multiplicity, the magnitude of v_n for different systems, will be controlled by ϵ_n and η/s . For different collision systems the geometrical-driven eccentricity ϵ_2 , is found to be largely dependent on the colliding systems. However the fluctuations-driven eccentricities ϵ_1 and ϵ_3 , are found to be very similar for different collision systems [115]. In the following, the measurements for v_1^{even} and v_3 are discussed separately from those for v_2 to highlight this distinction.

4.2.2 The odd flow harmonics v_1^{even} and v_3

Different sets of correlation functions were generated as a function of p_T and $\langle N_{ch} \rangle$ to allow a comparison of v_1^{even} and v_3 (for each collision system) for different dimensionless sizes ($RT \propto \langle N_{ch}^{1/3} \rangle$) and eccentricities.

The extracted values of $v_1^{even}(p_T)$, for the collision systems are compared in Fig. 4.16 for different values of $\langle N_{ch} \rangle$. Figures 4.16(a), 4.16(b) and 4.16(c) indicate similar $v_1^{even}(p_T)$ magnitudes for the systems specified at each $\langle N_{ch} \rangle$, as well as the characteristic pattern of a change from negative $v_1^{even}(p_T)$ at low- p_T , to positive $v_1^{even}(p_T)$ for $p_T \geq 1$ GeV. This pattern confirms the predicted trends for rapidity-even dipolar flow [74, 80, 95] and further indicates that for the selected values of $\langle N_{ch} \rangle$, $v_1^{even}(p_T)$ is essentially independent of collision system.

The extracted values of $v_3(p_T)$, for the different collision systems are compared in Fig. 4.17 for different values of $\langle N_{ch} \rangle$. Figures 4.17(a), 4.17(b) and 4.17(c), show similar system-independent patterns for $v_3(p_T)$, but with magnitudes and trends that differ from those for $v_1^{even}(p_T)$.

The system independence of $v_1^{even}(p_T)$ and $v_3(p_T)$ for the indicated $\langle N_{ch} \rangle$ values suggests that the fluctuation-driven initial-state eccentricities ϵ_1 and ϵ_3 , and the viscous attenuation (cf. Eq. 4.8) are similar for the indicated collision systems.

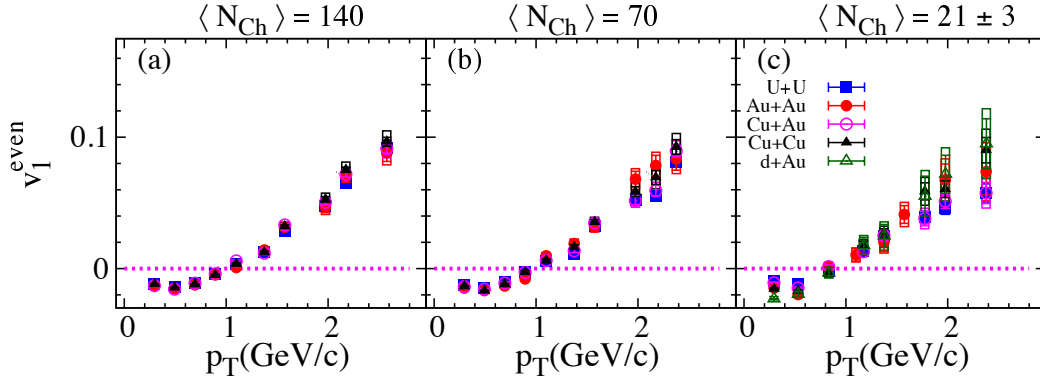


Fig. 4.16: The extracted v_1^{even} vs. p_T for several $\langle N_{ch} \rangle$ selections. Results are compared for U+U, Au+Au, Cu+Au and Cu+Cu for $\langle N_{ch} \rangle = 140$, and $\langle N_{ch} \rangle = 70$ and for U+U, Au+Au, Cu+Au, Cu+Cu and d+Au for $\langle N_{ch} \rangle = 21 \pm 3$.

The $\langle N_{ch} \rangle$ dependence of v_1^{even} is compared for all five collision systems in Fig. 4.18. For $\langle N_{ch} \rangle > 170$, the v_1^{even} values decrease with increasing values of $\langle N_{ch} \rangle$, consistent with the expected decrease of ε_1 as collisions become more central. The corresponding values of K are plotted vs. $\langle N_{ch} \rangle^{-1}$ for all five collision systems in Fig. 4.19; they show the expected linear behavior with $\langle N_{ch} \rangle^{-1}$ with comparable slopes that are related to $\langle p_T^2 \rangle$. Both Figs. 4.18 and 4.19 confirm that v_1^{even} and K are collision system independent.

The $\langle N_{ch} \rangle$ dependence of v_3 is compared for all five collision systems in Fig. 4.20. For $\langle N_{ch} \rangle > 170$ v_3 values decrease with increasing values of $\langle N_{ch} \rangle$, consistent with the expected decrease of ε_3 as collisions become more central. Figure 4.20 shows that v_3 is collision system independent.

Figures 4.18 and 4.20 indicate system-independent magnitudes and trends for v_1^{even} and v_3 analogous to the p_T -dependent results shown in Figs. 4.16 and 4.17. These results support our earlier interpretation that the fluctuation-driven values of ε_1 and ε_3 have a weak system dependence, and $\langle \frac{n}{s}(T) \rangle$ for the matter created in the respective collision systems are comparable.

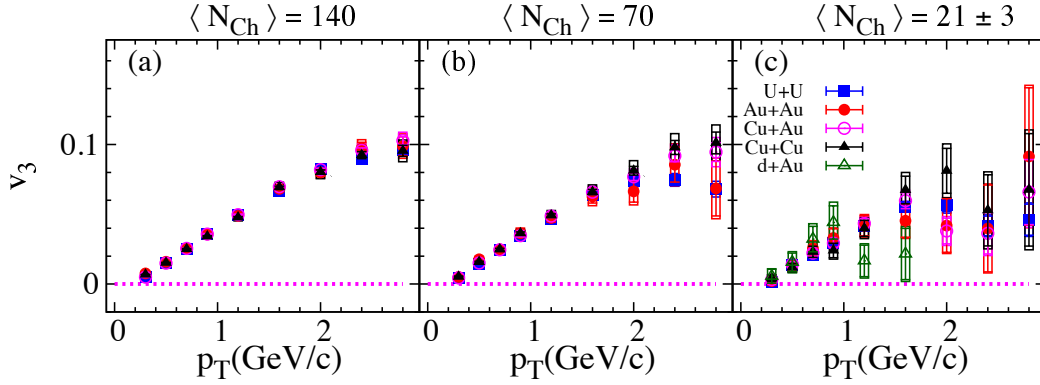


Fig. 4.17: The extracted v_3 vs. p_T for several $\langle N_{ch} \rangle$ selections. Results are compared for U+U, Au+Au, Cu+Au and Cu+Cu for $\langle N_{ch} \rangle = 140$, and $\langle N_{ch} \rangle = 70$ and for U+U, Au+Au, Cu+Au, Cu+Cu and d+Au for $\langle N_{ch} \rangle = 21 \pm 3$.

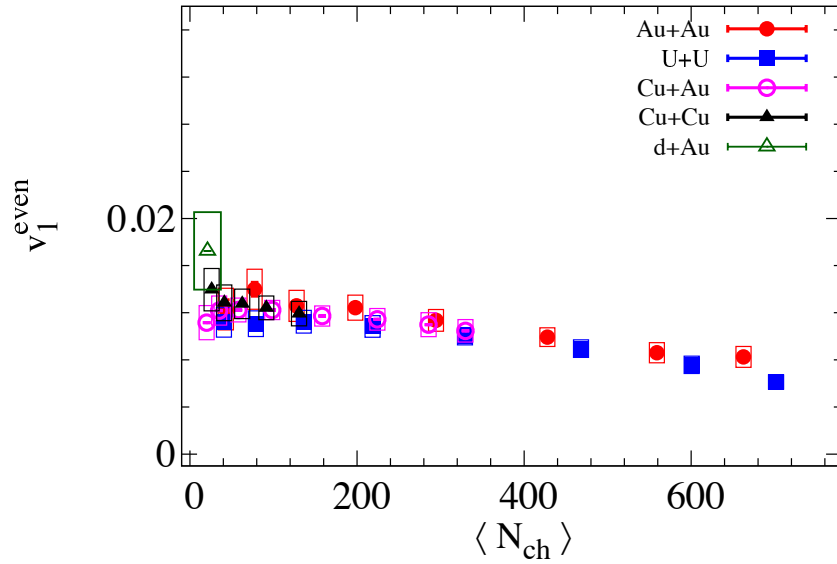


Fig. 4.18: Comparison of the $\langle N_{ch} \rangle$ dependence of v_1^{even} for all collision systems for the p_T selections $0.2 < p_T(\text{GeV}/c) < 4$. The $\langle N_{ch} \rangle$ values for d+Au correspond to $\sim 0\text{-}20\%$ central collisions.

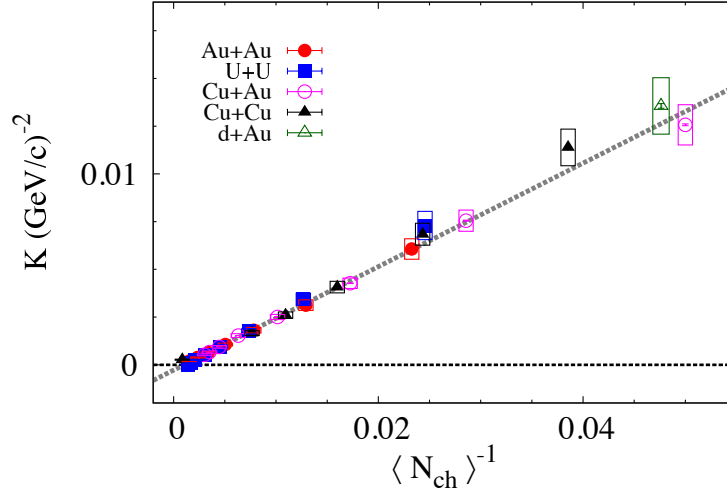


Fig. 4.19: Comparison of the $\langle N_{\text{ch}} \rangle^{-1}$ dependence of the extracted values of K for all collision systems. The dashed line represent the straight line fit.

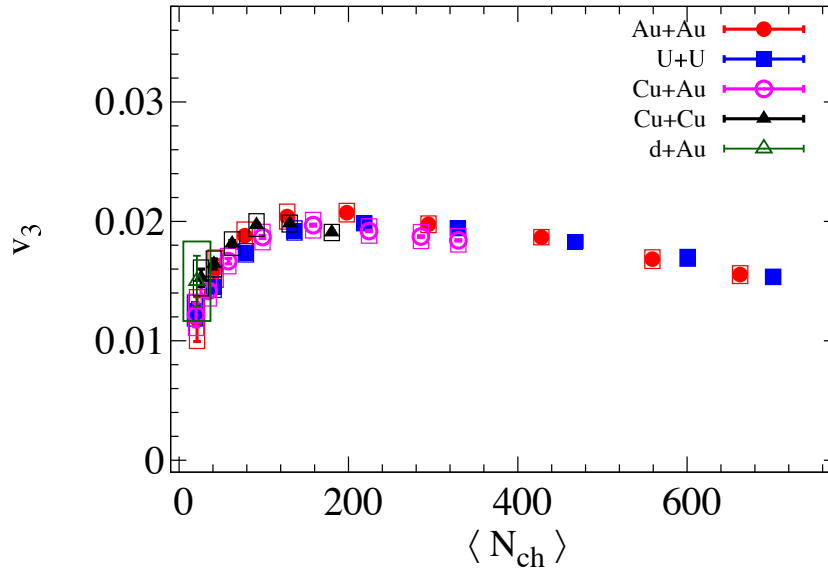


Fig. 4.20: Comparison of the $\langle N_{\text{ch}} \rangle$ dependence of v_3 for all collision systems for the p_T selections $0.2 < p_T(\text{GeV}/c) < 4$. The $\langle N_{\text{ch}} \rangle$ values for d+Au correspond to ~ 0 -20% central collisions.

4.2.3 The even flow harmonic v_2

Diverse sets of correlation functions were generated as a function of p_T and $\langle N_{\text{ch}} \rangle$ to allow a study of v_2 (for each collision system) for different dimensionless sizes ($RT \propto \langle N_{\text{ch}}^{1/3} \rangle$) and eccentricities.

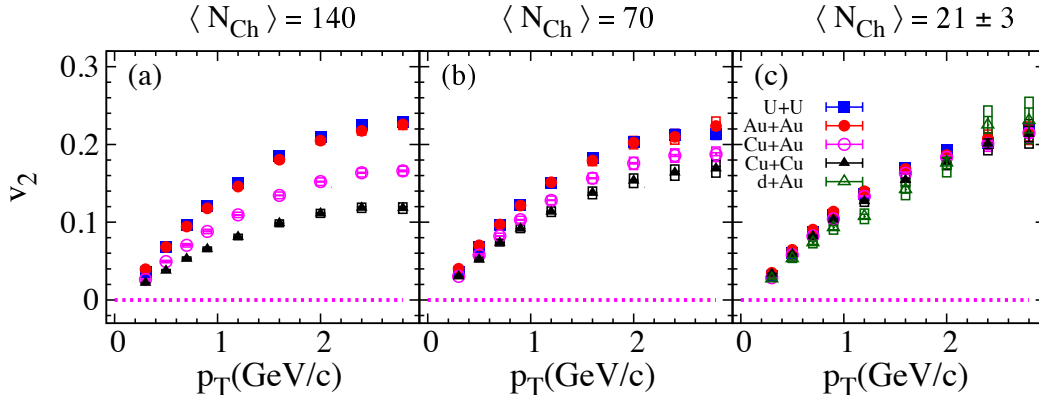


Fig. 4.21: The extracted v_2 vs. p_T for several $\langle N_{\text{ch}} \rangle$ selections. Results are compared for U+U, Au+Au, Cu+Au and Cu+Cu for $\langle N_{\text{ch}} \rangle = 140$, and $\langle N_{\text{ch}} \rangle = 70$ and for U+U, Au+Au, Cu+Au, Cu+Cu and d+Au for $\langle N_{\text{ch}} \rangle = 21 \pm 3$.

The $v_2(p_T)$ values shown in Figs. 4.21(a), (b) and (c) contrasts with those for $v_1^{\text{even}}(p_T)$ and $v_3(p_T)$. That is, the trends for a given $\langle N_{\text{ch}} \rangle$ are independent of the collision system, but the magnitudes are not system-independent, albeit with differences that grow with $\langle N_{\text{ch}} \rangle$.

The system dependent differences, apparent for $\langle N_{\text{ch}} \rangle = 140$ and 70 (Figs. 4.21(a) and 4.21(b)), can be attributed to the system-dependent ε_2 values for each $\langle N_{\text{ch}} \rangle$. For $\langle N_{\text{ch}} \rangle \sim 21$ (Fig. 4.21(c)), a residual system-dependent long-range di-jet-induced non-flow contribution could add to the observed differences.

The $\langle N_{\text{ch}} \rangle$ dependence of v_2 is compared for all five collision systems in Fig. 4.22. For $\langle N_{\text{ch}} \rangle > 170$, the v_2 values show a decrease with increasing values of $\langle N_{\text{ch}} \rangle$, consistent with the expected decrease of ε_2 as collisions become more central. The apparent decrease in the values of v_2 for $\langle N_{\text{ch}} \rangle < 170$, corroborate the dominant role of size-driven viscous attenuation of the flow harmonics for these multiplicities. Note that ε_2 increases for $\langle N_{\text{ch}} \rangle < 170$. The v_2 comparisons shown in Fig. 4.22, accentuate the system-dependent

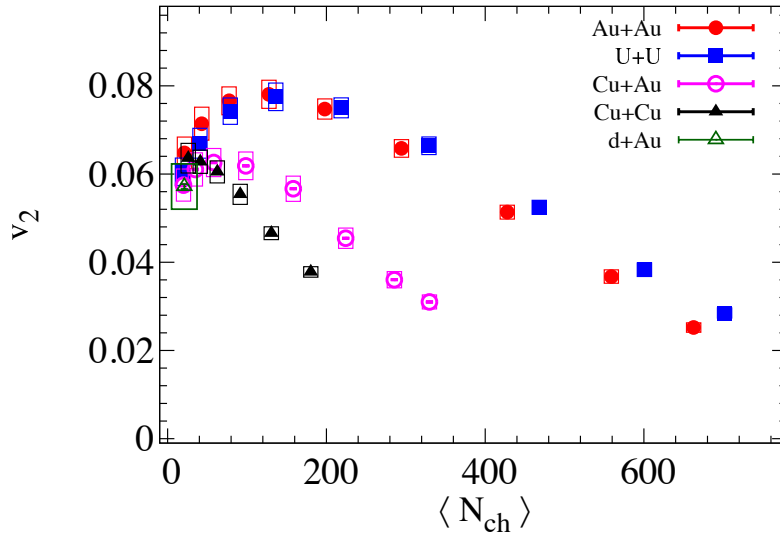


Fig. 4.22: Comparison of the $\langle N_{\text{ch}} \rangle$ dependence of v_2 for all collision systems for the p_T selections $0.2 < p_T(\text{GeV}/c) < 4$. The $\langle N_{\text{ch}} \rangle$ values for d+Au correspond to $\sim 0\text{-}20\%$ central collisions.

patterns observed in Figs. 4.22(a), 4.22(b) and 4.22(c). Here, the sizable uncertainties for the d+Au data points, reflect the systematic uncertainty estimates for residual non-flow contributions which are smaller for these p_T -integrated measurements.

4.2.4 Data scaling features

The striking system-dependent patterns shown in Figs. 4.22 and 4.21 can be attributed to the strong dependence of ε_2 on system size for a fixed value of $\langle N_{\text{ch}} \rangle$. Using the Monte Carlo Glauber (MC-Glauber) calculations [114, 116] we can compute ε_n as a function of collision centrality or $\langle N_{\text{ch}} \rangle$, and use them to scale out the effects of geometry.

Figures 4.21 (a) and (b) confirm the influence of the system-dependent ε_2 values for a given $\langle N_{\text{ch}} \rangle$. That is, they show data collapse onto a single curve for v_2/ε_2 vs. p_T as would be expected if the viscous attenuation for U+U, Au+Au, Cu+Au and Cu+Cu systems are similar (cf. Eq. 4.8). Figure 4.21 (c) shows that d+Au is following the same features of the larger systems.

This shape dependence, which weakens for low $\langle N_{\text{ch}} \rangle$, is confirmed via the plot of v_2/ε_2 vs. $\langle N_{\text{ch}} \rangle^{-1/3}$ shown in Figs. 4.24 and 4.25. Note that a linear

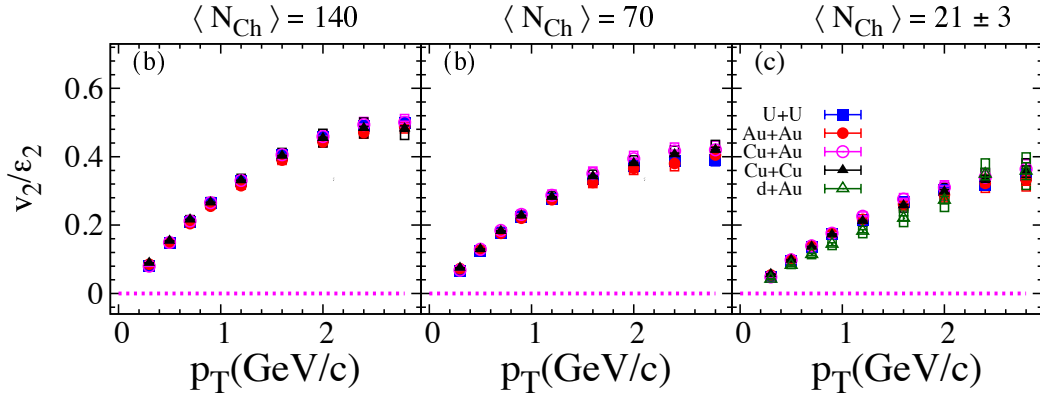


Fig. 4.23: The scaled v_2/ϵ_2 vs. p_T for several $\langle N_{\text{ch}} \rangle$ selections. Results are compared for U+U, Au+Au, Cu+Au and Cu+Cu for $\langle N_{\text{ch}} \rangle = 140$, and $\langle N_{\text{ch}} \rangle = 70$ and for U+U, Au+Au, Cu+Au, Cu+Cu and d+Au for $\langle N_{\text{ch}} \rangle = 21 \pm 3$.

dependence of $\ln(v_n/\epsilon_n)$ vs. $\langle N_{\text{ch}} \rangle^{-1/3}$ implies a slope parameter $\beta' \propto \langle \frac{\eta}{s}(T) \rangle$ within the acoustic model framework (c.f. Eq. 4.8). The inset in Fig. 4.25 indicates a marked similarity between the slopes of the eccentricity-scaled v_2 for U+U, Au+Au, Cu+Au and Cu+Cu collisions. The eccentricity-scaled results for d+Au also follow the data trend for these heavier collision species. These observations suggest that $\langle \frac{\eta}{s}(T) \rangle$ for the medium created in these systems is comparable.

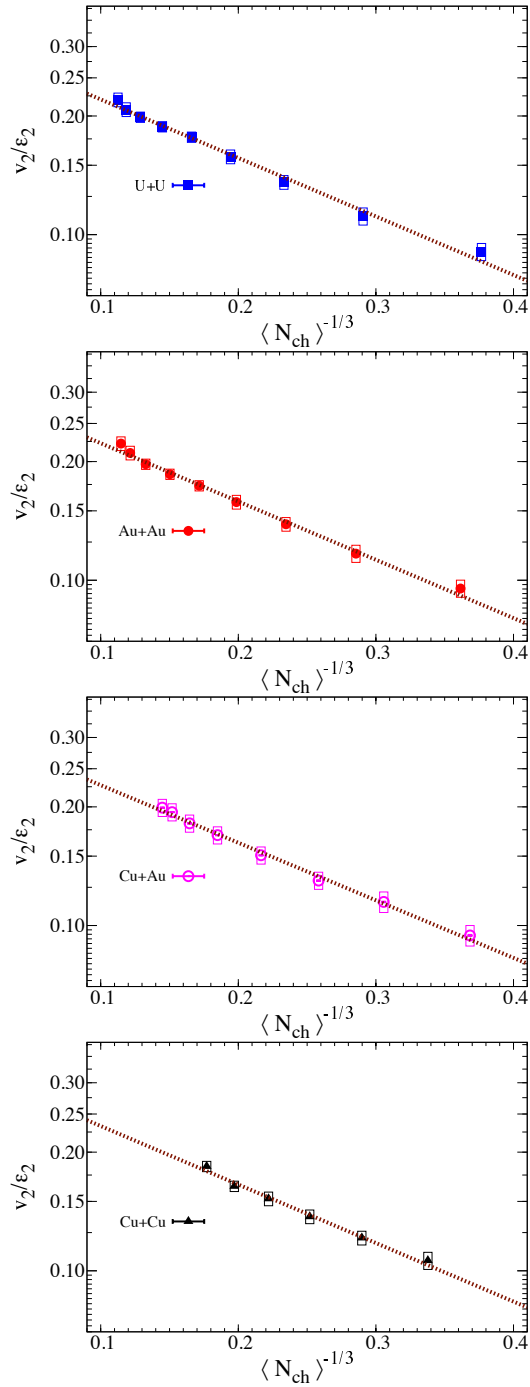


Fig. 4.24: The scaled v_2/ϵ_2 vs. $\langle N_{ch} \rangle^{-1/3}$ for all collision systems for the p_T selections $0.2 < p_T(\text{GeV}/c) < 4$. The dashed lines represent exponential fits to the data.

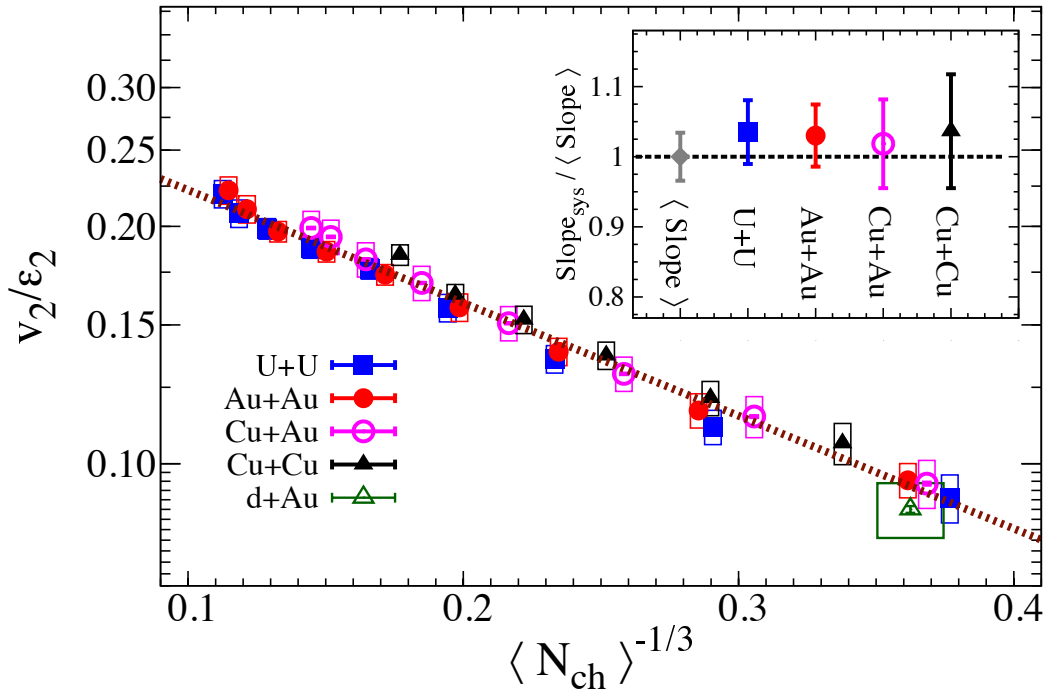


Fig. 4.25: The scaled v_2/ϵ_2 vs. $\langle N_{ch} \rangle^{-1/3}$ for all collision systems for the p_T selections $0.2 < p_T(\text{GeV}/c) < 4$. The dashed line represents an exponential fit to the data.

Chapter 5

Beam Energy and Collision System Dependence of Flow Fluctuations

The initial-state fluctuations (i.e. fluctuations of the impact parameter within a sample of events [118], as well as the fluctuations of participant positions [119–121]) influence the magnitude of the flow coefficients. Consequently, precision extraction of the specific shear viscosity of the QGP requires reliable constraints for the initial-state models employed in such extractions. Such constraints can be obtained via the two- and multi-particle flow harmonics measurements [33, 34].

As discussed before, the ratio $v_n\{4\}/v_n\{2\}$ can be used to estimate the strength of the fluctuations as a fraction of the measured flow harmonics. Thus a value for the ratio $v_n\{4\}/v_n\{2\} \sim 1$ indicates little, if any, fluctuations whereas a value less than one indicates large fluctuations.

$$\left(\frac{v_n\{4\}}{v_n\{2\}}\right)^4 = 1 - \frac{\sigma^2(v_n^2)}{\langle v_n^2 \rangle^2} \quad (5.1)$$

Therefore extensive experimental measurements of $v_n\{2\}$, $v_n\{4\}$ and $v_n\{4\}/v_n\{2\}$ can help establish whether flow fluctuations are dominated by initial- or final-state effects or both. Accordingly a comprehensive set of fluctuations measurements that span a broad range of $\sqrt{s_{NN}}$ (T , μ_B and η/s) and different collision system at a given beam energy could potentially provide, (i) unique supplemental restraints to discern between different initial-state models and

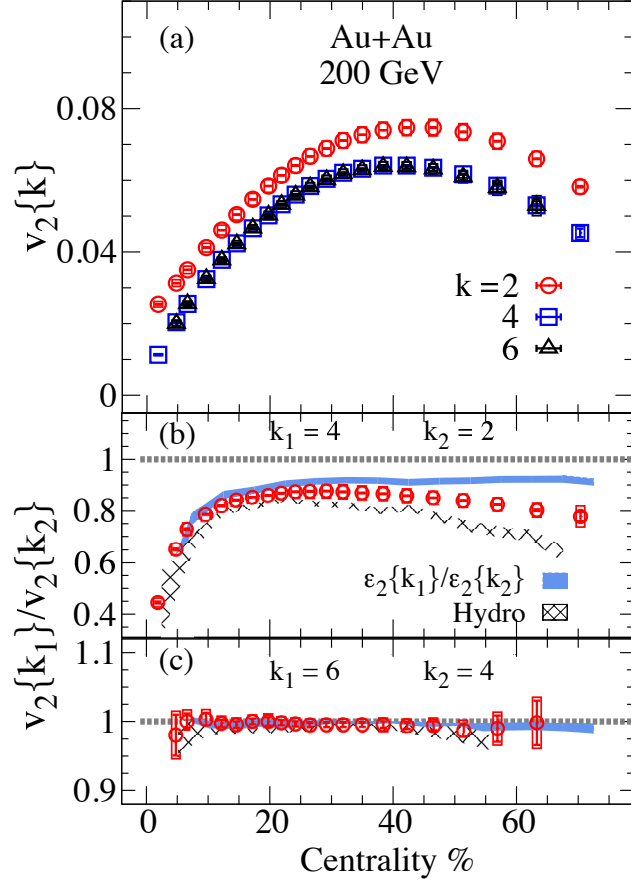


Fig. 5.1: The integrated Two-, four- and six-particle elliptic flow, $v_2\{k\}$, $k = 2, 4$ and 6 (panel a) and their ratios (panels b and c) vs. centrality for Au+Au collisions at $\sqrt{s_{NN}} = 200$ GeV. The bands represent model calculations presented in Ref [117].

(ii) reduce the fluctuations impact on the uncertainties correlated with the η/s extraction.

Illustrative examples of the integrated two-, four- and six-particle elliptic flow and their ratios vs. centrality, are presented in Fig.(5.1) (a, b and c). In panel (a), we show the characteristic centrality dependence of two-, four- and six-particle elliptic flow, as well as the good agreement between $v_2\{4\}$ and $v_2\{6\}$. The ratio $v_2\{4\}/v_2\{2\}$ which serves as a metric for elliptic flow fluctuations (panel (b)), show the expected decrease in the magnitude of the fluctuations from central to peripheral collisions, consistent with the patterns expected when initial-state eccentricity fluctuations dominate. The elliptic flow fluctuations obtained from hydrodynamic calculations [117] (grey band) over-predict the measured magnitude, while the eccentricity fluctuations appear to under-predict the measured magnitude. The latter is to be expected if eccentricity fluctuations are not the only source of the flow fluctuations.

In the following, more detailed measurements for the BES and different collision systems are presented and discussed.

5.1 Beam Energy Dependence of Flow Fluctuations

As introduced earlier, the dependence of the elliptic flow and its fluctuations on system dynamics (i.e. $\eta/s(\mu_B, T)$) can be revealed via comparisons of the measurements for Au+Au at $\sqrt{s_{NN}} = 7.7 - 200$ GeV. The two-, four and six-particle integrated elliptic flow and their ratios vs. centrality, for Au+Au at $\sqrt{s_{NN}} = 7.7 - 200$ GeV are presented in Fig.(5.2). They show an increase with beam energy. However, the elliptic flow fluctuations, ($v_2\{4\}/v_2\{2\}$) shown in Fig.(5.2) (d) show little, if any, dependence on the beam energy. By contrast, they show the expected decrease in the magnitude of the fluctuations from central to peripheral collisions, consistent with patterns expected when initial-state eccentricity fluctuations dominate. Figure.(5.2) (e) shows good agreement between four- and six-particle elliptic flow in accordance with the expectation for anisotropic flow. Accordingly, the elliptic flow fluctuation measurements for Au+Au at BES energies does not appear to depend on the system dynamics.

Event-shape selection [122] gives access to more detailed differential measurements of the fluctuations because it allows more constraints to be placed

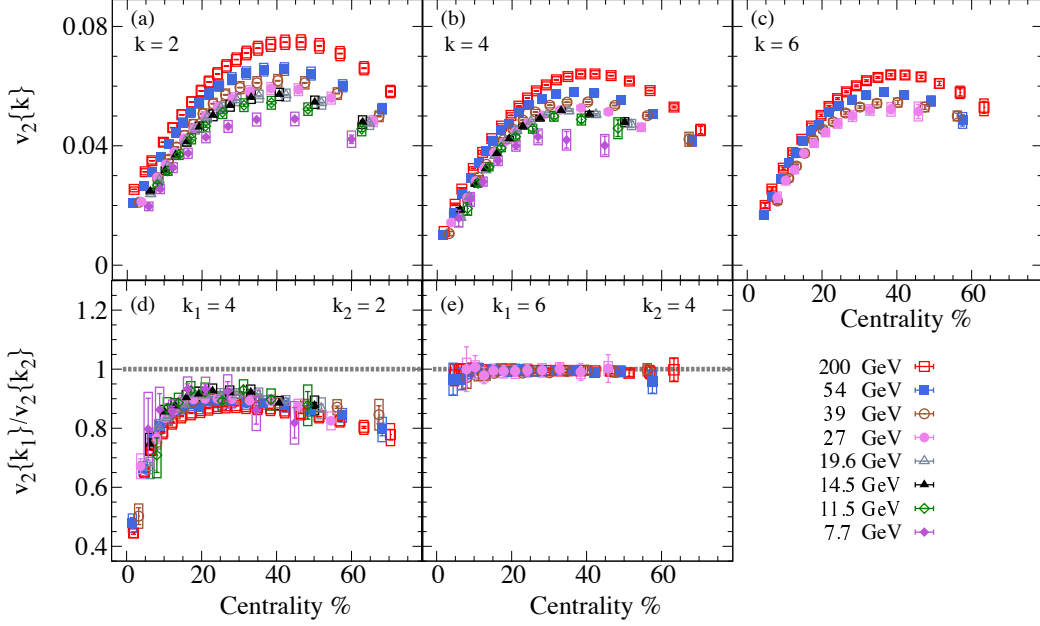


Fig. 5.2: The integrated Two-, four- and six-particle elliptic flow $v_2\{k\}$, $k = 2, 4$ and 6 (panels (a) and (b)), and their ratios (panel (c)) as a function of centrality for Au+Au collisions at $\sqrt{s_{NN}} = 7.7 - 200$ GeV.

on the initial-state fluctuations [123] by partitioning the respective centrality classes into different shape selections. Such measurements can even help to disentangle the hydrodynamic response from the initial-state effects.

Event-shape selections were made via selections on the magnitude of the second-order reduced flow vector q_2 [118, 124], defined as:

$$q_2 = \frac{|Q_2|}{\sqrt{M}}, \quad (5.2)$$

where Q_2 is the magnitude of the second-order harmonic flow vector calculated from the azimuthal distribution of particles within $|\eta| < 0.35$, and M is the charged hadron multiplicity of the same sub-event. Note that the associated flow measurements are performed for $|\eta| > 0.35$.

Figure 5.3 (a) shows that the q_2 distribution for 40 – 50% Au+Au collisions at $\sqrt{s_{NN}} = 200$ GeV is relatively broad and can accommodate several selections as indicated by the bands. Fig. (5.3) (b) illustrates the efficacy of these selections. That is, it shows a clear increase of the extracted values of

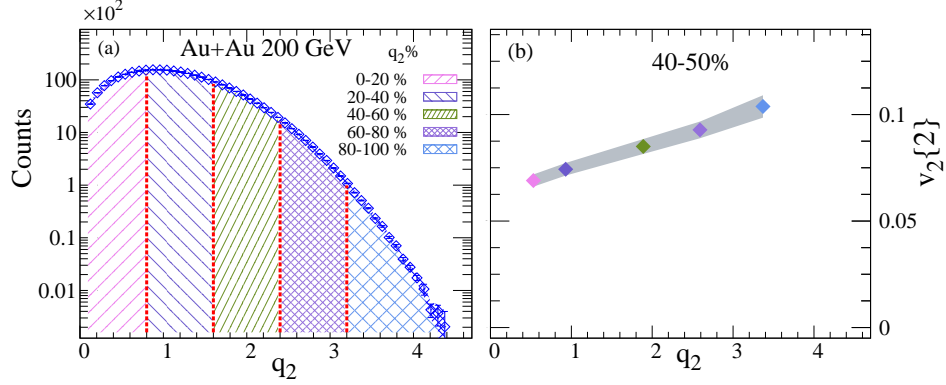


Fig. 5.3: (a) The q_2 distribution for 40 – 50% Au+Au collisions at $\sqrt{s_{NN}} = 200$ GeV, for the sub-event sample with $|\eta| < 0.35$. The indicated bands represent different $q_2\%$ selections; (b) illustrative plot of $v_2\{2\}$ as a function of q_2 for the $q_2\%$ selections in (a).

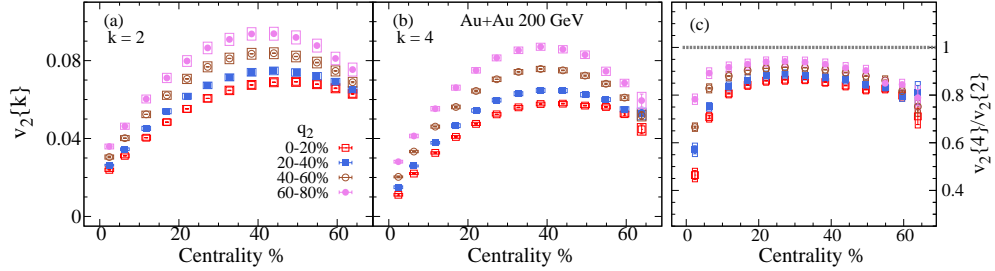


Fig. 5.4: Comparison of (a) $v_2\{2\}$, (b) $v_2\{4\}$ and (c) $v_2\{4\}/v_2\{2\}$ as a function of centrality for several q_2 selections for Au+Au collisions at $\sqrt{s_{NN}} = 200$ GeV.

$v_2\{2\}$ for $|\eta| > 0.35$ with q_2 .

The results for shape selection in Au+Au collisions at $\sqrt{s_{NN}} = 39, 54$ and 200 GeV are summarized as a function of centrality in Figs. 5.4, 5.5 and 5.6. Panels (a) and (b) indicate sizable increases for both $v_2\{2\}$ and $v_2\{4\}$ with q_2 selection. Note however, that the event-shape selections are less effective for the lower beam energies (cf. Figs. 5.5 and 5.6) due to smaller event plane resolutions at these beam energies. Figs. 5.4 - 5.6 (c) show a modest decreasing trend in the magnitude of the fluctuations with q_2 selection. Nonetheless,

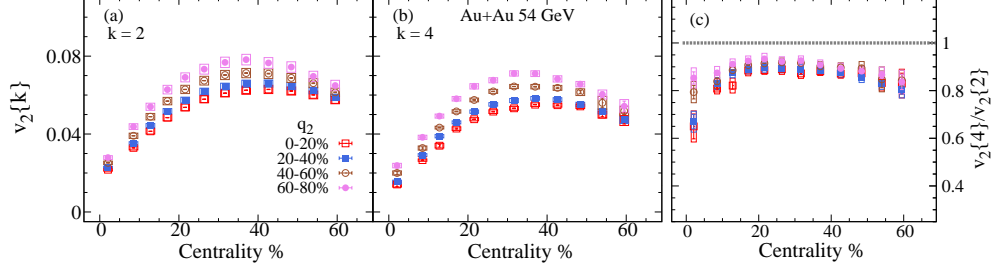


Fig. 5.5: Comparison of (a) $v_2\{2\}$, (b) $v_2\{4\}$ and (c) $v_2\{4\}/v_2\{2\}$ as a function of centrality for several q_2 selections for Au+Au collisions at $\sqrt{s_{NN}} = 54$ GeV.

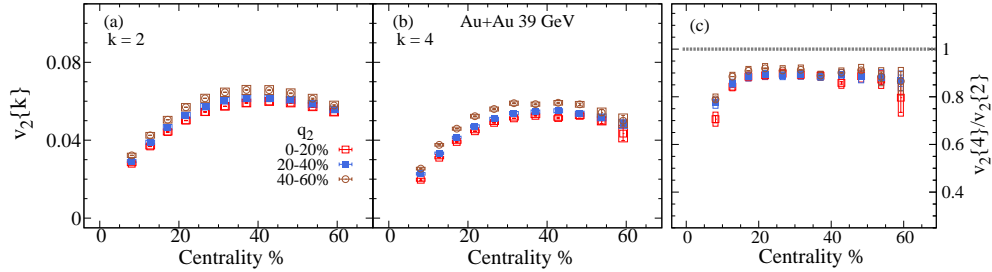


Fig. 5.6: Comparison of (a) $v_2\{2\}$, (b) $v_2\{4\}$ and (c) $v_2\{4\}/v_2\{2\}$ as a function of centrality for several q_2 selections for Au+Au collisions at $\sqrt{s_{NN}} = 39$ GeV.

the measurements indicate that the elliptic flow fluctuations are sensitive to the event-shape selection and thus provide an additional set of constraints for models.

Additional important insights on flow fluctuations can be obtained by studying the flow fluctuations of identified particles. Figs. 5.7, 5.8 and 5.9 show the two- and four-particle elliptic flow and their ratios vs. centrality for identified particles in Au+Au collisions at $\sqrt{s_{NN}} = 200, 54$ and 39 GeV respectively. The mass ordering effect on the magnitude of two- and four-particle elliptic flow can be seen in panels (a, b and c). This mass ordering effect, which cancels out for the ratio $v_2\{4\}/v_2\{2\}$, presented in panel (d), shows the expected decrease in the magnitude from central to peripheral collisions, consistent with the patterns expected when initial-state eccentricity

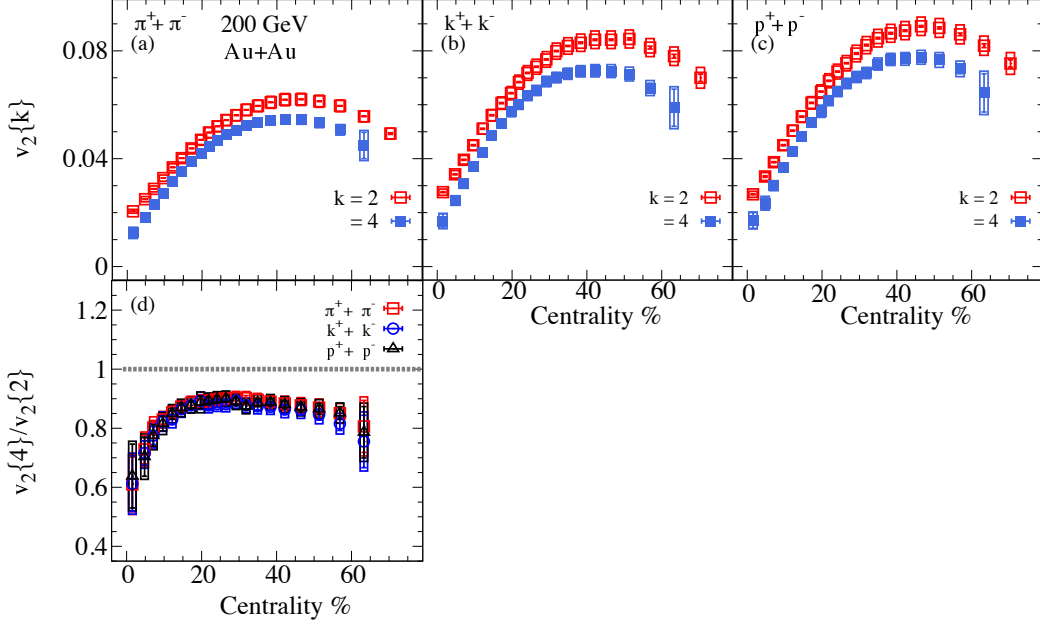


Fig. 5.7: The integrated $v_2\{2\}$, $v_2\{4\}$, and $v_2\{4\}/v_2\{2\}$ of identified hadrons as a function of centrality for Au+Au collisions at $\sqrt{s_{NN}} = 200$ GeV; are shown.

fluctuations dominate.

Further insights about the dynamical final-state fluctuations can be gained via an examination of the projection of the flow fluctuation onto a final state variable such as p_T . Fig. 5.10 shows the two- and four-particle elliptic flow coefficients and their ratio vs. p_T , for Au+Au collisions at different beam energies. The elliptic flow fluctuations ($v_2\{4\}/v_2\{2\}$), show a rather weak p_T dependence with large uncertainty for the lower beam energies. The differential measurements shown in Fig. 5.10, further suggests that the influence of the dynamical final-state fluctuations are much less than those for the initial-state-driven fluctuations.

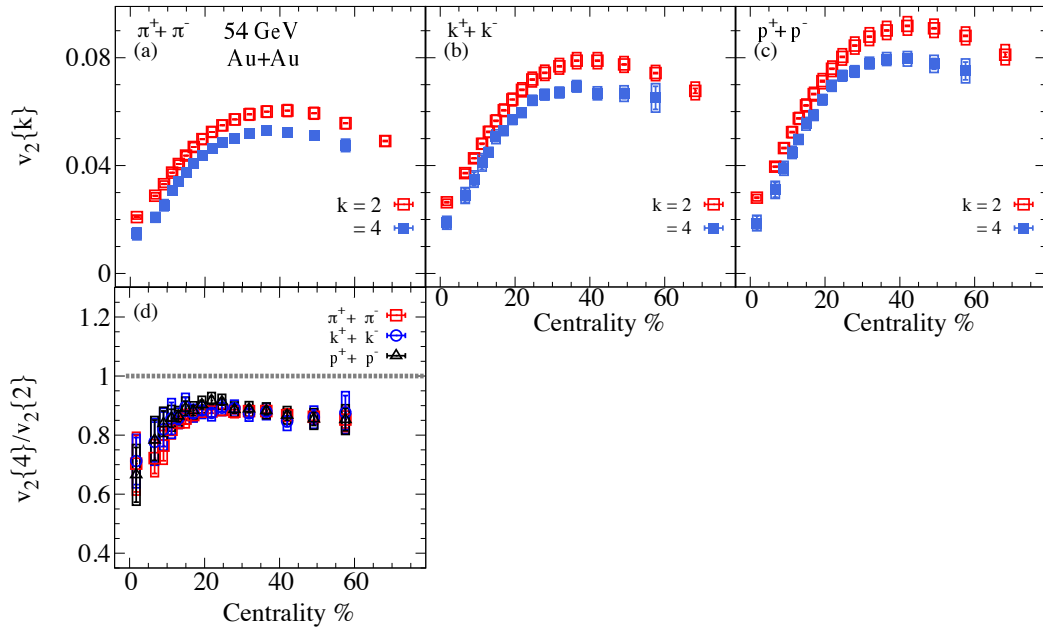


Fig. 5.8: The integrated $v_2\{2\}$, $v_2\{4\}$, and $v_2\{4\}/v_2\{2\}$ of identified hadrons as a function of centrality for Au+Au collisions at $\sqrt{s_{NN}} = 54$ GeV; are shown.

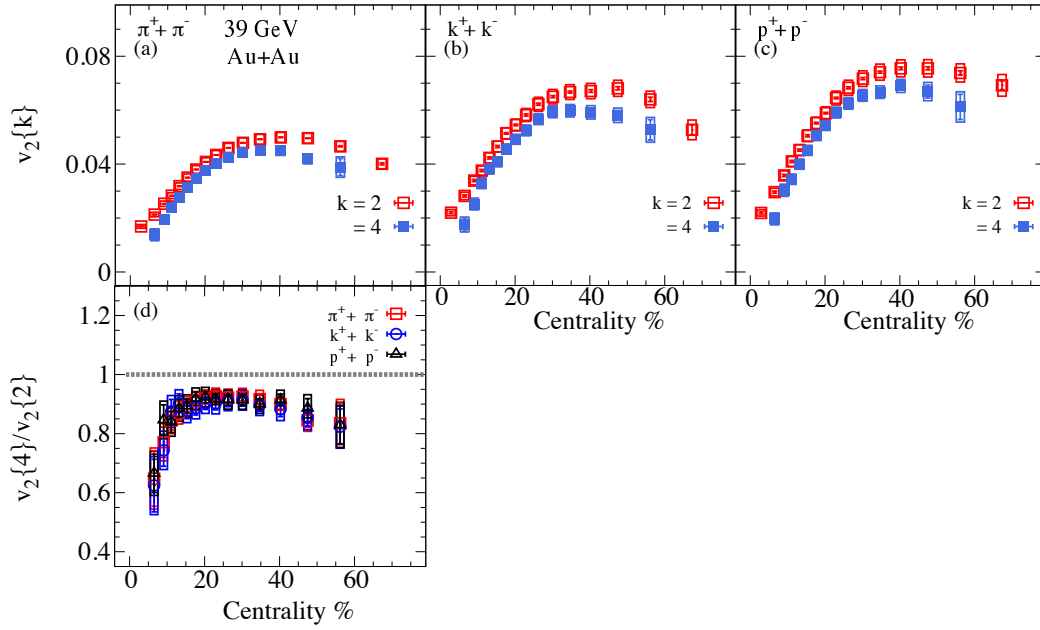


Fig. 5.9: The integrated $v_2\{2\}$, $v_2\{4\}$, and $v_2\{4\}/v_2\{2\}$ of identified hadrons as a function of centrality for Au+Au collisions at $\sqrt{s_{NN}} = 39$ GeV; are shown.

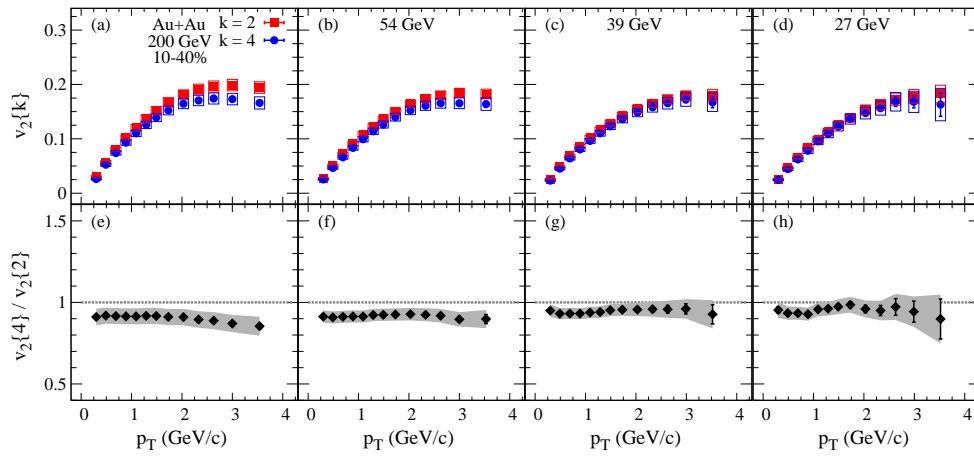


Fig. 5.10: The p_T differential $v_2\{2\}$, $v_2\{4\}$, and $v_2\{4\}/v_2\{2\}$ for Au+Au collisions at different beam energies are shown.

5.2 Collision System Dependence of Flow Fluctuations

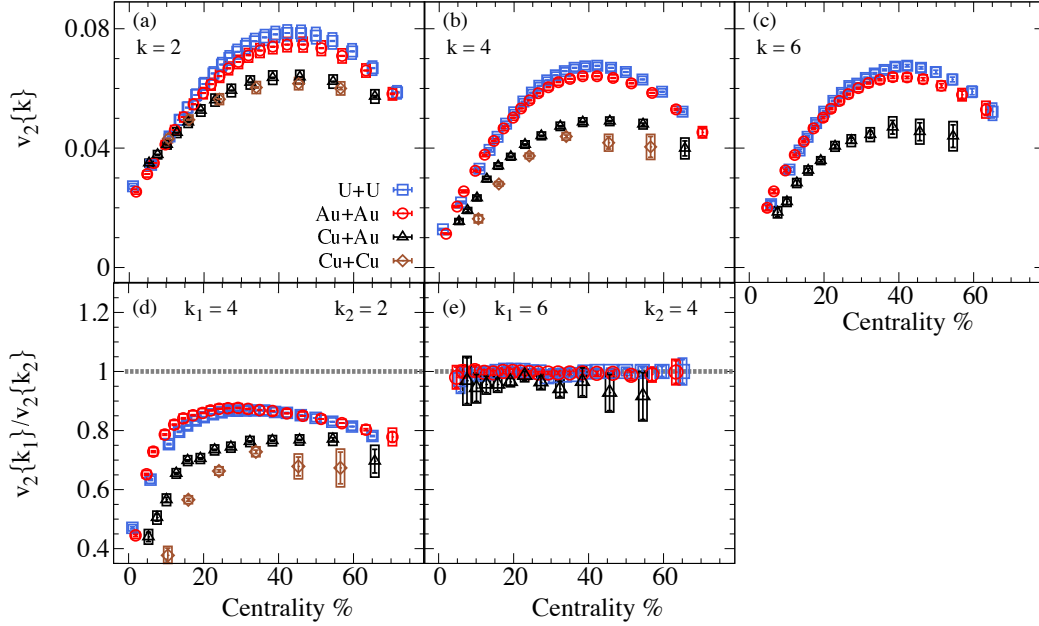


Fig. 5.11: The integrated $v_2\{2\}$, $v_2\{4\}$, $v_2\{6\}$ and their ratios as a function of centrality for U+U collisions at $\sqrt{s_{NN}} = 193$ GeV, Au+Au, Cu+Au, and Cu+Cu collisions at $\sqrt{s_{NN}} = 200$ GeV; are shown.

The BES measurements presented earlier, suggest that for a given beam energy, little if any change in η/s is to be expected for different collision systems. Therefore, fluctuations measurements for different collision systems can give important constraints for initial-state models. In this section new measurements for p_T -integrated and differential $v_2\{2\}$, $v_2\{4\}$, $v_2\{6\}$ and their ratios, are presented for U+U collisions at $\sqrt{s_{NN}} = 193$ GeV, and Au+Au, Cu+Au and Cu+Cu collisions at $\sqrt{s_{NN}} = 200$ GeV.

The integrated $v_2\{2\}$, $v_2\{4\}$, $v_2\{6\}$ and their ratios, for different collision systems, are shown in Fig.(5.11). They indicate the expected system dependent trends of $v_2\{2\}$, $v_2\{4\}$, $v_2\{6\}$, with more pronounced differences for Cu+Au and Cu+Cu, in line with the expected trends for initial-state eccentricity fluctuations [115]. Interestingly, the elliptic flow fluctuations shown in Fig.(5.11) (d), indicate similar fluctuations for the larger systems (Au+Au

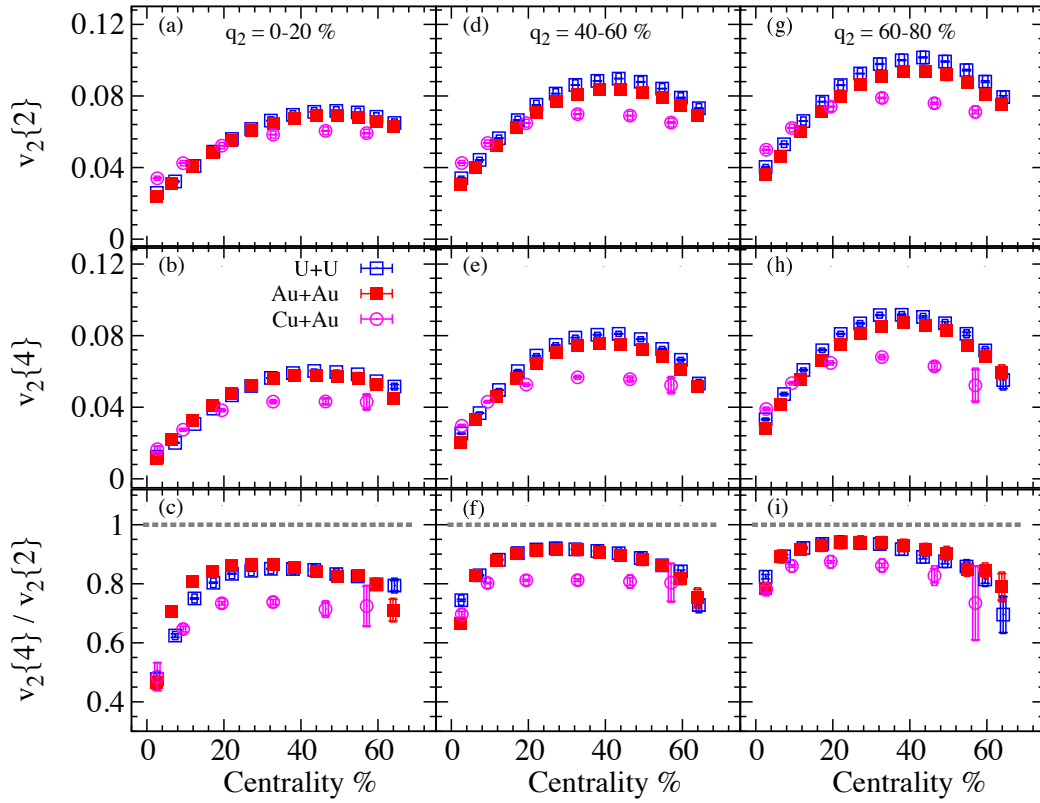


Fig. 5.12: The integrated $v_2\{2\}$, $v_2\{4\}$, and $v_2\{4\}/v_2\{2\}$ as a function of centrality for several q_2 selections for U+U collisions at $\sqrt{s_{NN}} = 193$ GeV, Au+Au and Cu+Au collisions at $\sqrt{s_{NN}} = 200$ GeV; are shown.

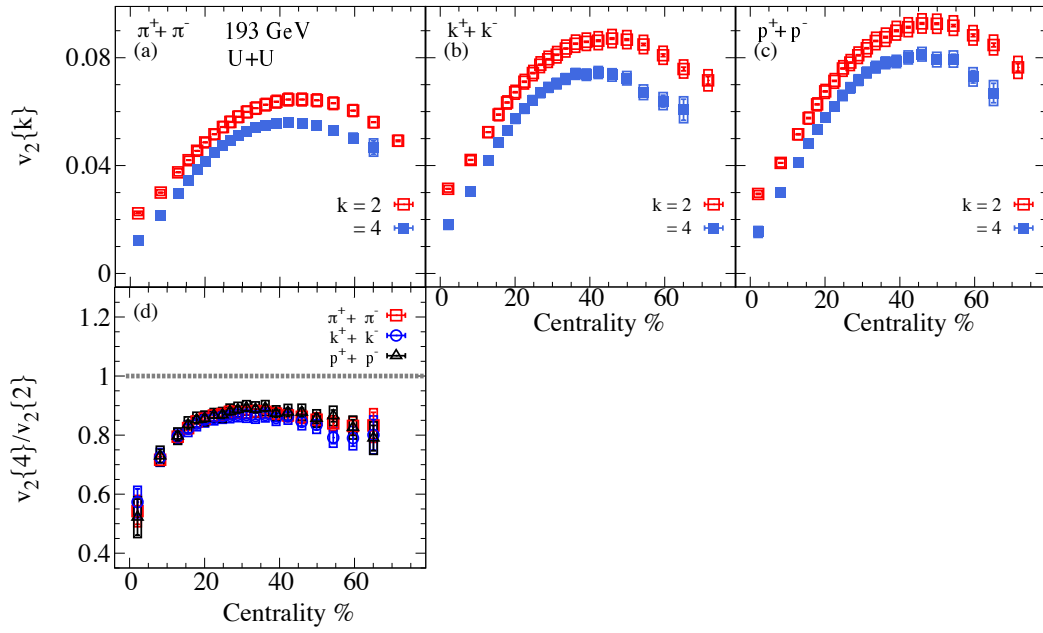


Fig. 5.13: The integrated identified hadrons $v_2\{2\}$, $v_2\{4\}$, and $v_2\{4\}/v_2\{2\}$ as a function of centrality for U+U collisions at $\sqrt{s_{NN}} = 193$ GeV; are shown.

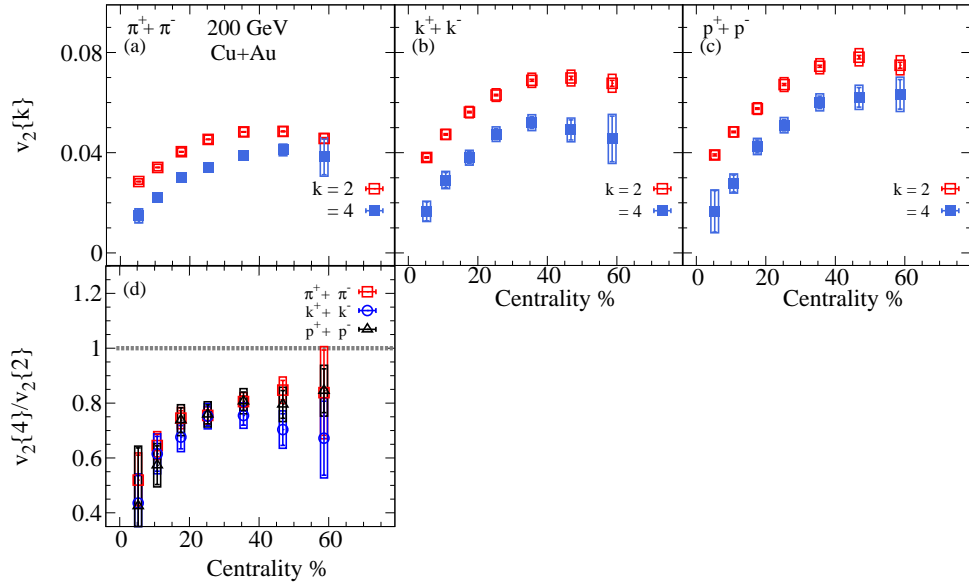


Fig. 5.14: The integrated identified hadrons $v_2\{2\}$, $v_2\{4\}$, and $v_2\{4\}/v_2\{2\}$ as a function of centrality for Cu+Au collisions at $\sqrt{s_{NN}} = 200$ GeV; are shown.

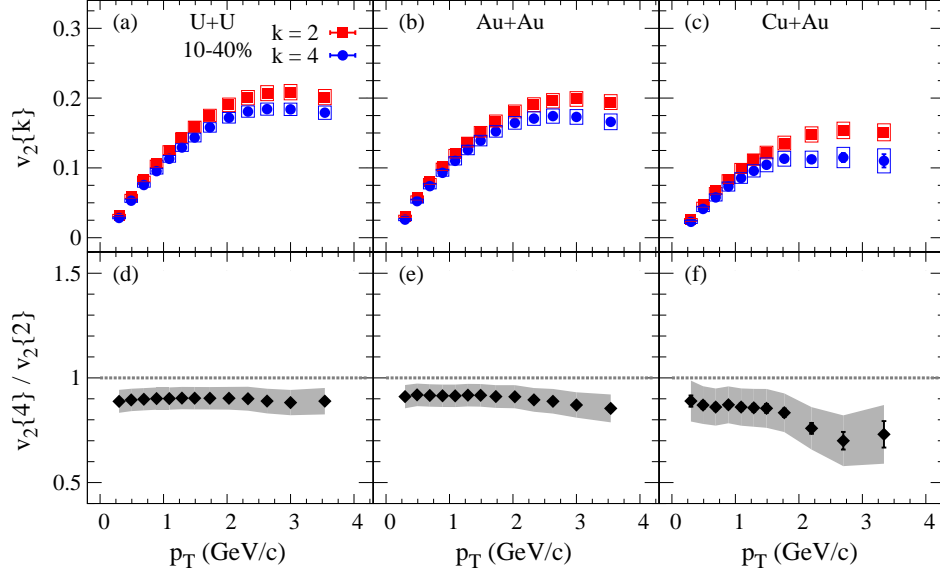


Fig. 5.15: The p_T differential $v_2\{2\}$, $v_2\{4\}$, and $v_2\{4\}/v_2\{2\}$ for different collision systems at $\sqrt{s_{NN}} \sim 200$ GeV are shown.

and U+U). This is to be expected, especially in more central collisions where the eccentricity is small. As highlighted before, these measurements indicate good agreement between the four- and six-particle elliptic flow (Fig.(5.11) (e)) as would be expected from a Gaussian distribution of the flow fluctuations.

The results for event shape selection for different collision systems, are summarized as a function of centrality in Fig. 5.12. Both $v_2\{2\}$ and $v_2\{4\}$ indicate sizable increases with the $q_2\%$ selection. By contrast, $v_2\{4\}/v_2\{2\}$ shows a more modest decreasing trend in the magnitude of the fluctuations with q_2 selection. Nonetheless, the measurements indicate that the elliptic flow fluctuations are sensitive to the event-shape selection and thus provide an additional set of constraints for models.

Figures 5.13 and 5.14 show the two- and four-particle elliptic flow and their ratios, vs. centrality for identified particles in U+U ($\sqrt{s_{NN}} = 193$ GeV) and Cu+Au collisions ($\sqrt{s_{NN}} = 200$ GeV) respectively. The mass ordering effect on the magnitude of two- and four-particle elliptic flow can be seen in panels (a, b and c). This effect, which cancels for the ratio $v_2\{4\}/v_2\{2\}$, shows the expected decrease in the magnitude from central to peripheral

collisions, consistent with patterns expected when initial-state eccentricity fluctuations dominate.

The dynamical final-state fluctuations effect is introduced in Fig 5.15; it shows the two- and four-particle elliptic flow and their ratio vs. p_T for U+U ($\sqrt{s_{NN}} = 193$ GeV), Au+Au and Cu+Au collisions ($\sqrt{s_{NN}} = 200$ GeV). The implied elliptic flow fluctuations ($v_2\{4\}/v_2\{2\}$), show a weak p_T dependence with large uncertainty for Cu+Au.

Chapter 6

Conclusion

In this work, we have used the two-particle correlation method as well as multi-particle cumulant method to carry out a comprehensive set of STAR anisotropic flow measurements for Au+Au collisions spanning the beam energy range $\sqrt{s_{NN}} = 7.7 - 200$ GeV, U+U at $\sqrt{s_{NN}} = 193$ GeV and Cu+Au, Cu+Cu and d+Au collisions at $\sqrt{s_{NN}} = 200$ GeV. The presented measurements show characteristic dependencies on centrality, $\sqrt{s_{NN}}$, η , p_T and collision system, consistent with the development of hydrodynamic-like flow in Quark-Gluon Plasma (QGP) created in these collisions. The rapidity-even dipolar flow (v_1^{even}) measurements underscore the importance of momentum conservation and the role of geometric fluctuations generated in the initial stages of the collisions. The $v_{n=2-5}$ measurements accentuate the influence of the specific shear viscosity ($\frac{\eta}{s}$), initial-state eccentricity (ϵ_n) and dimensionless size (RT), on the magnitude of v_n and its viscous attenuation in the QGP. The measurements for elliptic flow fluctuations indicate sizeable fluctuations in central collisions, a modest dependence on event-shape and system size, and a rather weak dependence on p_T , beam energy and particle species. Accordingly the elliptic flow fluctuations measurements are dominated by the initial-state eccentricity fluctuations. The detailed $v_{n \leq 5}$ and fluctuations measurements presented, give new insight into the patterns of viscous attenuation and $\frac{\eta}{s}$ for the matter created in the systems studied. The unique set of measurements spanning different systems and the BES energies, are essential to ongoing theoretical efforts to extract both the μ_B and T dependence of the specific shear viscosity $\frac{\eta}{s}$, of the quark-gluon plasma.

Bibliography

- [1] Frank Wilczek. QCD made simple. *Phys. Today*, 53N8:22–28, 2000.
- [2] Rajan Gupta. Introduction to lattice QCD: Course. In *Probing the standard model of particle interactions. Proceedings, Summer School in Theoretical Physics, NATO Advanced Study Institute, 68th session, Les Houches, France, July 28-September 5, 1997. Pt. 1, 2*, pages 83–219, 1997.
- [3] Torbjorn Sjostrand, Stephen Mrenna, and Peter Z. Skands. PYTHIA 6.4 Physics and Manual. *JHEP*, 05:026, 2006.
- [4] Miklos Gyulassy and Xin-Nian Wang. HIJING 1.0: A Monte Carlo program for parton and particle production in high-energy hadronic and nuclear collisions. *Comput. Phys. Commun.*, 83:307, 1994.
- [5] N. Cabibbo and G. Parisi. Exponential Hadronic Spectrum and Quark Liberation. *Phys. Lett.*, 59B:67–69, 1975.
- [6] R. Hagedorn and J. Ranft. *Nuovo Cimento Suppl.*, 6:169, 1968.
- [7] Shinji Ejiri. Canonical partition function and finite density phase transition in lattice QCD. *Phys. Rev.*, D78:074507, 2008.
- [8] Robert D. Pisarski and Frank Wilczek. Remarks on the Chiral Phase Transition in Chromodynamics. *Phys. Rev.*, D29:338–341, 1984.
- [9] M. Asakawa and K. Yazaki. Chiral Restoration at Finite Density and Temperature. *Nucl. Phys.*, A504:668–684, 1989.
- [10] Adam Miklos Halasz, A. D. Jackson, R. E. Shrock, Misha A. Stephanov, and J. J. M. Verbaarschot. On the phase diagram of QCD. *Phys. Rev.*, D58:096007, 1998.

- [11] Yoshitaka Hatta and Takashi Ikeda. Universality, the QCD critical / tricritical point and the quark number susceptibility. *Phys. Rev.*, D67:014028, 2003.
- [12] E. Scott Bowman and Joseph I. Kapusta. Critical Points in the Linear Sigma Model with Quarks. *Phys. Rev.*, C79:015202, 2009.
- [13] Y. Aoki, G. Endrodi, Z. Fodor, S. D. Katz, and K. K. Szabo. The Order of the quantum chromodynamics transition predicted by the standard model of particle physics. *Nature*, 443:675–678, 2006.
- [14] Frank R. Brown, Frank P. Butler, Hong Chen, Norman H. Christ, Zhihua Dong, Wendy Schaffer, Leo I. Unger, and Alessandro Vaccarino. On the existence of a phase transition for QCD with three light quarks. *Phys. Rev. Lett.*, 65:2491–2494, 1990.
- [15] Frank Wilczek. From notes to chords in QCD. *Nucl. Phys.*, A642:1–13, 1998.
- [16] W. Greiner, J. Reinhardt, M. G. Itkis, and M. C. Guclu. Structure and dynamics of elementary matter. Proceedings, NATO Advanced Study Institute, Camyuva-Kemer, Turkey, September 22-October 2, 2003. *Dordrecht, Netherlands: Kluwer Academic (2004) 675 p*, 2004.
- [17] Roman Pasechnik and Michal umbera. Phenomenological Review on QuarkGluon Plasma: Concepts vs. Observations. *Universe*, 3(1):7, 2017.
- [18] Chun Shen, Zhi Qiu, Huichao Song, Jonah Bernhard, Steffen Bass, and Ulrich Heinz. The iEBE-VISHNU code package for relativistic heavy-ion collisions. *Comput. Phys. Commun.*, 199:61–85, 2016.
- [19] Ulrich W. Heinz and Maurice Jacob. Evidence for a new state of matter: An Assessment of the results from the CERN lead beam program. 2000.
- [20] P. Fachini. Experimental highlights of the RHIC program. *AIP Conf. Proc.*, 857:62–75, 2006. [,62(2006)].
- [21] K. Safarik. Physics programme of ALICE experiment. *Nucl. Phys.*, A749:229–242, 2005.

- [22] W. F. Henning. FAIR and its experimental program. *J. Phys.*, G34:S551–S557, 2007.
- [23] Alexander Sorin, Vladimir Kekelidze, Alexander Kovalenko, Richard Lednicky, Igor Meshkov, and Grigory Trubnikov. Heavy-ion program at NICA/MPD at JINR. *Nucl. Phys.*, A855:510–513, 2011.
- [24] E. B. Forsyth and C. Lasky. Engineering Design of the AGS Fast Beam Extraction System. *IEEE Trans. Nucl. Sci.*, 12:882, 1965.
- [25] E. Malwitz et al. CERN heavy-ion facility design report . Number CERN-93-01. CERN, 1993. 1993.
- [26] J. Cleymans, H. Oeschler, K. Redlich, and S. Wheaton. Comparison of chemical freeze-out criteria in heavy-ion collisions. *Phys. Rev.*, C73:034905, 2006.
- [27] Guang-You Qin. Anisotropic Flow and Jet Quenching in Relativistic Nuclear Collisions. *Int. J. Mod. Phys.*, E24(02):1530001, 2015.
- [28] Raimond Snellings. Elliptic Flow: A Brief Review. *New J. Phys.*, 13:055008, 2011.
- [29] Paul Sorensen. Elliptic Flow: A Study of Space-Momentum Correlations In Relativistic Nuclear Collisions. 2009.
- [30] Roy A. Lacey. The Role of elliptic flow correlations in the discovery of the sQGP at RHIC. *Nucl. Phys.*, A774:199–214, 2006.
- [31] Nicolas Borghini, Phuong Mai Dinh, and Jean-Yves Ollitrault. A New method for measuring azimuthal distributions in nucleus-nucleus collisions. *Phys. Rev.*, C63:054906, 2001.
- [32] Ante Bilandzic, Raimond Snellings, and Sergei Voloshin. Flow analysis with cumulants: Direct calculations. *Phys. Rev.*, C83:044913, 2011.
- [33] Ante Bilandzic, Christian Holm Christensen, Kristjan Gulbrandsen, Alexander Hansen, and You Zhou. Generic framework for anisotropic flow analyses with multiparticle azimuthal correlations. *Phys. Rev.*, C89(6):064904, 2014.

- [34] Jiangyong Jia, Mingliang Zhou, and Adam Trzupek. Revealing long-range multiparticle collectivity in small collision systems via subevent cumulants. *Phys. Rev.*, C96(3):034906, 2017.
- [35] M. E. Beddo et al. STAR: Conceptual design report for the Solenoidal Tracker at RHIC. 1992.
- [36] M. Anderson et al. The Star time projection chamber: A Unique tool for studying high multiplicity events at RHIC. *Nucl. Instrum. Meth.*, A499:659–678, 2003.
- [37] M. Harrison, T. Ludlam, and S. Ozaki. RHIC project overview. *Nucl. Instrum. Meth.*, A499:235–244, 2003.
- [38] L. C. Bland. Spin physics with the STAR detector. *RIKEN Rev.*, 28:8–14, 2000.
- [39] M. Anderson et al. The Star time projection chamber: A Unique tool for studying high multiplicity events at RHIC. *Nucl. Instrum. Meth.*, A499:659–678, 2003.
- [40] W. J. Llope et al. The TOFp / pVPD time-of-flight system for STAR. *Nucl. Instrum. Meth.*, A522:252–273, 2004.
- [41] Ji Xu. Talk at RHIC and AGS User Meeting 2016.
- [42] Michael L. Miller, Klaus Reygers, Stephen J. Sanders, and Peter Steinberg. Glauber modeling in high energy nuclear collisions. *Ann. Rev. Nucl. Part. Sci.*, 57:205–243, 2007.
- [43] Derek Teaney. The Effects of viscosity on spectra, elliptic flow, and HBT radii. *Phys.Rev.*, C68:034913, 2003.
- [44] Roy A. Lacey and Arkadij Taranenko. What do elliptic flow measurements tell us about the matter created in the little bang at RHIC? *PoS*, CFRNC2006:021, 2006.
- [45] Roy A. Lacey, N.N. Ajitanand, J.M. Alexander, P. Chung, W.G. Holzmann, et al. Has the QCD Critical Point been Signaled by Observations at RHIC? *Phys.Rev.Lett.*, 98:092301, 2007.

- [46] A. Adare et al. Energy Loss and Flow of Heavy Quarks in Au+Au Collisions at $s(\text{NN})^{1/2} = 200\text{-GeV}$. *Phys.Rev.Lett.*, 98:172301, 2007.
- [47] Hans-Joachim Drescher, Adrian Dumitru, Clement Gombeaud, and Jean-Yves Ollitrault. The Centrality dependence of elliptic flow, the hydrodynamic limit, and the viscosity of hot QCD. *Phys.Rev.*, C76:024905, 2007.
- [48] K. Dusling and D. Teaney. Simulating elliptic flow with viscous hydrodynamics. *Phys.Rev.*, C77:034905, 2008.
- [49] Zhe Xu, Carsten Greiner, and Horst Stocker. PQCD calculations of elliptic flow and shear viscosity at RHIC. *Phys.Rev.Lett.*, 101:082302, 2008.
- [50] Denes Molnar and Pasi Huovinen. Dissipative effects from transport and viscous hydrodynamics. *J.Phys.*, G35:104125, 2008.
- [51] Roy A. Lacey, Arkadij Taranenko, and Rui Wei. Is the quark gluon plasma produced in RHIC collisions strongly coupled? 2009.
- [52] Kevin Dusling, Guy D. Moore, and Derek Teaney. Radiative energy loss and $v(2)$ spectra for viscous hydrodynamics. *Phys.Rev.*, C81:034907, 2010.
- [53] A.K. Chaudhuri. Centrality dependence of elliptic flow and QGP viscosity. *J.Phys.*, G37:075011, 2010.
- [54] Roy A. Lacey, A. Taranenko, R. Wei, N.N. Ajitanand, J.M. Alexander, et al. Azimuthal anisotropy: transition from hydrodynamic flow to jet suppression. *Phys.Rev.*, C82:034910, 2010.
- [55] Paul Romatschke and Ulrike Romatschke. Viscosity Information from Relativistic Nuclear Collisions: How Perfect is the Fluid Observed at RHIC? *Phys.Rev.Lett.*, 99:172301, 2007.
- [56] Sergei A. Voloshin, Arthur M. Poskanzer, and Raimond Snellings. Collective phenomena in non-central nuclear collisions. 2008.
- [57] Matthew Luzum and Paul Romatschke. Conformal Relativistic Viscous Hydrodynamics: Applications to RHIC results at $s(\text{NN})^{1/2} = 200\text{-GeV}$. *Phys.Rev.*, C78:034915, 2008.

- [58] Matthew Luzum and Paul Romatschke. Viscous Hydrodynamic Predictions for Nuclear Collisions at the LHC. *Phys.Rev.Lett.*, 103:262302, 2009.
- [59] Huichao Song, Steffen A. Bass, Ulrich Heinz, Tetsufumi Hirano, and Chun Shen. 200 A GeV Au+Au collisions serve a nearly perfect quark-gluon liquid. *Phys.Rev.Lett.*, 106:192301, 2011.
- [60] K Aamodt et al. Elliptic flow of charged particles in Pb-Pb collisions at 2.76 TeV. *Phys.Rev.Lett.*, 105:252302, 2010.
- [61] Matthew Luzum. Elliptic flow at energies available at the CERN Large Hadron Collider: Comparing heavy-ion data to viscous hydrodynamic predictions. *Phys.Rev.*, C83:044911, 2011.
- [62] Roy A. Lacey, A. Taranenko, N.N. Ajitanand, and J.M. Alexander. Initial indications for the production of a strongly coupled plasma in Pb+Pb collisions at $\sqrt{s_{NN}} = 2.76$ TeV. *Phys.Rev.*, C83:031901, 2011.
- [63] Piotr Bozek, Mikolaj Chojnacki, Wojciech Florkowski, and Boris Tomasik. Hydrodynamic predictions for Pb+Pb collisions at $\sqrt{s_{NN}} = 2.76$ TeV. *Phys.Lett.*, B694:238–241, 2010.
- [64] Tetsufumi Hirano, Pasi Huovinen, and Yasushi Nara. Elliptic flow in U+U collisions at $\sqrt{s_{NN}} = 200$ GeV and in Pb+Pb collisions at $\sqrt{s_{NN}} = 2.76$ TeV: Prediction from a hybrid approach. *Phys.Rev.*, C83:021902, 2011.
- [65] Bjorn Schenke, Sangyong Jeon, and Charles Gale. Elliptic and triangular flow in event-by-event (3+1)D viscous hydrodynamics. *Phys.Rev.Lett.*, 106:042301, 2011.
- [66] Bjoern Schenke, Sangyong Jeon, and Charles Gale. Anisotropic flow in $\sqrt{s} = 2.76$ TeV Pb+Pb collisions at the LHC. *Phys.Lett.*, B702:59–63, 2011.
- [67] Huichao Song, Steffen A. Bass, and Ulrich Heinz. Elliptic flow in 200 A GeV Au+Au collisions and 2.76 A TeV Pb+Pb collisions: insights from viscous hydrodynamics + hadron cascade hybrid model. *Phys.Rev.*, C83:054912, 2011.

- [68] Chun Shen, Ulrich Heinz, Pasi Huovinen, and Huichao Song. Systematic parameter study of hadron spectra and elliptic flow from viscous hydrodynamic simulations of Au+Au collisions at $\sqrt{s_{NN}} = 200$ GeV. *Phys.Rev.*, C82:054904, 2010.
- [69] Fernando G. Gardim, Frederique Grassi, Matthew Luzum, and Jean-Yves Ollitrault. Anisotropic flow in event-by-event ideal hydrodynamic simulations of $\sqrt{s_{NN}} = 200$ GeV Au+Au collisions. *Phys.Rev.Lett.*, 109:202302, 2012.
- [70] H. Niemi, G.S. Denicol, P. Huovinen, E. Molnar, and D.H. Rischke. Influence of a temperature-dependent shear viscosity on the azimuthal asymmetries of transverse momentum spectra in ultrarelativistic heavy-ion collisions. *Phys.Rev.*, C86:014909, 2012.
- [71] Guang-You Qin, Hannah Petersen, Steffen A. Bass, and Berndt Muller. Translation of collision geometry fluctuations into momentum anisotropies in relativistic heavy-ion collisions. *Phys.Rev.*, C82:064903, 2010.
- [72] Sergei A. Voloshin, Arthur M. Poskanzer, Aihong Tang, and Gang Wang. Elliptic flow in the Gaussian model of eccentricity fluctuations. *Phys. Lett.*, B659:537–541, 2008.
- [73] Matthew Luzum and Jean-Yves Ollitrault. Directed flow at midrapidity in heavy-ion collisions. *Phys. Rev. Lett.*, 106:102301, 2011.
- [74] Ekaterina Retinskaya, Matthew Luzum, and Jean-Yves Ollitrault. Directed flow at midrapidity in $\sqrt{s_{NN}} = 2.76$ TeV Pb+Pb collisions. *Phys. Rev. Lett.*, 108:252302, 2012.
- [75] Georges Aad et al. Measurement of the azimuthal anisotropy for charged particle production in $\sqrt{s_{NN}} = 2.76$ TeV lead-lead collisions with the ATLAS detector. *Phys. Rev.*, C86:014907, 2012.
- [76] Matthew Luzum. Flow fluctuations and long-range correlations: elliptic flow and beyond. *J. Phys.*, G38:124026, 2011.
- [77] K. Aamodt et al. Harmonic decomposition of two-particle angular correlations in Pb-Pb collisions at $\sqrt{s_{NN}} = 2.76$ TeV. *Phys. Lett.*, B708:249–264, 2012.

- [78] Nicolas Borghini, Phuong Mai Dinh, and Jean-Yves Ollitrault. Are flow measurements at SPS reliable? *Phys. Rev.*, C62:034902, 2000.
- [79] Jiangyong Jia, Sooraj K. Radhakrishnan, and Soumya Mohapatra. A study of the anisotropy associated with dipole asymmetry in heavy ion collisions. *J. Phys.*, G40:105108, 2013.
- [80] Derek Teaney and Li Yan. Triangularity and Dipole Asymmetry in Heavy Ion Collisions. *Phys. Rev.*, C83:064904, 2011.
- [81] Katarna Gajdoov. Investigations of anisotropic collectivity using multiparticle correlations in pp, pPb and PbPb collisions. *Nucl. Phys.*, A967:437–440, 2017.
- [82] Nicolas Borghini, Phuong Mai Dinh, and Jean-Yves Ollitrault. Flow analysis from multiparticle azimuthal correlations. *Phys. Rev.*, C64:054901, 2001.
- [83] Zhi Qiu and Ulrich W. Heinz. Event-by-event shape and flow fluctuations of relativistic heavy-ion collision fireballs. *Phys. Rev.*, C84:024911, 2011.
- [84] Jinghua Fu. Centrality dependence of mapping the hydrodynamic response to the initial geometry in heavy-ion collisions. *Phys. Rev.*, C92(2):024904, 2015.
- [85] H. Niemi, K. J. Eskola, and R. Paatelainen. Event-by-event fluctuations in a perturbative QCD + saturation + hydrodynamics model: Determining QCD matter shear viscosity in ultrarelativistic heavy-ion collisions. *Phys. Rev.*, C93(2):024907, 2016.
- [86] Jacquelyn Noronha-Hostler, Li Yan, Fernando G. Gardim, and Jean-Yves Ollitrault. Linear and cubic response to the initial eccentricity in heavy-ion collisions. *Phys. Rev.*, C93(1):014909, 2016.
- [87] Niseem Magdy. Beam energy dependence of the anisotropic flow coefficients v_n . *PoS*, CPOD2017:005, 2017.
- [88] Niseem Magdy. Viscous Damping of Anisotropic Flow in 7.7200 GeV Au+Au Collisions. *J. Phys. Conf. Ser.*, 779(1):012060, 2017.

- [89] Iu. A. Karpenko, P. Huovinen, H. Petersen, and M. Bleicher. Estimation of the shear viscosity at finite net-baryon density from $A + A$ collision data at $\sqrt{s_{NN}} = 7.7 - 200$ GeV. *Phys. Rev.*, C91(6):064901, 2015.
- [90] L. Adamczyk et al. Inclusive charged hadron elliptic flow in Au + Au collisions at $\sqrt{s_{NN}} = 7.7 - 39$ GeV. *Phys. Rev.*, C86:054908, 2012.
- [91] Laszlo P. Csernai, Joseph.I. Kapusta, and Larry D. McLerran. On the Strongly-Interacting Low-Viscosity Matter Created in Relativistic Nuclear Collisions. *Phys. Rev. Lett.*, 97:152303, 2006.
- [92] Pawel Danielewicz, Roy Lacey, and William G. Lynch. Determination of the equation of state of dense matter. *Science*, 298:1592–1596, 2002.
- [93] Fernando G. Gardim, Frederique Grassi, Yojiro Hama, Matthew Luzum, and Jean-Yves Ollitrault. Directed flow at mid-rapidity in event-by-event hydrodynamics. *Phys. Rev.*, C83:064901, 2011.
- [94] Roy A. Lacey. Indications for a Critical End Point in the Phase Diagram for Hot and Dense Nuclear Matter. *Phys. Rev. Lett.*, 114(14):142301, 2015.
- [95] J. Adam et al. Beam energy dependence of rapidity-even dipolar flow in Au+Au collisions. *Phys. Lett.*, B784:26–32, 2018.
- [96] Piotr Bozek. Event-by-event viscous hydrodynamics for CuAu collisions at $\sqrt{s_{NN}}=200$ GeV. *Phys. Lett.*, B717:287–290, 2012.
- [97] L. Adamczyk et al. Beam Energy Dependence of the Third Harmonic of Azimuthal Correlations in Au+Au Collisions at RHIC. *Phys. Rev. Lett.*, 116(11):112302, 2016.
- [98] Vardan Khachatryan et al. Measurement of long-range near-side two-particle angular correlations in pp collisions at $\sqrt{s} = 13$ TeV. *Phys. Rev. Lett.*, 116(17):172302, 2016.
- [99] Georges Aad et al. Observation of Long-Range Elliptic Azimuthal Anisotropies in $\sqrt{s} = 13$ and 2.76 TeV pp Collisions with the ATLAS Detector. *Phys. Rev. Lett.*, 116(17):172301, 2016.

- [100] A. Adare et al. Measurement of long-range angular correlation and quadrupole anisotropy of pions and (anti)protons in central d +Au collisions at $\sqrt{s_{NN}}=200$ GeV. *Phys. Rev. Lett.*, 114(19):192301, 2015.
- [101] L. Adamczyk et al. Effect of event selection on jetlike correlation measurement in d +Au collisions at $\sqrt{s_{NN}} = 200$ GeV. *Phys. Lett.*, B743:333–339, 2015.
- [102] Serguei Chatrchyan et al. Observation of long-range near-side angular correlations in proton-lead collisions at the LHC. *Phys. Lett.*, B718:795–814, 2013.
- [103] Betty Abelev et al. Long-range angular correlations on the near and away side in p -Pb collisions at $\sqrt{s_{NN}} = 5.02$ TeV. *Phys. Lett.*, B719:29–41, 2013.
- [104] Georges Aad et al. Observation of Associated Near-Side and Away-Side Long-Range Correlations in $\sqrt{s_{NN}}=5.02$ TeV Proton-Lead Collisions with the ATLAS Detector. *Phys. Rev. Lett.*, 110(18):182302, 2013.
- [105] Kevin Dusling and Raju Venugopalan. Comparison of the color glass condensate to dihadron correlations in proton-proton and proton-nucleus collisions. *Phys. Rev.*, D87(9):094034, 2013.
- [106] Piotr Bozek and Wojciech Broniowski. Collective dynamics in high-energy proton-nucleus collisions. *Phys. Rev.*, C88(1):014903, 2013.
- [107] Kevin Dusling, Wei Li, and Björn Schenke. Novel collective phenomena in high-energy proton-proton and proton-nucleus collisions. *Int. J. Mod. Phys.*, E25(01):1630002, 2016.
- [108] Roy A. Lacey, Yi Gu, X. Gong, D. Reynolds, N. N. Ajitanand, J. M. Alexander, A. Mwai, and A. Taranenko. Is anisotropic flow really acoustic? 2013.
- [109] Edward Shuryak and Ismail Zahed. High-multiplicity pp and pA collisions: Hydrodynamics at its edge. *Phys. Rev.*, C88(4):044915, 2013.
- [110] Roy A. Lacey, A. Taranenko, N. N. Ajitanand, and J. M. Alexander. Scaling of the higher-order flow harmonics: implications for initial-eccentricity models and the 'viscous horizon'. 2011.

- [111] Pilar Staig and Edward Shuryak. The Fate of the Initial State Fluctuations in Heavy Ion Collisions. II The Fluctuations and Sounds. *Phys. Rev.*, C84:034908, 2011.
- [112] Roy A. Lacey, Peifeng Liu, Niseem Magdy, M. Csand, B. Schweid, N. N. Ajitanand, J. Alexander, and R. Pak. Scaling properties of the mean multiplicity and pseudorapidity density in $e^- + e^+$, $e^\pm + p$, $p(\bar{p}) + p$, $p + A$ and $A + A(B)$ collisions. 2016.
- [113] Peifeng Liu and Roy A. Lacey. System-size dependence of the viscous attenuation of anisotropic flow in $p + Pb$ and $Pb + Pb$ collisions at LHC energies. 2018.
- [114] Peifeng Liu and Roy A. Lacey. Acoustic scaling of linear and mode-coupled anisotropic flow; implications for precision extraction of the specific shear viscosity. 2018.
- [115] Bjoern Schenke, Prithwish Tribedy, and Raju Venugopalan. Initial-state geometry and fluctuations in $Au + Au$, $Cu + Au$, and $U + U$ collisions at energies available at the BNL Relativistic Heavy Ion Collider. *Phys. Rev.*, C89(6):064908, 2014.
- [116] Roy A. Lacey, Rui Wei, N. N. Ajitanand, and A. Taranenko. Initial eccentricity fluctuations and their relation to higher-order flow harmonics. *Phys. Rev.*, C83:044902, 2011.
- [117] Paolo Alba, Valentina Mantovani Sarti, Jorge Noronha, Jacquelyn Noronha-Hostler, Paolo Parotto, Israel Portillo Vazquez, and Claudia Ratti. Effect of the QCD equation of state and strange hadronic resonances on multiparticle correlations in heavy ion collisions. 2017.
- [118] C. Adler et al. Elliptic flow from two and four particle correlations in $Au + Au$ collisions at $\sqrt{s(NN)}^{1/2} = 130\text{-GeV}$. *Phys. Rev.*, C66:034904, 2002.
- [119] Mike Miller and Raimond Snellings. Eccentricity fluctuations and its possible effect on elliptic flow measurements. 2003.
- [120] S. Manly et al. System size, energy and pseudorapidity dependence of directed and elliptic flow at RHIC. *Nucl. Phys.*, A774:523–526, 2006.

- [121] B. Alver et al. System size, energy, pseudorapidity, and centrality dependence of elliptic flow. *Phys. Rev. Lett.*, 98:242302, 2007.
- [122] Georges Aad et al. Measurement of the distributions of event-by-event flow harmonics in lead-lead collisions at $\sqrt{s_{NN}} = 2.76$ TeV with the ATLAS detector at the LHC. *JHEP*, 11:183, 2013.
- [123] H. Niemi, G. S. Denicol, H. Holopainen, and P. Huovinen. Event-by-event distributions of azimuthal asymmetries in ultrarelativistic heavy-ion collisions. *Phys. Rev.*, C87(5):054901, 2013.
- [124] Jaroslav Adam et al. Event shape engineering for inclusive spectra and elliptic flow in Pb-Pb collisions at $\sqrt{s_{NN}} = 2.76$ TeV. *Phys. Rev.*, C93(3):034916, 2016.